Astronomy Letters, Vol. 30, No. 11, 2004, pp. 729–736. Translated from Pis'ma v Astronomicheskiĭ Zhurnal, Vol. 30, No. 11, 2004, pp. 803–811.

The SAI Catalog of Supernovae and Radial Distributions of Supernovae of Various Types in Galaxies

D. Yu. Tsvetkov*, N. N. Pavlyuk, and O. S. Bartunov*****

Sternberg Astronomical Institute, Universitetskiĭ pr. 13, Moscow, 119992 Russia

Received May 18, 2004

Abstract—We describe the Sternberg Astronomical Institute (SAI) catalog of supernovae. We show that the radial distributions of type-Ia, type-Ibc, and type-II supernovae differ in the central parts of spiral galaxies and are similar in their outer regions, while the radial distribution of type-Ia supernovae in elliptical galaxies differs from that in spiral and lenticular galaxies. We give a list of the supernovae that are farthest from the galactic centers, estimate their relative explosion rate, and discuss their possible origins.

Key words: *astronomical catalogs, supernovae, observations, radial distributions of supernovae.*

INTRODUCTION

In recent years, interest in studying supernovae (SNe) has increased significantly. Among other reasons, this is because SNe Ia are used as "standard candles" for constructing distance scales and for cosmological studies, and because SNe Ibc may be related to gamma ray bursts.

Many new programs of searching for SNe using modern CCD detectors and automated telescopes have been initiated, and the number of discoveries per year has increased from 20–30 in the 1980s to about 300 in the last several years.

Therefore, the collection and systematization of SN data and their presentation in a form convenient for statistical and other studies are of particular interest.

The first lists of SNe appeared in the late 1950s and were repeatedly updated as the number of discovered objects increased (Zwicky 1958, 1965; Kowal and Sargent 1971; Sargent *et al.* 1974). The catalogs by Karpowicz and Rudnicki (1968) and Flin *et al.* (1979) also contained a complete bibliography for each object. In the last twenty years, the Asiago Observatory catalog of supernovae (Barbon *et al.* 1984, 1989, 1999) has received the greatest recognition; in addition to SN data, it also contains basic information about the host galaxies. A list of SNe was included in the fifth volume of the General Catalog of Variable Stars (Artyukhina *et al.* 1995). At present, continuously updated lists and catalogs of SNe can be found on the Internet. The most complete data are contained in the list of SNe maintained by the Central Bureau of Astronomical Telegrams (http://cfa-www.harvard.edu/cfa/ps/lists/Supernovae.html) and the electronic version of the Asiago catalog (http://web.pd.astro.it/supern).

Studies of the SN distribution in galaxies are of great interest in elucidating the nature of the stellar populations that provide SN explosions of a certain type. Although the presupernova stars are currently known for several SNe II (SN 1987A, 1993J, 2003gd), the origin of presupernovae of other types is still an open question in many respects. Of particular interest is the possible difference between the populations of type-Ia presupernovae in galaxies of different types, which can affect the results of cosmological studies using them.

Despite the rapid increase in the amount of data, the SN distributions in galaxies have been studied rarely in recent years. After the paper of Bartunov *et al.* (1992), which gives references to previous papers, we note the works of van den Bergh (1997), Bartunov and Tsvetkov (1997), Wang *et al.* (1997), and Howell *et al.* (2000). Tsvetkov *et al.* (2001) compared the radial distributions of gamma ray bursts and SNe Ibc.

Since the number of SNe discovered since the last comprehensive studies of the radial distribution has increased by more than a factor of 2, a new study would be of great interest.

*E-mail: tsvetkov@sai.msu.su
**E-mail: pavlyuk@sai.msu.su
***E-mail: oleg@sai.msu.su

THE SAI CATALOG OF SUPERNOVAE

Description of the Catalog

For statistical studies of SNe, it is necessary to collect data on all the discovered SNe and on their host galaxies.

The SAI catalog of supernovae was originally intended precisely for statistical studies; its compilation was begun in 1986 on the basis of existing SN lists and published data. One version of the catalog was described by Tsvetkov and Bartunov (1993).

The current version of the SAI catalog of supernovae contains data on 2780 extragalactic SNe discovered from 1885 until January 6, 2004, and on their host galaxies. The catalog is accessible on the Internet: http://www.sai.msu.su/sn/sncat; it is also possible to directly retrieve data from the catalog using a number of key parameters (http://www.sai.msu.su/cgi-bin/wdb-p95/sn/sncat/form).

The catalog presents the following data:

(1) SN name;

(2) Galaxy name;

(3) Equatorial coordinates of the galaxy for epoch 2000.0;

(4) Galaxy magnitude and its source;

(5) Position angle of the major axis of the galaxy;

(6) Inclination of the galaxy to the plane of the sky;

(7) Radial velocity or redshift of the galaxy;

(8) Morphological type of the galaxy from the RC3 catalog (de Vaucouleurs *et al.* 1991); galaxy membership in a double or triple system is additionally specified;

(9) Logarithm of the apparent axial ratio of the galaxy;

(10) Logarithm of the apparent length of the major axis;

(11) Numerical code of the morphological type;

(12) Galaxy luminosity class;

(13) Galactocentric distance of the SN in the north–south and east–west directions, in arcsecs;

(14) SN magnitude; it is additionally specified whether this is the magnitude at maximum brightness determined from the light curve or an estimate at a certain time, most often at the discovery (the magnitude at maximum could then be brighter); the photometric band (if it is a standard one) is also given;

(15) Date of maximum SN brightness;

(16) SN discovery date;

(17) SN type;

(18) SN equatorial coordinates for epoch 2000.0;

(19) Search program or observatory that discovered the SN;

(20) Discoverers' names.

The SNe are arranged in order of their increasing numbers assigned by the Central Bureau of Astronomical Telegrams of the International Astronomical Union.

Initially, IAU Circulars served as the main sources of SN data. However, if these data are refined or modified in subsequent works, then appropriate changes are made to the catalog.

The identification of SN host galaxies, which is easy for bright and nearby objects, becomes increasingly difficult, because the number of discovered faint and distant SNe has increased significantly in recent years. In addition, difficulties arise when a SN explodes in a multiple system of galaxies or in a peculiar galaxy. Therefore, when compiling the catalog, the sky field around each SN was studied using DSS (http://archive.stsci.edu/dss/index.html). To find the most likely host galaxy, in addition to the sky positions, we also use data on the radial velocities and brightnesses of the galaxy and the SN. If the host galaxy is multiple, this is specified in the description of the galaxy type.

The main source of data on the host galaxies was the LEDA database (http://www-obs.univ-lyon1.fr/hypercat). However, the radial velocities (or redshifts) of the galaxies were taken from the NED database (http://nedwww.ipac.caltech.edu). The magnitudes were taken from the UGC (Nilson 1973) and ESO (Lauberts 1982) catalogs for most of the galaxies and from the LEDA database and the PGC catalog (Paturel *et al.* 1989) and, if no data were available in these sources, from the NED database or IAU Circulars for fainter galaxies.

In several cases, we compared our data and those from the Asiago catalog and the SN list of the Central Bureau of Astronomical Telegrams. However, the catalogs are compiled independently.

Statistical Data

Figure 1 shows the distribution of SN discoveries in years, with the SNe discovered photographically being highlighted. We see a sharp increase in the number of discoveries in the mid-1990s and another jump in 2001. The photographic searches for SNs ceased in 2000, but the number and fraction of SNe discovered photographically began to decrease after 1992.

The distributions in SN and galaxy types are shown in Figs. 2 and 3, respectively. These data are similar to those of Barbon *et al.* (1999).

The SN redshift distribution is shown in Fig. 4. The programs of searching for distant SNe initiated in the mid-1990s have discovered mostly SNe Ia with $0.3 < z < 1.0$, while the "ordinary" programs have

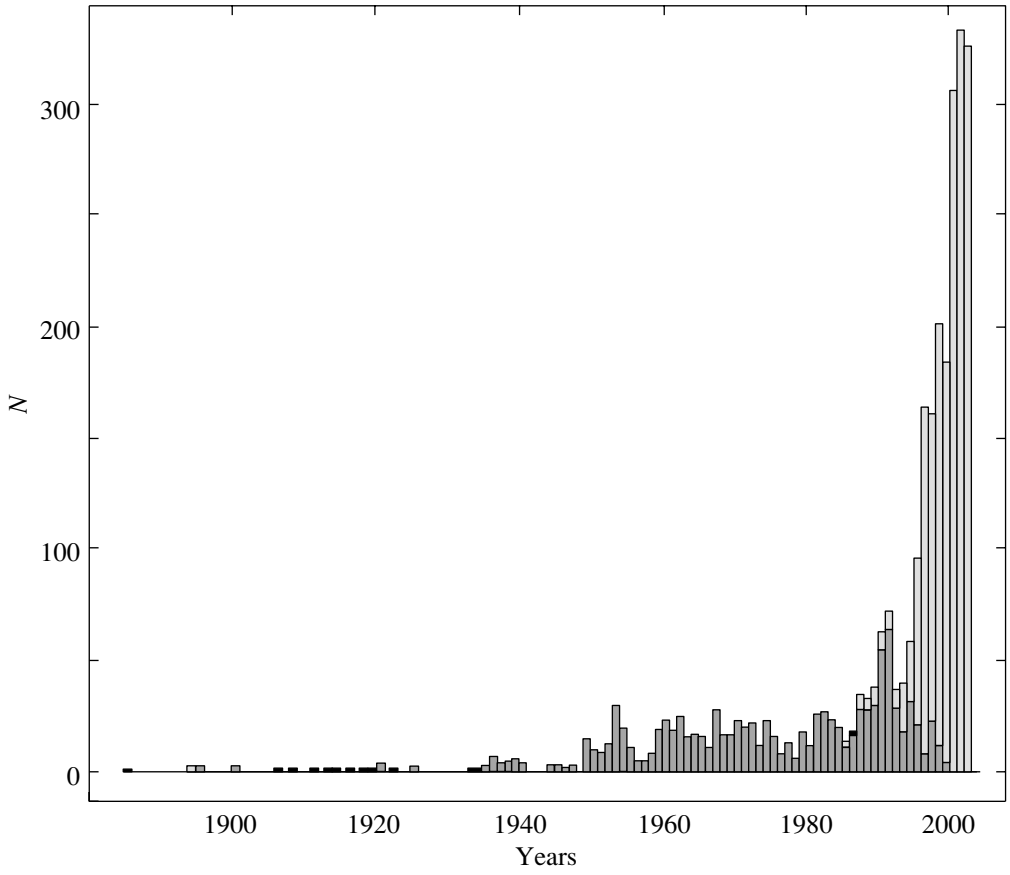

Fig. 1. Distribution of SN discoveries in years. The dark shading highlights the SNe discovered photographically.

discovered SNe with $z < 0.1$, with their distribution peaking near $z = 0.02$.

The distribution of SNe in the plot of magnitude against the logarithm of the product of the speed of light by the redshift is shown in Fig. 5. The magnitudes for most of the SNe are the estimates at the time of their discovery and could be much larger than those at maximum brightness. We see that the line corresponding to $M = -19.5$ is essentially the upper envelope of the set of points; only a few SNe lie above and to the left of it. The brightest SNe II and SNe Ibc lie near the line and, consequently, have almost the same luminosity at maximum as SNe Ia. The large scatter in the lower left part of the diagram is attributable to the peculiar velocities of the galaxies; for SNe with high radial velocities and shifted far leftward of and above the line, the redshifts and magnitudes are determined with a large uncertainty.

RADIAL DISTRIBUTIONS OF SNe IN THEIR HOST GALAXIES

Method of Analysis

The method of analyzing the radial distributions is virtually identical to the method that we used previously (Bartunov *et al.* 1992). For each SN, we calculated the following quantities: the relative radial distance r and the radial distance in kiloparsecs R: $r = 2\sqrt{\Delta\alpha^2 + \Delta\delta^2}/D_{25}$; $R = V_r\sqrt{\Delta\alpha^2 + \Delta\delta^2}/206.3H_0$, where $\Delta\alpha$ and $\Delta\delta$ are the distances from the SN to the Galactic center, D_{25} is the diameter of the galaxy up to the $25^m/\square''$ isophote, V_r is the radial velocity of the galaxy, and H_0 is the Hubble constant

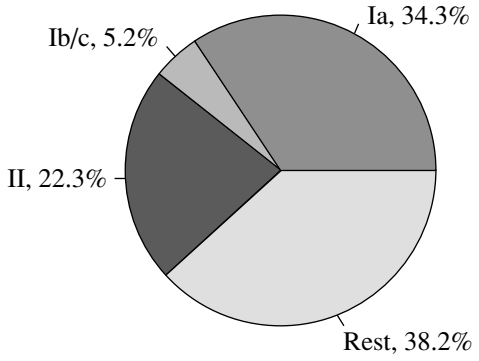

Fig. 2. Distribution of SNe in types.

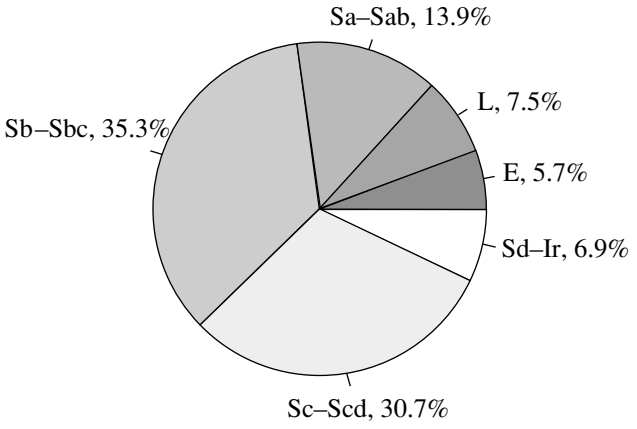

Fig. 3. Distribution of SNe in morphological types of their host galaxies.

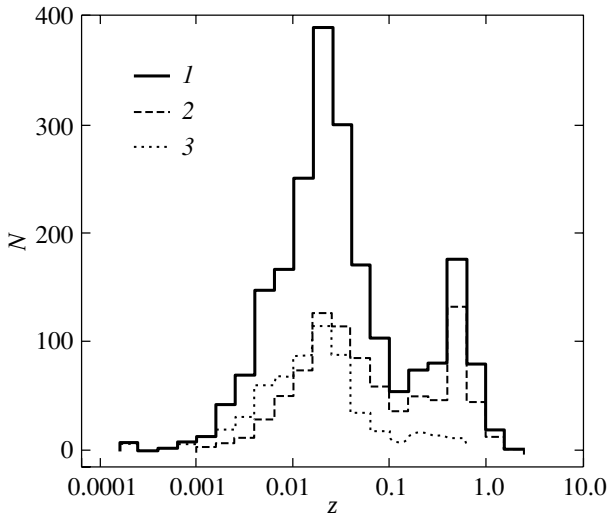

Fig. 4. Redshift distribution of SNe: (*1*) all SNe, (*2*) SNe Ia, (*3*) SNe II.

assumed to be 75 km s^{-1}Mpc^{-1}. We also calculated the distance r_c normalized not to the length of the galaxy's major axis, but to the galaxy's size along the SN radius vector: $r_c = r/\sqrt{\cos^2\theta + k^2\sin^2\theta}$, where θ is the angle between the SN radius vector and the major axis of the galaxy, and k is the ratio of the minor and major apparent axes of the galaxy. For spiral and lenticular galaxies, r_c may be considered as the relative distance corrected for the galaxy's inclination if the SN lies in the galactic plane. The distance in kiloparsecs can also be corrected in a similar way: $R_c = Rr_c/r$. Subsequently, we constructed the SN distribution histograms and the corresponding plots of surface density σ versus radial distance. In contrast to our previous papers, we did not smooth the data; when calculating the surface density in galactic regions far from the center, we increased the bins in which the number of SNe was counted.

SN Samples

Our samples included SNe in galaxies for which information about the morphological type, apparent sizes, and radial velocities was available and which were not members of double or multiple systems. We considered only galaxies with radial velocities $V_r <$ 30 000 km s^{-1} and spiral and lenticular galaxies with inclinations of less than 70°. We plotted the distributions for the following samples (the number of SNe in the sample is given in parentheses):

ASCCD (515), AECCD (29), ALCCD (45): all of the SNe discovered in spiral, elliptical, and lenticular galaxies, respectively, through CCD and visual observations;

ASPHOT (413), AEPHOT (32), ALPHOT (50): all the SNe discovered in spiral, elliptical, and lenticular galaxies, respectively, through photographic observations;

ASCCDN (273), ASPHOTN (244): SNe from the ASCCD and ASPHOT samples in galaxies with $V_r < 5100$ km s^{-1};

ASCCDF (242), ASPHOTF (168): SNe from the ASCCD and ASPHOT samples in galaxies with $V_r > 5100$ km s^{-1};

IAS (231): SNe Ia in spiral galaxies;

IIS (343): SNe II in spiral galaxies;

IBCS (88): type Ibc supernovae (including Ib, Ic and Ib/c types) in spiral galaxies;

IASCCDN (66): SNe Ia from the ASCCDN sample;

IISCCDN (142): SNe II from the ASCCDN sample;

IBCSCCDN (46): SNe Ibc from the ASCCDN sample;

AE (61): all SNe in elliptic galaxies;

AL (95): all SNe in lenticular galaxies.

A comparison showed that the difference between the distributions in distances r and r_c is insignificant for our samples; below, we use only the distributions in r_c and R_c.

Selection Effects

The considerable increase in the number of SNe allowed the selection effects that affect the observed distributions to be estimated more reliably. Bartunov *et al.* (1992) and Howell *et al.* (2000) showed that a significant fraction of SNe in the central parts of galaxies is lost in photographic SN searches due to overexposure; this effect is enhanced with increasing distance to the galaxies. In the sample by Bartunov *et al.* (1992), the number of SNe discovered during

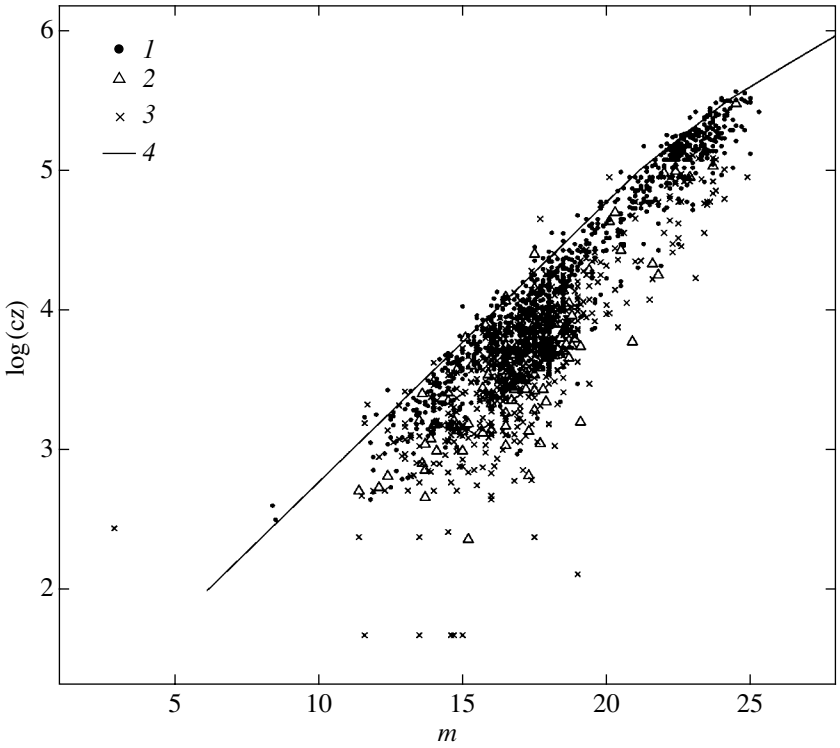

Fig. 5. SN distribution in the plot of magnitude versus logarithm of the product of the speed of light by the redshift: (*1*) SNe Ia, (*2*) SNe Ibc, (*3*) SNe II, (*4*) positions of the objects with $M = -19.5$ for $H_0 = 75$ km s^{-1} Mpc^{-1}, $q_0 = 0$.

visual and CCD observations was much smaller than that discovered photographically. In our sample, their number is approximately the same, which enables us to carry out a much more detailed and reliable study. The results are presented in Fig. 6. A comparison of the plots of logarithm of the surface density against relative radial distance for SNe in spiral galaxies indicates that some of the SNe at $r_c < 0.4$ are actually undetectable through photographic searches, and this fraction strongly depends on the distance. The SN loss is 21, 46, and 10% of the total sample size for the ASPHOT, ASPHOTF, and ASPHOTN samples, respectively. A small loss of SNe at the very centers of spiral galaxies is also observed for the ASCCDF sample; it is about 7%. We see from Fig. 6 that this effect is smaller for elliptical galaxies: it is about 6%. For lenticular galaxies, it is approximately the same as that for spirals, about 32%. However, these estimates are much less reliable than those for spiral galaxies, because the number of SNe is much smaller.

These results show that a selection-free dependence of the SN surface density on the relative radial distance can be obtained by choosing only the SNe discovered through CCD and visual observations in nearby galaxies.

Radial Distributions

The radial distributions of SNe of various types in spiral galaxies and the distributions of all SNe in elliptical and lenticular galaxies are shown in Fig. 7. For comparison, this figure shows the dependences of the surface brightness on the radial distance for elliptical and spiral galaxies and the distributions of OB associations in M 33 and H II regions in NGC 3184 (a description and the sources of these data were given by Bartunov *et al.* (1992) and Tsvetkov *et al.* (2001)).

We see that the distributions of SNe of various types discovered using CCD and visually in nearby galaxies, in the central parts of spiral galaxies differ significantly. The most interesting feature of the distributions is a reduced SN Ia density in the innermost regions of spiral galaxies that was first found by van den Bergh (1997) and Wang *et al.* (1997). Note also the rapid drop in the SN Ibc density in the central regions of galaxies and an almost constant SN II density at $r_c < 0.5$. At $r_c > 0.5$, the distributions of SNe of various types are almost identical. As would be expected, the SN II distribution bears a strong similarity to the distribution of OB associations and H II regions; however, the SN Ibc distribution differs greatly from it. At the same time, for the complete samples, the difference between SNe Ibc and SNe II is much smaller, indicating a stronger influence of selection on the results for SNe Ibc. Since Tsvetkov *et*

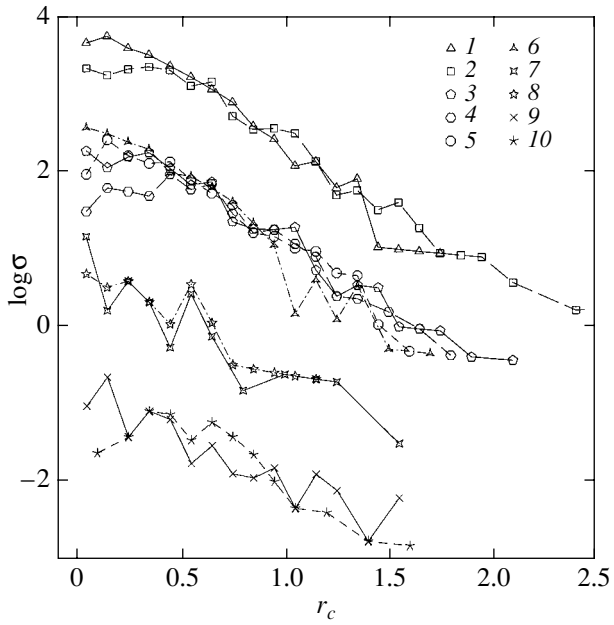

Fig. 6. Influence of selection effects on the radial distributions of SNe. The distributions for the following samples are shown: (*1*) ASCCD, (*2*) ASPHOT, (*3*) ASPHOTN, (*4*) ASPHOTF, (*5*) ASCCDF, (*6*) ASCCDN, (*7*) AECCD, (*8*) AEPHOT, (*9*) ALCCD, (*10*) ALPHOT.

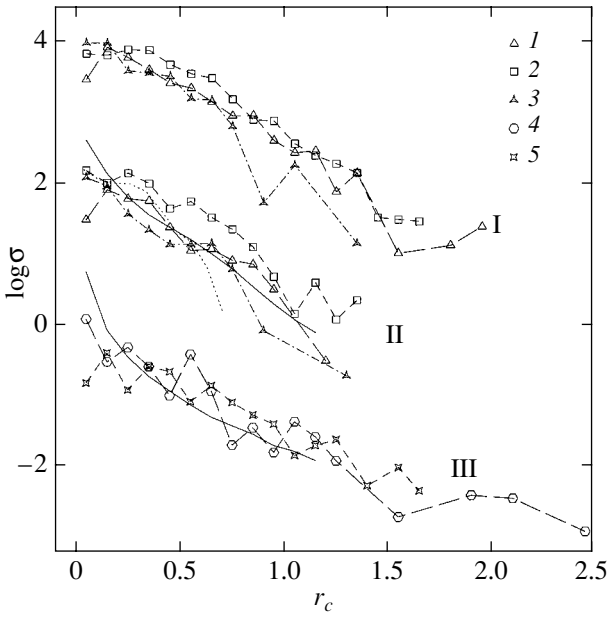

Fig. 7. Radial distributions of SNe of various types: (*1*) SNe Ia, (*2*) SNe II, (*3*) SNe Ibc ((I) IAS, IIS, IBCS samples; (II) IASCCDN, IISCCDN, IBCSCCDN samples), (*4*) AE sample, (*5*) AL sample (the solid lines indicate the luminosity distribution in an "average" spiral galaxy (II) and an elliptic galaxy (III); the dotted line indicates the distribution of OB associations and H II regions).

al. (2001) used only the complete sample of SNe Ibc, it is clear why they concluded that the distributions of SNe Ibc and OB associations and H II regions were similar. In reality, the SN Ibc distribution in the central regions of galaxies agrees well with the luminosity distribution. Unfortunately, the number of SNe IIL, IIP, IIn, and IIb is too small for the radial distribution to be studied.

The radial distribution of SNe (mostly SNe Ia) in elliptical galaxies differs greatly from that for spiral galaxies. Here, the surface density increases up to the center and agrees well with the luminosity distribution. However, in lenticular galaxies the SN Ia distribution is the same as that in spirals.

We also studied the possible r_c dependence of the SN Ia brightness decline rate described by the quantity Δm_{15} in spiral galaxies. We found no statistically significant dependence, as was the case in the paper by Ivanov *et al.* (2000).

The surface density is plotted against the galactocentric distances in kiloparsecs in Fig. 8. These plots show the same features as the distribution in r_c: a reduced SN Ia density at the centers of spiral and lenticular galaxies, a constant SN II density at $R_c < 5$ kpc, a rapid drop in the SN Ibc density in the central regions of galaxies, and almost identical distributions of SNe of all types at $R_c > 5$ kpc.

SUPERNOVAE FLARING UP FAR FROM THE GALACTIC CENTERS

Of particular interest in studying the radial distribution of SNe are objects located far beyond the optical radius of galaxies. Tammann (1974) was the first to call attention to them.

Recently, intergalactic SNe Ia supernovae have been discovered in clusters of galaxies; it is assumed that their fraction could be about 20% (Gal-Yam *et al.* 2003).

Data on the SNe farthest from the galactic centers ($r > 2$) are given in the table. We did not calculate r_c and R_c for them, because it is unlikely that these SNe belong to the galactic disks.

Most of these SNe belong to early-type galaxies, with their fraction of the total number of SNe from our samples in elliptical, lenticular, and spiral galaxies being 5, 3, and 0.5%, respectively. According to de Vaucouleurs *et al.* (1991), about 14 and 2% of the luminosity of elliptical and spiral galaxies, respectively, can be beyond the relative radius $r = 2$. Thus, our estimates of the frequency of occurrence of distant SNe are consistent with the assumption that they flare up in distant galactic halos, which are particularly extended in elliptical galaxies. However, SN II and Ibc explosions at such large distances still deserve

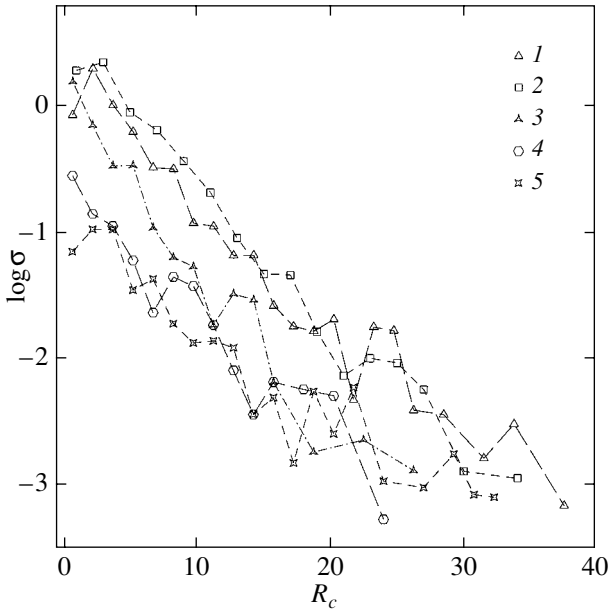

Fig. 8. Surface density of SNe of various types versus galactocentric distance R_c in kiloparsecs for the following samples: (*1*) IAS, (*2*) IIS, (*3*) IBCS, (*4*) AE, (*5*) AL.

special attention, because the presence of high-mass stars in the halo is unlikely.

SN IIP 1969L in NGC 1058 was noticed by Tammann (1974); he obtained deep photographs of the galaxy and found two unusual weak and broad spiral arms in them. The SN flared up in one of them, with this arm extending still farther from the explosion site.

SN Ib 1997C flared up in the pair of galaxies NGC 3158–NGC 3160 very close to the line connecting the components; the distance from SN to NGC 3160 is approximately half the distance from SN to NGC 3158. NGC 3158 is an elliptical galaxy that is brighter than NGC 3160 by more than 2^m. No low-surface-brightness features were found in the DSS maps at the SN explosion site.

Thus, it may well be that, in these cases, the presence of high-mass stars far beyond the optical radius is attributable to the peculiar nature of the galaxy NGC 1058 and to the interaction in the NGC 3158–NGC 3160 pair.

SNe farthest from the galactic centers

SN	SN type	Galaxy	Galaxy type	r	R, kpc
1968Z		NGC 7768	E	2.17	50.4
1969L	IIP	NGC 1058	Sc	2.66	9.7
1970L	I	NGC 2968	Sa	2.16	17.8
1971C		NGC 3904	E	2.78	28.0
1976L	I	NGC 1411	L	2.42	9.2
1980I	Ia	NGC 4374	E	2.46	35.2
1980M		ESO 366-G05	Sc	2.06	29.5
1982E		NGC 1332	L	2.89	31.0
1982X		UGC 4778	Sb	3.89	69.5
1992bo	Ia	ESO 352-G57	L	2.17	25.4
1997C	Ib	NGC 1360	Sbc	2.53	42.9

CONCLUSIONS

The SAI catalog of supernovae allows statistical studies of SNe to be carried out fast and effectively. As an example, we have studied the radial distribution of SNe in galaxies.

We showed that the radial distributions of SNe of three main types (Ia, Ibc, II) in the central regions of spiral galaxies differ significantly. Only the distribution of SNe II agrees, as would be expected, with the distribution of young high-mass stars. SNe Ibc, which show a distribution relative to star-forming regions similar to that of SNe II (Bartunov *et al.* 1994; van Dyk 1992), concentrate much more strongly toward the galactic centers; their distribution is similar to the luminosity distribution. SNe Ia in spiral and lenticular galaxies have a reduced explosion rate in the innermost parts, while their distribution in elliptical galaxies is similar to the luminosity distribution. These results are difficult to explain in terms of the universally accepted ideas of the nature of type-Ibc and type-Ia presupernovae.

Data on SNe observed far beyond the optical radius of galaxies show that their fraction is rather small, and these explosions can occur in the halos of galaxies or in peculiar and interacting systems. However, a more detailed study of the explosion sites of these SNe (especially SNe II and SNe Ibc) should be performed in an attempt to find the stellar population located there.

REFERENCES

1. N. M. Artyukhina, V. P. Goranskiĭ, N. A. Gorynya, *et al.*, *General Catalog of Variable Stars* (Kosmoinform, Moscow, 1995), Vol. V [in Russian].
2. R. Barbon, V. Buondi, E. Cappellaro, and M. Turatto, Astron. Astrophys., Suppl. Ser. **139**, 531 (1999).

3. R. Barbon, E. Cappellaro, F. Ciatti, *et al.*, Astron. Astrophys., Suppl. Ser. **58**, 735 (1984).
4. R. Barbon, E. Cappellaro, and M. Turatto, Astron. Astrophys., Suppl. Ser. **81**, 421 (1989).
5. O. S. Bartunov, I. N. Makarova, and D. Yu. Tsvetkov, Astron. Astrophys. **264**, 428 (1992).
6. O. S. Bartunov and D. Yu. Tsvetkov, *Thermonuclear Supernovae,* Ed. by P. Ruiz-Lapuente *et al.* (Kluwer Acad., Dordrecht, 1997), p. 87.
7. O. S. Bartunov, D. Yu. Tsvetkov, and I. V. Filimonova, Publ. Astron. Soc. Pac. **106**, 1276 (1994).
8. P. Flin, M. Karpowicz, W. Murawski, and K. Rudnicki, *Catalogue of Supernovae* (Panstwowe Wydawnictwo Naukowe, Warszawa, 1979).
9. A. Gal-Yam, D. Maoz, P. Guhathakurta, and A. V. Filippenko, Astron. J. **125**, 1087 (2003).
10. D. A. Howell, L. Wang, and J. C. Wheeler, Astrophys. J. **530**, 166 (2000).
11. V. D. Ivanov, M. Hamuy, and P. A. Pinto, Astrophys. J. **542**, 588 (2000).
12. M. Karpowicz and K. Rudnicki, *Preliminary Catalogue of Supernovae* (Warsaw Univ. Press, Warsaw, 1968).
13. C. T. Kowal and W. L. W. Sargent, Astron. J. **76**, 756 (1971).
14. A. Lauberts, *The ESO/Uppsala Survey of the ESO (B) Atlas* (ESO, Garching, 1982).
15. P. Nilson, Uppsala Astron. Obs. Ann. **6** (1973).
16. G. Paturel, P. Fouque, L. Bottinelly, and L. Gouguenheim, Astron. Astrophys., Suppl. Ser. **80**, 299 (1989).
17. W. L. W. Sargent, L. Searle, and C. T. Kowal, *Supernovae and Supernova Remnants,* Ed. by C. B. Cosmovichi (Reidel, Dordrecht, 1974), p. 33.
18. G. A. Tammann, *Supernovae and Supernova Remnants*, Ed. by C. B. Cosmovichi (Reidel, Dordrecht, 1974), p. 215.
19. D. Yu. Tsvetkov and O. S. Bartunov, Bull. Inform. CDS **42**, 17 (1993).
20. D. Yu. Tsvetkov, S. I. Blinnikov, and N. N. Pavlyuk, Pis'ma Astron. Zh. **27**, 483 (2001) [Astron. Lett. **27**, 411 (2001)].
21. S. van den Bergh, Astron. J. **113**, 197 (1997).
22. S. D. van Dyk, Astron. J. **103**, 1788 (1992).
23. G. de Vaucouleurs, A. de Vaucouleurs, H. G. Corwin, *et al.*, *Third Reference Catalogue of Bright Galaxies* (Springer-Verlag, New York, 1991).
24. L. Wang, P. Hoflich, and J. C. Wheeler, Astrophys. J. Lett. **483**, L29 (1997).
25. F. Zwicky, *Handbuch der Physik,* Ed. by S. Flugge (Springer, Berlin, 1958), Vol. 51, p. 766.
26. F. Zwicky, *Stars and Stellar Systems,* Ed. by L. H. Aller and M. C. McLaughlin (Univ. of Chicago Press, Chicago, 1965), Vol. VIII, p. 367.

Translated by G. Rudnitskii

Astronomy Letters, Vol. 30, No. 11, 2004, pp. 737–750. Translated from Pis'ma v Astronomicheskiĭ Zhurnal, Vol. 30, No. 11, 2004, pp. 812–826.

Dynamics and Radiation of Young Type-Ia Supernova Remnants: Important Physical Processes

E. I. Sorokina[1*], S. I. Blinnikov[1,2], D. I. Kosenko[1,2], and P. Lundqvist[3]

[1] *Sternberg Astronomical Institute, Universitetskiĭ pr. 13, Moscow, 119992 Russia*

[2] *Institute of Theoretical and Experimental Physics, ul. Bol'shaya Cheremushkinskaya 25, Moscow, 117259 Russia*

[3] *Stockholm Observatory, AlbaNova, SE-106 91 Sweden*

Received April 25, 2004

Abstract—We analyze the physical processes that should be taken into account when modeling young type-Ia supernova remnants (SNRs) with ages of several hundred years in which forward (into the interstellar medium) and reverse (into the ejection) shocks propagate. We show that the energy losses in a heavy-element-rich ejection can be significant for SNRs even at this evolutionary phase. We study the effects of electron thermal conduction and the rate of energy exchange between electrons and ions on the temperature distribution and the X-ray emission from such SNRs. We use observational data for the Tycho SNR from the XMM-Newton Space X-ray Telescope to compare our calculations with observations.

Key words: *X-ray astronomy, supernova remnants, models.*

INTRODUCTION

Supernova remnants (SNRs) have long been simulated numerically. However, since the physics of these objects is very complex, they have not yet been completely included in any computer code in the world; different physical processes can be important at different evolutionary phases.

In this paper, we consider young SNRs that have swept up interstellar gas with a mass of the order of the ejection mass during their expansion after the supernova explosion. Two shocks are formed in the SNR at this evolutionary phase. One propagates outward, into the interstellar medium, thereby increasing the mass of the swept-up gas, while the other travels inward, through a supernova ejection that has already cooled down due to adiabatic expansion, reheating it to temperatures of 10^7–10^9 K. Thus, there is another opportunity to study the matter ejected during a supernova explosion, to analyze the density and chemical-element distributions, and, possibly, to better understand the explosion physics.

Nadezhin (1981, 1985) and Chevalier (1982) suggested self-similar solutions for this evolutionary phase more than twenty years ago. These solutions correctly predict the overall hydrodynamic structure of an SNR and the formation of shocks in it. However, many physical processes without which the peculiarities of SNR radiation cannot be correctly predicted are impossible to in corporate into them. For example, time-dependent ionization, dependent on the entire preceding evolution of the SNR, cannot in principle be taken into account in a self-similar solution, although it is very significant for young SNRs inside which an ionization equilibrium is established in several hundred years. Therefore, numerical simulations that include nonequilibrium processes are required to properly understand the particular features of the radiation from SNRs of such an age.

The realization of this fact has led to the appearance of many works aimed at studying the effects of various physical processes in SNRs (time-dependent ionization, the possible difference between the electron and ion temperatures, the influence of radiative losses, allowance for electron thermal conduction and nonthermal particles). Here, we refer only to works on modeling the Tycho SNR. Without claiming to be complete, we summarized these works in Table 1 by specifying precisely which physical processes were taken into account in each of them. The time-dependent ionization was taken into account in all works. The hydrodynamic evolution was not computed only by Hamilton and Sarazin (1984b). Instead, these authors took a self-similar solution from their previous paper (Hamilton and Sarazin 1984a), but, at the same time, they were the only authors

*E-mail: sorokina@sai.msu.su

Table 1. Allowance for the physical processes in works on modeling the Tycho SNR

Work	Hydrodynamics	Time-dependent ionization	Radiative losses	Thermal conduction	T_e vs. T_i
Hamilton and Sarazin (1984b)	−	+	+	−	2–$3T$
Itoh *et al.* (1988)	+	+	−	−(+)	$2T$
Brinkmann *et al.* (1989)	+	+	−	−	$1T$
Badenes *et al.* (2003)	+	+	−	−	$2T$
This paper	+	+	+	+	1–$2T$

who took into account the radiative losses before our work. The following notation is used in the T_e vs. T_i column: $1T$ for the works in which the electron and ion temperatures are assumed to be equal; $2T$ for the works in which these temperatures are different, but become equal in most cases only through Coulomb collisions; and $3T$ for the case where two components are identified in the electron gas: a hot component heated at the shock front by plasma instabilities and a cold component emerged behind the shock front due to plasma ionization. Thermal conduction was taken into account in a self-consistent way in none of the previous works, but Itoh *et al.* (1988) proposed a temperature equilibration algorithm that, to some extent, simulates the action of thermal conduction.

Here, we include both the electron thermal conduction and the radiative losses. Our results indicate that these can significantly change the hydrodynamic structure of a SNR. However, since the ionization is time dependent, these do not strongly affect the radiation, because the ionization rate for all the actually possible variety in the temperature distribution is approximately the same, and the ion composition does not reach equilibrium values in several hundred years and, hence, is also similar for all temperatures.

We compare the results of our calculations—the X-ray spectra and the SNR surface brightness distributions under different physical conditions in different models—with recent observations of the Tycho SNR, for which data with high spatial and spectral resolutions from the XMM-Newton space telescope are available (Decourchelle *et al.* 2001).

THE SNR MODELS

We constructed the SNR model from two parts: the supernova ejection and the surrounding interstellar medium. Since our main goal here was to investigate the effects of various physical processes on SNR radiation, we took only two type-Ia supernova models with markedly different properties as the ejection:

(1) the classical W7 model (Nomoto *et al.* 1984); $M_{\rm WD} = 1.38M_\odot$, $E_0 = 1.2 \times 10^{51}$ erg, $M(^{56}{\rm Ni}) = 0.6M_\odot$;

(2) one of the first three-dimensional models from MPA (Reinecke *et al.* 2002) that is referred to below as MR0; $M_{\rm WD} = 1.38M_\odot$, $E_0 = 4.6 \times 10^{50}$ erg, $M(^{56}{\rm Ni}) = 0.43M_\odot$.

Yet another significant difference between these models is their different gas mixing: the mixing in MR0 is so strong that iron accounts for 20% of even the outermost layers of the ejection, while the mixing in W7 almost disappears even in the layer with a mass coordinate of $1.1M_\odot$. A significant factor in modeling the light curves for these models (Blinnikov and Sorokina 2004) was that the combination of the explosion energy and the mixing efficiency of the ejection matter for both models yielded almost the same velocity of the photosphere and, as a result, similar light curves. It should be noted, however, that MR0 in the UBV bands is in much better agreement with the observations, while the decline rate of the bolometric light curve better agrees with W7. We assume that a crucial factor for the radiation of an optically thin SNR must be mainly the degree of mixing, which differs significantly in the models we chose. The reverse shock successively heats up increasingly deep layers of the ejection, and the spectral evolution of the SNR depends on the degree of mixing and the abundances of various elements. In our subsequent papers, we are planning to pay more attention to the variety of models and to clarify how the model properties can be reflected in the pattern of SNR radiation.

We surrounded the ejection by a gas at rest with a constant temperature (10^4 K) and density and with solar elemental abundances. In order for the observed XMM-Newton X-ray flux from the Tycho SNR (Decourchelle *et al.* 2001) to be equal to the computed flux, we assumed the ambient density to be 5×10^{-24} g cm^{-3} at a distance of 2.3 kpc. The

computation began at a SNR age of ~ 10 yr, when the density of the outer ejection zones exceeded the interstellar density by a factor of 10 to 100. Before this time, we assumed that the ejection did not feel the presence of interstellar matter and expanded adiabatically.

BASIC EQUATIONS AND PHYSICAL PROCESSES

The Equations and the Method

The SUPREMNA code was developed to solve the problem. We used this code to solve the following system of spherically symmetric differential equations in Lagrangian coordinates:

$$\partial r/\partial t = u, \tag{1}$$

$$\frac{\partial r}{\partial m} = \frac{1}{4\pi r^2 \rho}, \tag{2}$$

$$\frac{\partial u}{\partial t} = -4\pi r^2 \frac{\partial (P_e + P_i)}{\partial m} - \frac{Gm}{r^2}, \tag{3}$$

$$\left(\frac{\partial E_e}{\partial T_e}\right)_\rho \frac{\partial T_e}{\partial t} = -4\pi P_e \frac{\partial}{\partial m}\left(r^2 u\right) - 4\pi \frac{\partial}{\partial m}\left(r^2 F_{\rm cond}\right) - \varepsilon_r - \frac{\partial \varepsilon_{\rm ion}}{\partial t} - \left(\frac{\partial E_e}{\partial X_e}\right)\frac{\partial X_e}{\partial t} + \frac{1}{\rho}\nu_{ie} k_b \left(T_i - T_e\right), \tag{4}$$

$$\left(\frac{\partial E_i}{\partial T_i}\right)_\rho \frac{\partial T_i}{\partial t} = -4\pi P_i \frac{\partial}{\partial m}\left(r^2 u\right) - \frac{1}{\rho}\nu_{ie} k_b \left(T_i - T_e\right), \tag{5}$$

$$\partial \mathbf{X}/\partial t = f(T_e, \rho, \mathbf{X}). \tag{6}$$

Here, u is the velocity; ρ is the density; T_e and T_i are the electron and ion temperatures; P_e and P_i are the electron and ion pressures (with artificial viscosity; see below); E_e and E_i are the thermal energies of the gas element with a mass coordinate m (corresponding to the mass within the radius r) at time t; $F_{\rm cond}$ is the energy flux due to electron–electron and electron–ion thermal conduction; ν_{ie} is the electron–ion collision frequency per unit volume; ε_r is the specific energy loss rate by the gas element via radiation; $\partial \varepsilon_{\rm ion}/\partial t$ is the change in the specific thermal energy of the gas due to the change in ionization state; $X_e = n_e/n_b$ is the electron-to-baryon number ratio per unit volume; and $\mathbf{X} = \{X_{\rm HI}, X_{\rm HII}, X_{\rm HeI}, \ldots, X_{\rm NiXXIX}\}$ is the concentration vector of all the ions of all the included elements relative to the total number of atoms and ions. Below, we consider in detail the physical processes included in these equations and show how important their allowance is when modeling the radiation in young SNRs.

To solve the system of equations (1)–(6), we used an implicit finite-difference method that we developed. The use of lines for the hydrodynamic equations, in which the spatial derivatives are substituted with finite differences and the emerging system of ordinary differential equations is solved by Gear-type multistep predictor–corrector methods (see Gear 1971; Arushanyan and Zaletkin 1990), underlies this method. Previously, we used a similar method to compute the light curves of supernovae, and its detailed description can be found in the paper by Blinnikov *et al.* (1998). Our problem differs from that described by Blinnikov *et al.* (1998) by the absence of multigroup transfer equations (we assume the ejection and the swept-up interstellar gas to be transparent, so any emitted photon escapes from the system). The entire heat exchange proceeds in the approximation of thermal conduction according to Eq. (4), which is also effectively solved by the method of lines consistent with hydrodynamics. However, compared to the work by Blinnikov *et al.* (1998), the problem under consideration is significantly complicated by the need for a kinetic calculation of the ionization state for the gas in each zone.

The time it takes for a time-independent ionization to be established after the passage of the shock front through a gas element under the conditions typical of young SNRs exceeds several hundred years. Therefore, the time-dependent ionization must be computed to model the radiation of historical Tycho-like SNRs. Since the radiation in a heavy-element-rich ejection can affect the dynamics even in young SNRs (see below), it is improper first to perform a hydrodynamic SNR calculation (as was done, e.g., by Badenes *et al.* 2003), preserving the density and temperature history, and only then to compute the ionization state from these data. We had to include the ion kinetic calculation in the general scheme. The physical aspect of the kinetics of a moving multicharged plasma was described, for example, in the book by Borovskiĭ *et al.* (1995). The computational aspect of this problem is far from trivial. We solved the kinetic problem as follows by ensuring full consistency between hydrodynamics and kinetics:

At each step in time, the hydrodynamic predictor yields the evolution of T and ρ in each Lagrangian zone in the form of polynomial fits up to the fourth order in time t. Knowing the ion concentrations from the previous step, we obtain their new values at the next step by solving the system of kinetic equations using the interpolating polynomial for T and ρ specified by the hydrodynamic predictor. We solved the kinetic equations using a different predictor–corrector

algorithm (as well as Gear's method) by enabling it to make the necessary number of steps to calculate the new concentrations with a given accuracy. Subsequently, we substituted them together with the predicted hydrodynamic variables into the right-hand sides of the equations with which the hydrodynamic corrector then worked. If the predictor and corrector results diverged, then the procedure was repeated with a reduced step or order of the method. In the case of successful convergence, we considered the possibility of an automatic increase in the step or order of the method.

The kinetic calculations were performed for all species of the fifteen most abundant elements in space (H, He, C, N, O, Ne, Na, Mg, Al, Si, S, Ar, Ca, Fe, Ni) by taking into account the electron-impact ionization, autoionization, photo- and dielectronic recombination, and charge exchange (Arnaud and Rothenflug 1985; Verner and Yakovlev 1990; Verner and Ferland 1996; Seaton 1959; Shull and Steenberg 1982; Nussbaumer and Storey 1983).

Electron Thermal Conduction

We took the thermally conductive flux in Eq. (4) to be

$$F_{\rm cond} = -\frac{k_e \nabla T}{1 + |k_e \nabla T|/F_{\rm sat}}. \qquad (7)$$

Here, we took into account the fact that the electron energy E_e could not be transferred with a speed higher than the speed of sound in an ion or electron gas, c_{si} or c_{se}, depending on which of these speeds is lower (in most cases, this is the ion speed; see, e.g., Bobrova and Sasorov 1993). In this way, we can indirectly take into account the electrical neutrality of the plasma as a whole (Imshennik and Bobrova 1997). Thus, the thermally conductive flux for any temperature gradient cannot be higher than its saturated value of $F_{\rm sat} = E_e \min(c_{si}, c_{se})$.

The electron thermal conductivity from Eq. (7) includes both the electron–electron and electron–ion thermal conduction. It is (Spitzer and Härm 1953)

$$k_e = \frac{2k^{7/2}T^{5/2}\xi(Z)}{e^4 m_e^{1/2} Z \ln\Lambda}\left(\frac{2}{\pi}\right)^{3/2}, \qquad (8)$$

where k is the Boltzmann constant; e and m_e are the electron charge and mass, respectively; and Z is the mean ion charge. According to Spitzer and Härm (1953) (see also Borkowski *et al.* 1989), we calculated the latter using the formula

$$Z = \sum_{i,j} n_{i,j} Z_{i,j}^2 \Big/ \sum_{i,j} n_{i,j} Z_{i,j}, \qquad (9)$$

where the sums are taken over all ions of all chemical elements. The Coulomb logarithm was taken from Cohen *et al.* (1950):

$$\ln\Lambda = \ln\left\{\frac{3}{2e^3 Z}\frac{(kT)^{3/2}}{[\pi n_e (1+Z)]^{1/2}}\right\}. \qquad (10)$$

The function $\xi(Z)$ in (8) is of the order of unity. We took the expression for it from the paper by Borkowski *et al.* (1989) (see also Max *et al.* 1980):

$$\xi(Z) = 0.95\,\frac{Z + 0.24}{1 + 0.24Z}. \qquad (11)$$

The values of $\xi(Z)$ calculated using this formula are in good agreement with those obtained by Spitzer and Härm (1953).

Thermal conductivity reaches its saturated value of $F_{\rm sat}$ even at small temperature gradients, because the electron mean free path relative to collisions with ions is large (Imshennik and Bobrova 1997):

$$\lambda \sim (kT_e)^2/(Ze^4 n_e \ln\Lambda) \sim 10^4 T_e^2/Z n_e\,[\rm cm], \qquad (12)$$

where Z is the mean change determined above. The mean free path λ accounts for an appreciable fraction of the SNR radius at $T_e \sim 10^7\,\rm K \sim 1$ keV and can formally even exceed it at higher temperatures. In the next section, we assess the role of a magnetic field that effectively reduces the electron mean free path.

Note that the ion temperature T_i in a two-temperature plasma can be so high that ions contribute appreciably to the thermal conductivity (Bobrova and Sasorov 1993). We have not yet taken this effect into account (as in other astrophysical works on SNRs), but its consideration deserves the attention of theorists.

Radiative Losses

The importance of radiative losses in a heavy-element-rich supernova ejection was emphasized by Hamilton and Sarazin (1984b). These authors showed that thermal instability and runaway cooling of the ejection could develop even at early evolutionary phases of the SNR, for example, at the ejection parameters that correspond to the Tycho SNR. Nevertheless, in subsequent works on modeling the radiation from the Tycho SNR (Itoh *et al.* 1988; Brinkmann *et al.* 1989; Badenes *et al.* 2003), the radiative losses were disregarded.

Our calculations completely take into account the radiative losses both in the interstellar medium and in the ejection and confirm the conclusions reached by Hamilton and Sarazin (1984b) that these losses cannot be ignored without a special test, even for young SNRs. Figure 1 shows, for the W7 and MR0 models, the evolution of the thermal energy and the

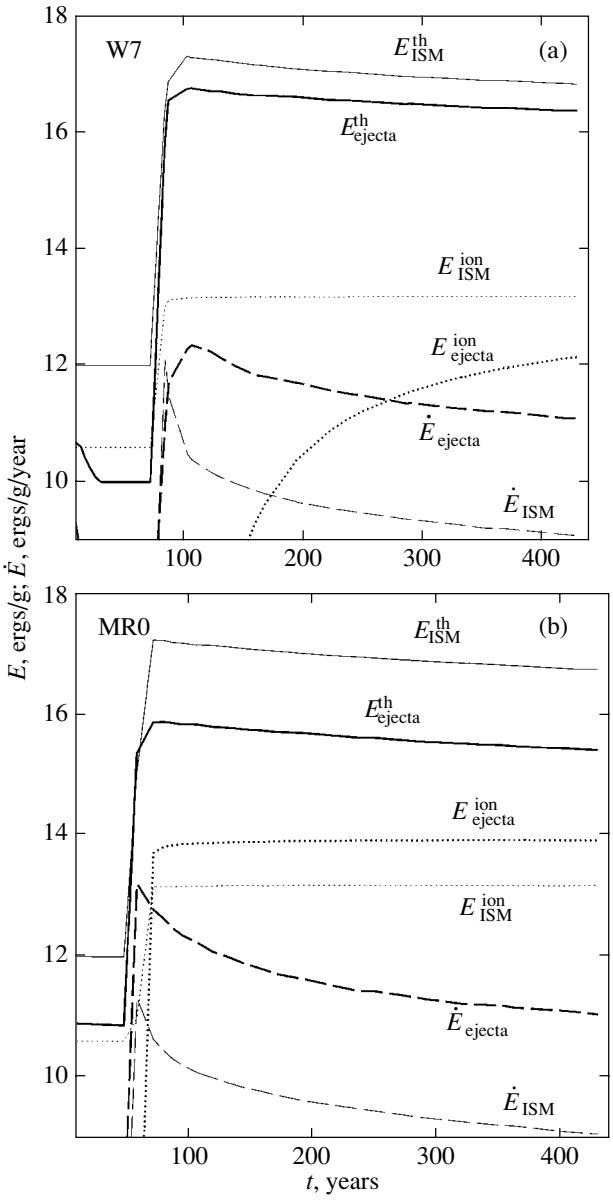

Fig. 1. Evolution of the thermal energy (solid lines), the energy spent on ionization (dotted lines), and the energy radiated in a year (dashed line) in one of the numerical zones of the ejection and the ambient medium for the (a) W7 and (b) MR0 models. All of the energies are shown on a logarithmic scale.

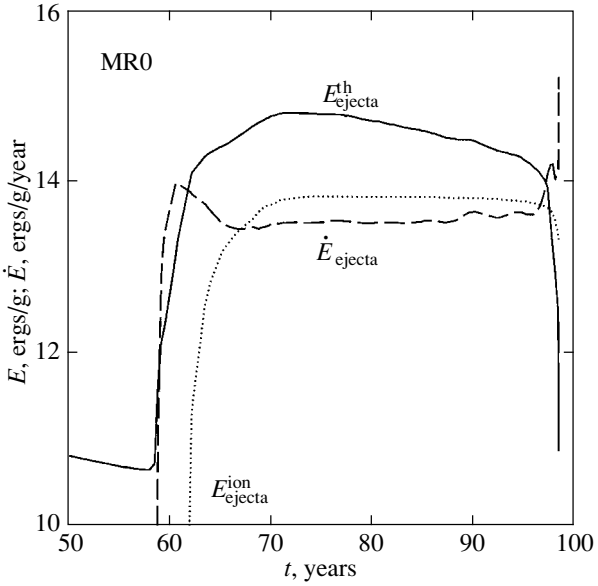

Fig. 2. Same as Fig. 1 for the MR0 model, but the density in the displayed zone was increased by a factor of 10, which leads to the growth of thermal instability in this zone in less than 100 yr. Here, the model with $T_e = T_i$, and the energies on a logarithmic scale.

rate of its change in two Lagrangian zones, one belongs to the ejection and the other belongs to the interstellar medium. The zones were chosen so that they were simultaneously heated by the reverse and forward shocks and a significant amount of iron was contained in the chosen ejection zone. The models were computed up to the age of the Tycho SNR, which is about 430 yr. We see from Fig. 1 that the characteristic cooling ($E/\dot{E}$) time scale for a gas element in the interstellar medium is very large, $\sim 10^7$ yr. In the ejection, the thermal energy is an order of magnitude lower, while the losses are two orders of magnitude higher; i.e., they may still be considered small for the two models under consideration.

However, it should be remembered that we have to average the radial density distribution for our one-dimensional code. In reality, the supernova ejection can be essentially three-dimensional, so there are dense clumps in the rarefied matter whose cooling rate is appreciably higher than that of the matter on average. Such clumps can lose energy on the order of the thermal energy even by the age of the Tycho SNR.

We can illustrate such cooling by artificially increasing the density in one of the outer zones in our models. The outer zones of the MR0 model are rich in iron, which increases the cooling rate. A threefold increase in density in one of these zones leads to faster cooling than in the original model; still, the cooling time is more than 1000 yr. A tenfold increase in density leads to the growth of thermal instability in this zone in less than 100 yr. This is clearly seen from Fig. 2, which shows the thermal evolution of the zone with increased density in the MR0 model with $T_e = T_i$. Our calculations also indicate that, in the model with $T_e \neq T_i$ the extra heating of the electrons through heat exchange with the ions that are heated much more strongly at the shock does not give stabilization: instability grows at the same SNR age. In contrast, thermal conduction can inhibit the growth of thermal instability in the electron gas.

Table 2. Main cases of calculations for each model (W7 and MR0)

Case	$C_{\rm kill}$	q_i
basic	1	1
C	10^{-15}	1
q	1	0.5
Cq	10^{-15}	0.5

Since the outer layers of the W7 model consist of a carbon–oxygen mixture, they cool more slowly. In addition, the expansion velocity in W7 is higher than that in MR0. Hence, its density drops faster, which also increases the cooling time. For these reasons, we failed to obtain thermal instability in this model in 1000 yr.

Thus, in the one-dimensional models we considered, the cooling proved to be not very significant for a Tycho-age SNR. However, for models with a flatter density distribution, a lower kinetic energy, or in the three-dimensional case, the cooling in an ejection with clumps of gas in the outer layers can be significant, and the losses cannot be considered negligible on a time scale of several hundred years.

Energy Exchange between Electrons and Ions

During the passage of a shock front, ions heat up more strongly than electrons, and their temperature T_i breaks away from T_e. The front structure with thermal conduction at $T_i \neq T_e$ was studied in detail by Imshennik (1962) and Imshennik and Bobrova (1997). For purely collisional (Coulomb) thermal energy exchange, the temperature equilibration rate in Eqs. (4) and (5) is given by

$$\nu_{ie} = \frac{2^{5/2}\pi^{1/2}e^4 n_i n_e Z_i^2 \ln\Lambda}{m_i m_e k_b^{3/2}\left(T_i/m_i + T_e/m_e\right)^{3/2}}.$$

The question as to the role of collisionless processes in the energy exchange between the plasma components has not yet been solved. As was shown by McKee (1974), the plasma instabilities at the front can be so strong that the temperatures can become equal; according to the calculations by Cargill and Papadopoulos (1988), $T_e > T_i$ in certain cases (see also Lesch (1990), who discussed an efficient T_e and T_i equilibration mechanism). On the other hand, the interpretation of the observations for the young SNR 1006 by Laming *et al.* (1996) indicates that the electron temperature remains well below the ion temperature. The same conclusion ($T_e < 0.1 - 0.2T_{\rm mean}$) was reached by Hwang *et al.* (2002) regarding the Tycho SNR, but they did not rule out the presence of a distinct nonthermal tail in the electron distribution either.

To describe the effects of collisionless energy exchange, we used the following approach. We introduced a parameter q_i that specifies the fraction of the artificial viscosity Q added to the ion pressure in Eqs. (3)(5): $P_i = P_i(\text{thermal}) + q_i Q$; for the electron component, $P_e = P_e(\text{thermal}) + (1 - q_i)Q$. If only the collisional exchange is included, then $q_i = 1$ and we obtain the standard system of equations with the heating of only ions at the front (Maiorov 1986).

X-RAY EMISSION FROM SNRs UNDER VARIOUS PHYSICAL ASSUMPTIONS

For each supernova model, we computed the SNR evolution under various assumptions, because the role of plasma effects, magnetic fields, etc. is not yet completely clear. In our calculations, the main cases corresponded to the following assumptions. In all cases, the ionization kinetics was fully taken into account. The losses through radiation: free–free, i.e., bremsstrahlung, recombinational, and bound–bound (in X-ray lines), was taken into account at each time for the set of ions available at this time. Thus, the radiation depended not only on the density and temperature, but also on the preceding evolution of the ion composition. The computed SNR spectra were folded with the EPIC PN/XMM-Newton detector response matrix using the XSPEC software package (Arnaud 1996).

Such processes as the thermal conduction, the plasma heating in shocks, and the rate of heat exchange can depend on magnetic field and plasma instabilities. Therefore, their influence, for example, on the mean free path, was simulated by varying the parameter q_i and introducing the factor $C_{\rm kill}$ of $F_{\rm cond}$ in Eq. (4). The factor $C_{\rm kill}$ ($0 \leq C_{\rm kill} \leq 1$) describes the fraction of the thermal flux contributed to the system compared to the standard case (7), where the flux is limited only by the existence of a maximum speed (the speed of sound) for the heat carriers without a possible decrease in the particle mean free path due to the magnetic field and plasma instabilities.

Despite all the uncertainty of the physical processes, we should take into account the fact that there must be relationships between them. For example, the presence of a magnetic field reduces sharply the particle mean free path: in place of the Coulomb mean free path (12), we should use the Larmor radius $r_{\rm L} = mcu/eB$. Even for weak fields ($B \sim 10^{-6}$ G), $r_{\rm L} \ll \lambda$, i.e., $C_{\rm kill}$ should be decreased. At the same time, the presence of a magnetic field most likely leads to the growth of plasma instabilities at the front, implying

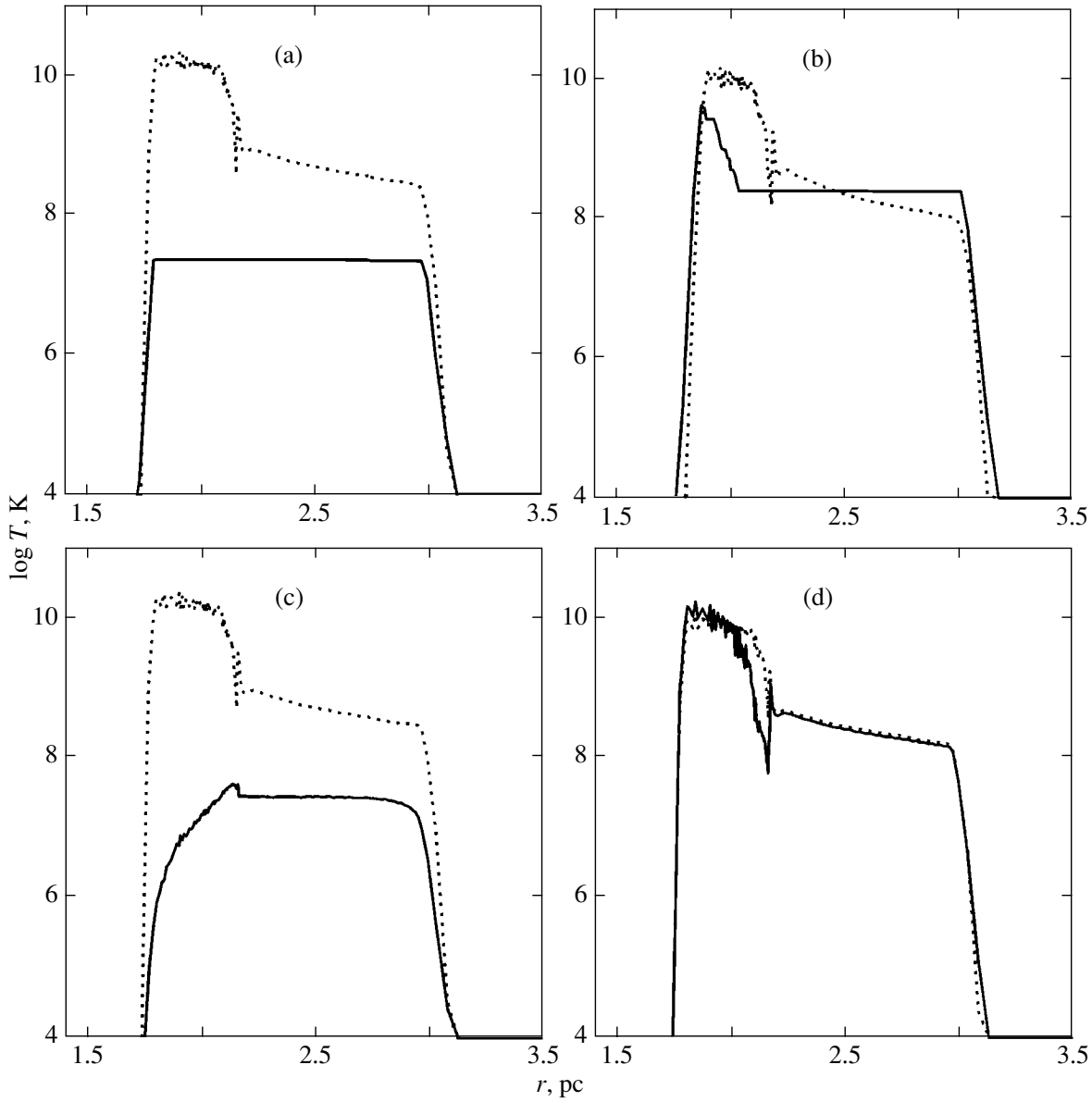

Fig. 3. Ion (dotted lines) and electron (solid lines) temperature distributions in the W7 models for four sets of parameters q_i and $C_{\rm kill}$: (a) basic set, (b) q, (c) C, and (d) Cq.

that the electron heating increases there, and the parameter q_i must decrease.

We considered the case without a magnetic field ($C_{\rm kill} = 1$, $q_i = 1$) to be the basic one. We also performed calculations with a reduced $C_{\rm kill}$ and $q_i = 0.5$. A detailed list of cases and their parameters are given in Table 2. Case Cq can be interpreted as a full allowance for the possible effect of a magnetic field: it causes extra collisionless heating of the electrons at the shock front, so that the post-shock electron and ion temperatures become almost equal, and reduces significantly the electron mean free path by suppressing the thermal conduction. In case C with a magnetic field, the thermal conduction is also suppressed, but it does not lead to extra non-Coulomb heating at the front for several reasons. In case q, the electron heating at the front can be attributed to plasma instabilities unrelated to the magnetic field; in this case, the thermal conduction is fully taken into account according to Eq. (7). These four cases may be considered as the limiting ones that restrict the entire variety of possibilities encountered in actual SNRs.

Figures 3 and 4 show the radial distributions of the electron and ion temperatures for the W7 and MR0 models for an age of 430 yr after the explo-

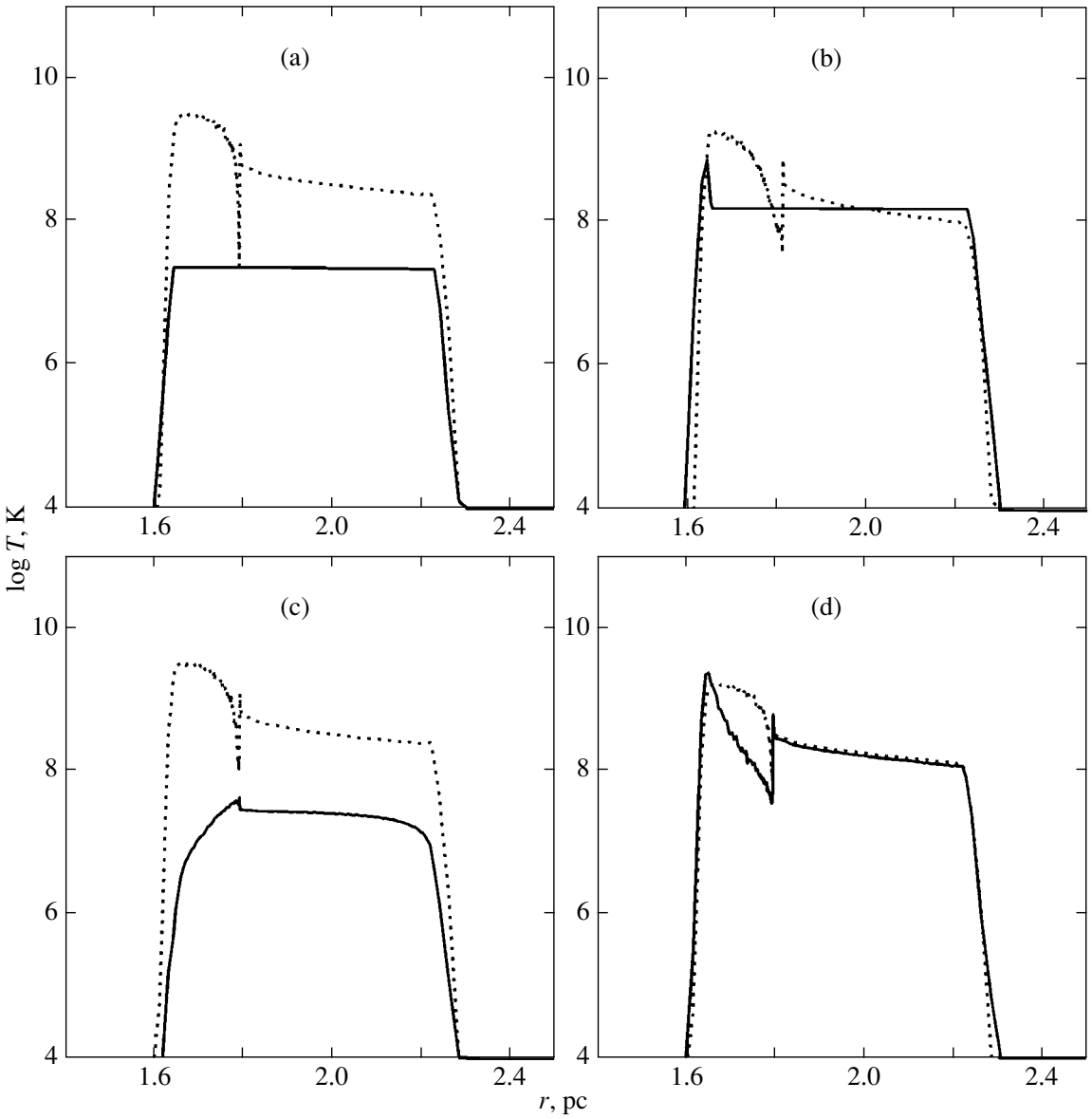

Fig. 4. Ion (dotted lines) and electron (solid lines) temperature distributions in the MR0 model for four sets of parameters q_i and $C_{\rm kill}$: (a) basic set, (b) q, (c) C, and (d) Cq.

sion, which roughly corresponds to the age of the Tycho SNR. The behavior of the electron temperature in the ejection well reflects our physical models, and the overall structure of the ejection is similar for the two explosion models. We clearly see from the figures how significant the electron thermal conduction can be in young SNRs. Thus, in our basic model with cold electrons at the front and without suppression of the thermal conduction, the electron temperature between the primary and reverse shocks is completely equalized. For strong electron heating at the front, the picture is approximately the same; only a small electron temperature peak is observed in the zone behind the reverse shock. Since this spike is moderately long and the electron temperature rapidly reaches the value common to the entire SNR, this is unlikely to affect appreciably the ionization rate behind the shock front, but, of course, the equilibrium ionization state is higher due to the larger dissipation and the higher electron gas temperature at the shock front. The case with strong electron heating and suppressed thermal conduction would have led to the same distribution of the electron and ion temperatures if radiative losses had not played a prominent role. However, as we see from the figures, the electron temperature in the ejection near the contact discontinuity is appreciably lower than the ion temperature. The radiative losses

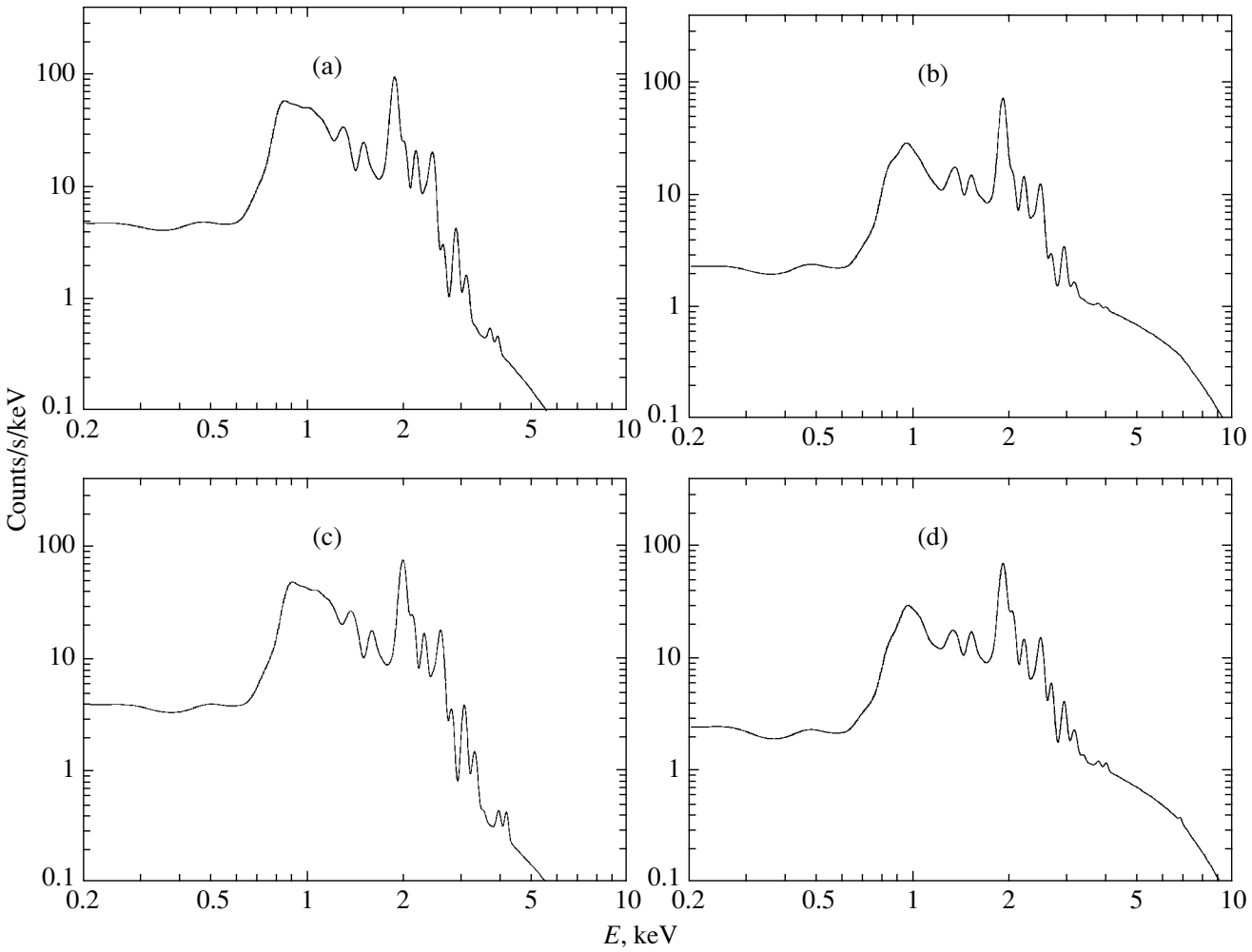

Fig. 5. Spectra for the W7 model folded with the EPIC PN/XMM-Newton detector response matrix: (a) $W7_{basic}$, (b) $W7_{q}$, (c) $W7_{C}$, and (d) $W7_{Cq}$.

are particularly important in the MR0 model with higher metallicity, for the outer layers, and density.

The temperature of the shock-heated interstellar medium for any physics differs by no more than an order of magnitude, while this difference in the ejection is much larger; therefore, one might also expect an appreciable effect of the physics on the radiation. Nevertheless, the integrated spectra (Figs. 5 and 6) prove to be almost insensitive to the physics, except for the continuum level and the small differences in the ratios of certain spectral lines). This is probably because the ionization in a SNR of such an age is time dependent. Although the time-independent ionization rates differ markedly, the ionization rates are similar for all models, while the differences in the spectrum being studied can be explained mainly by different chemical compositions and radial distributions of chemical elements in different models. Since iron lies deeper in W7 than in MR0, it is ionized later when the ejection density dropped appreciably due to the expansion (with a higher velocity). The ionization rate is much lower because the density is lower. As we see from Fig. 7, Fe XXI and Fe XXV are the highest iron ions in W7 and MR0, respectively, in the outer zones where iron is present in appreciable amounts and ionized most strongly. This is the reason why there are significant differences between the spectra for different explosion models.

A clear feature that distinguishes MR0 from W7 is the absence of $K\alpha$ iron lines in the W7 spectra in all four cases from Table 2 (the same is true for single-temperature hydrodynamics, $T_e = T_i$).

In our list of lines, the $K\alpha$ iron line is presented only for Fe XXIV–Fe XXVI. Therefore, it comes as no surprise that this line is clearly seen in the theoretical spectrum (Fig. 6) in the MR0 model where

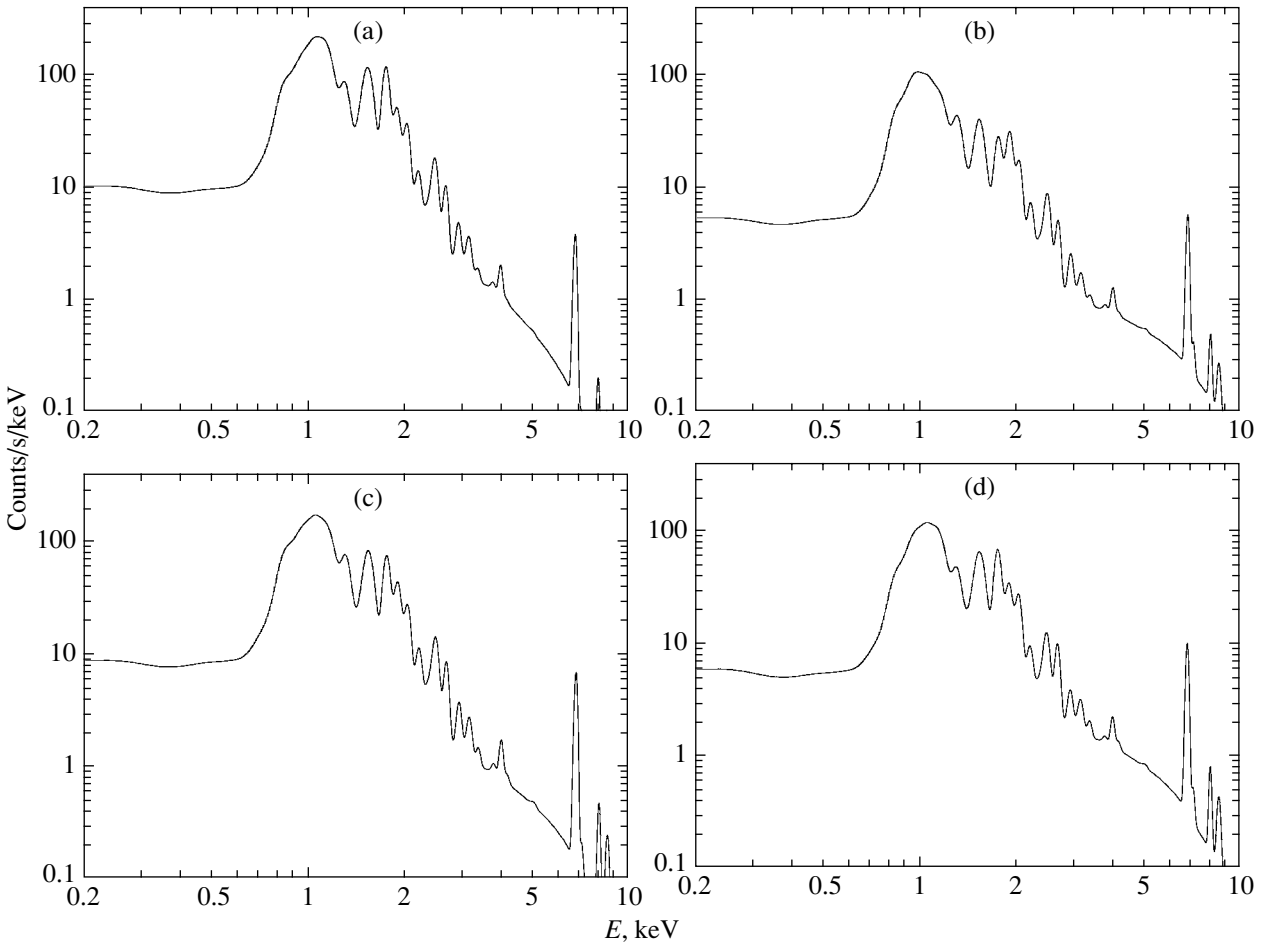

Fig. 6. Same as Fig. 5 for the MR0 model.

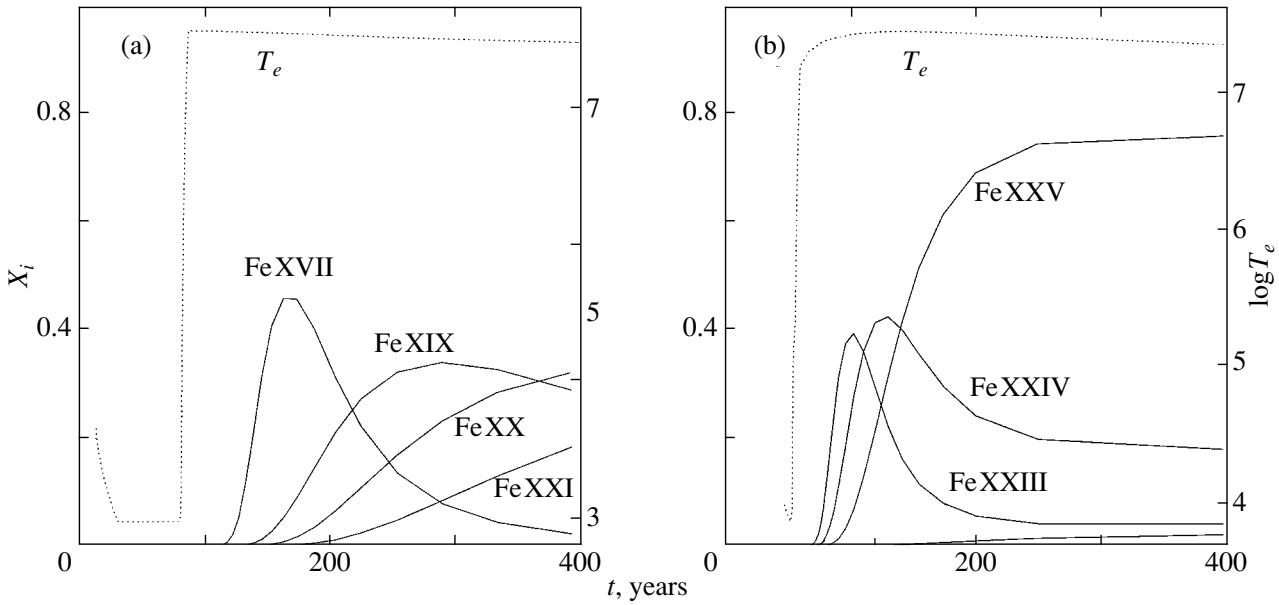

Fig. 7. Iron ionization kinetics in the (a) W7 and (b) MR0 models in the outermost iron-rich layers of the ejection ($1.02M_\odot$ for W7 and $1.37M_\odot$ for MR0). In the MR0 model, we see the appearance of a hydrogenic Fe XXVI ion. The dotted line indicates the evolution of the electron temperature in these zones.

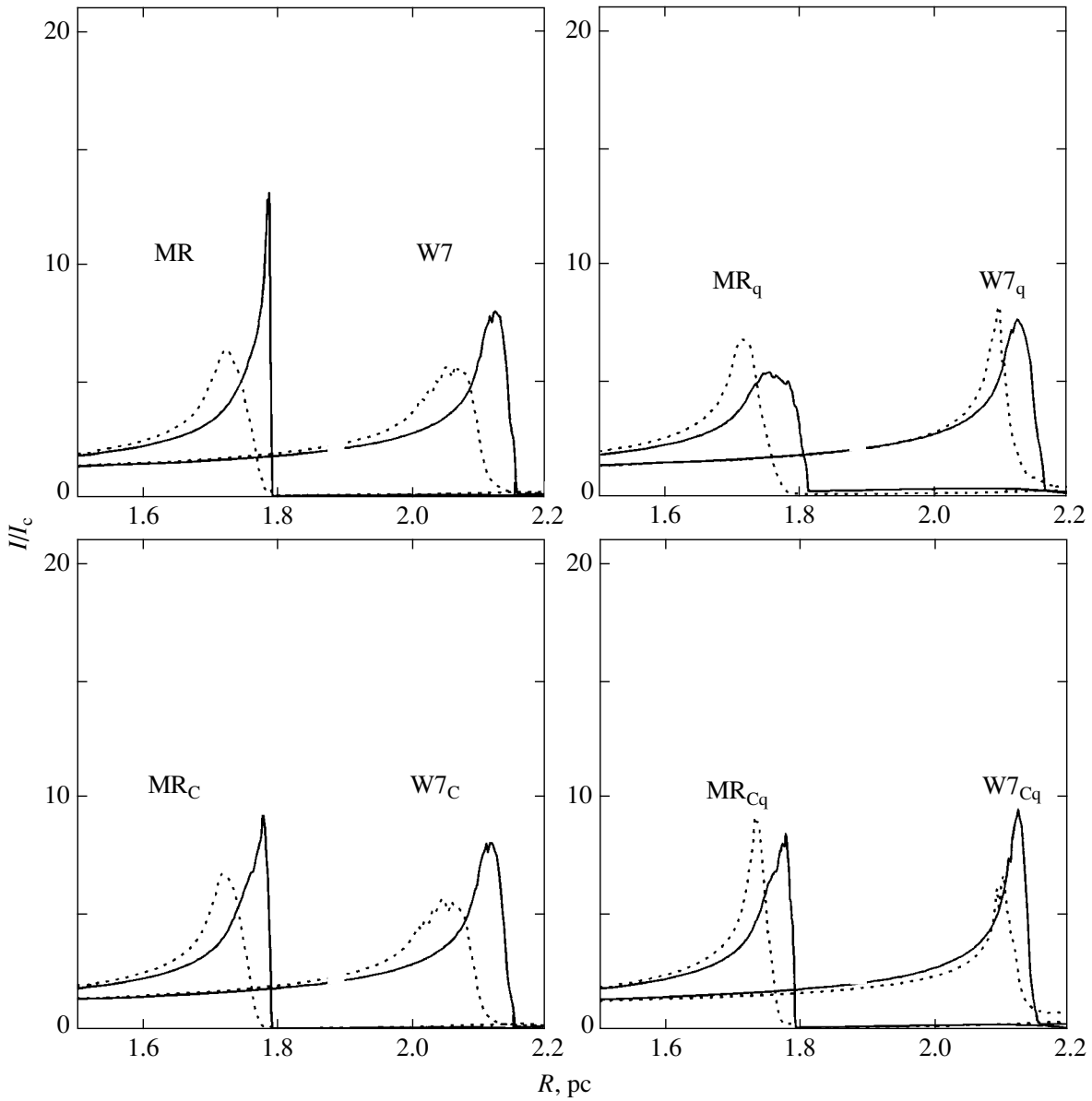

Fig. 8. Si XIII (solid lines) and Fe XVII (dotted lines) line intensity distributions over the SNR relative to the intensity in the same lines at the center for the W7 and MR0 models.

the ionization reaches these high ions (see Fig. 7). In the W7 model, the ionization reaches only Fe XXI (Fig. 7). However, it is interesting to assess the role of the excitation of such iron ions with several L-shell electrons: the question remains as to whether the $K\alpha$ line of iron ions will appear as they are excited from the inner K shell.

Clearly, in standard models with $T_e \sim 1$ keV, the excitation of the innermost electrons is suppressed compared to the ionization of outer electrons by the exponential factor $\exp(-\Delta E/T_e)$, where $\Delta E \sim 7$ keV is the transition energy. In hot models, the question remains as to whether the excitation or even the knocking out of K electrons followed by the emission of $K\alpha$ photons is possible at high mean thermal electron energies or in the presence of a noticeable nonthermal tail in their distribution. Nevertheless, it seems to us that the flux of such photons in W7 is much lower than that in MR0.

It is not easy to find atomic data on the inner transitions for iron with several electrons, although such work has been done both experimentally and theoretically (see, e.g., Goett *et al.* 1984; Zhang *et al.* 1990; Ballance *et al.* 2001; Whiteford *et al.* 2002). To place

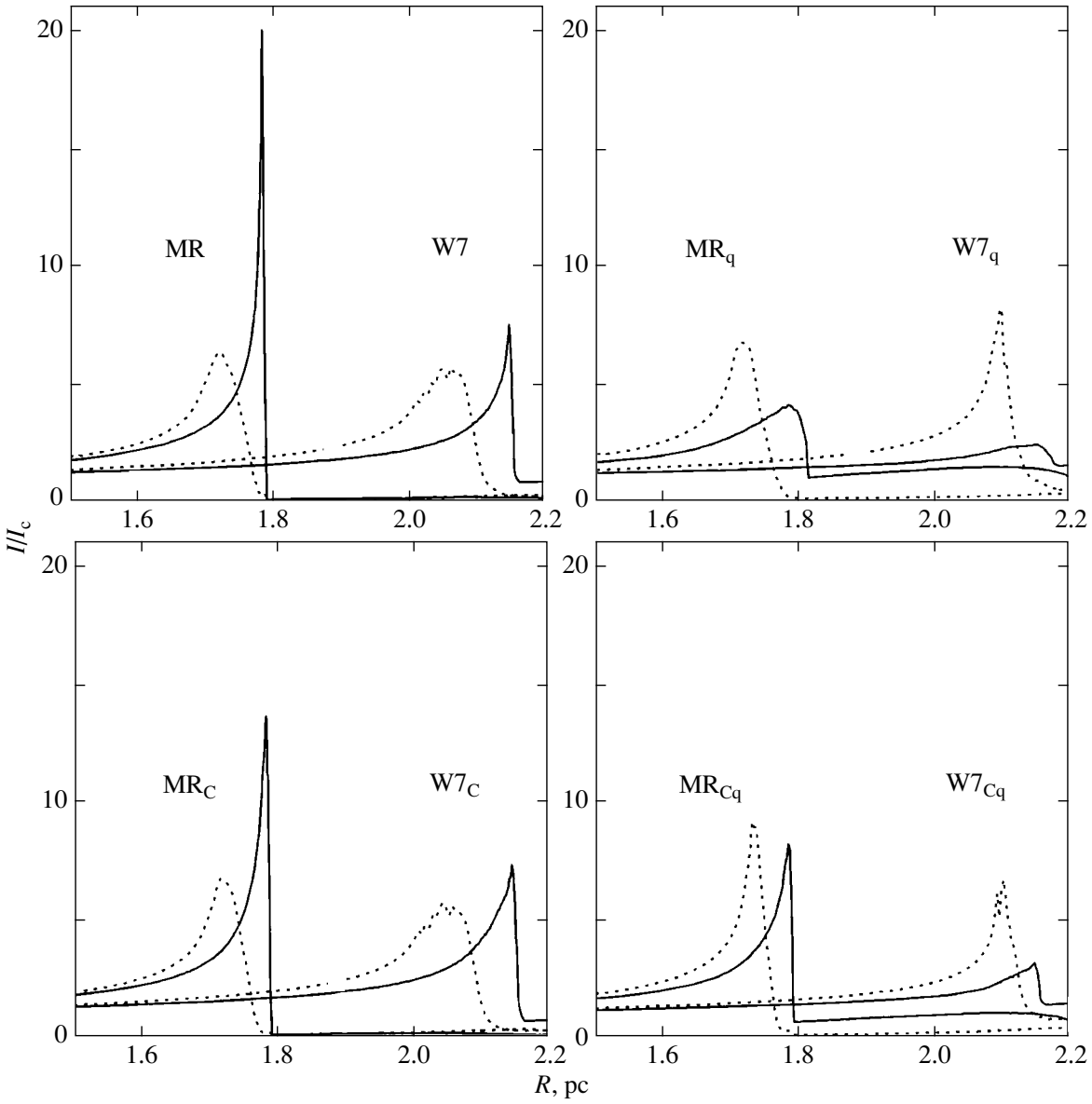

Fig. 9. Fe K (solid lines) and Fe XVII (dotted lines) line intensity distributions over the SNR relative to the intensity in the same lines at the center for the W7 and MR0 models.

an upper limit on the impact excitation rate $\langle\sigma v\rangle$ of a transition, we use simple formulas by van Regemorter (1982) (see formula (14.49) from the book by Vainshtein *et al.*, 1979):

$$\langle\sigma v\rangle \sim 6\times10^{-8} f_{12}\left(\frac{Ry}{\Delta E}\right)^{3/2}\beta^{1/2}\exp(-\beta),$$
$$\beta = -\Delta E/T_e,$$

where f_{12} is the oscillator strength of the $1\rightarrow2$ transition, $Ry = 13.6$ eV. In this form, this formula is valid for $\beta > 1$ and agrees well with the more accurate formula (9) from the paper by Sampson and Zhang (1988). We find from this formula at $T\sim$ 10–20 keV, typical of the $K\alpha$ iron line formation zone in hot models, that $\langle\sigma v\rangle \sim 10^{-12}\mathrm{cm}^3/\mathrm{s}$ if we take the largest values of $f_{12}\sim0.4$, as in the resonance $K\alpha$ transition of the hydrogenic Fe XXVI ion. For the inner transitions, for example, in Fe XX, the value of f_{12} is appreciably lower, and, most importantly, the electron density n_e in the Fe XX excitation region in W7 is an order of magnitude lower than that in MR0; i.e., the excitation probability of each ion, $n_e\langle\sigma v\rangle$, is much lower in W7, which confirms our conclusion about the low probability of the $K\alpha$ iron lines being observable in this model.

Observations by Decourchelle *et al.* (2001) indi-

cate that this line is prominent in the Tycho SNR, but it is still weaker than that in the MR0 model. The actual ejection must probably be slightly less mixed and rapidly expanding than in MR0 or, conversely, less energetic and more mixed than in W7.

On the other hand, the W7 model better reproduces the observations from the viewpoint of the ratio between the Si XIII (~2 keV) and Fe XVII (~ 0.8 keV) blends. However, in this case, a slightly more energetic and less mixed ejection could also rectify the situation for MR0.

Thus, an analysis of the spectra makes it possible to choose an explosion model that better reproduces the observations and, hence, to understand which explosion mechanism is realized in nature, but it is difficult to determine what physical processes are important inside a young SNR from the spectra. On the other hand, the surface brightness profiles in narrow-band filters corresponding to certain lines of the X-ray spectrum can provide us with this opportunity. Figure 8 shows the Si XIII (1.67–2 keV) and Fe XVII (775–855 eV) line profiles for four cases of both models, while Fig. 9 shows the same profiles for the models in Fe K (6.2–6.6 keV) and Fe XVII lines. The profiles in each line are shown relative to *its* central intensity. Their behavior (except for the Fe K line, which is almost absent in W7) when the physical parameters are changed is similar for both models, although the relative positions of the emitting rings in different lines do not coincide with the one observed.

CONCLUSIONS

We have performed for the first time hydrodynamic modeling of the evolution of young supernova remnants with a self-consistent allowance for the time-dependent ionization kinetics in a two-temperature plasma and the electron thermal conduction. We phenomenologically took into account the influence of a magnetic field on the thermal conduction and modeled the effective electron heating at the shock front through plasma processes. A large change in thermal conduction parameters was shown to have a negligible effect on the X-ray spectra that we obtained by taking into account all of the major elementary processes and by folding the theoretically predicted spectra with the EPIC PN/XMM-Newton detector response matrix.

One of our most important results is that the influence of radiative losses on hydrodynamics must be taken into account at the earliest evolutionary phases of SNRs. Thus, we have resolved the contradiction that has existed for twenty years between the results by Hamilton and Sarazin (1984b), who showed the possibility of thermal instability growing in a metal-rich ejection, and the complete neglect of this effect in other works on hydrodynamic modeling of young SNRs. In the models we considered, thermal instability grows to the point of runaway cooling in about a thousand years for a threefold density increase in one of the zones and in less than 100 years for a ten-fold density increase. In real three-dimensional models and when the ejection interacts with the possible circumstellar matter, thermal instability can begin to grow much faster.

Until now, our goal has not been to choose the best model to describe actual SNRs. However, our calculations of the X-ray spectra indicate that supernova models that lead to the production of iron in the outermost layers such as those obtained by Dunina-Barkovskaya *et al.* (2001) and Reinecke *et al.* (2002) are most promising for describing the observed iron lines.

The most important effect of those that we disregarded is, of course, the full three-dimensional calculation of the hydrodynamics. The generation of nonthermal particles at shock fronts and the evolution and hydrodynamic influence of magnetic fields should be investigated on a more physical basis. Nevertheless, it seems to us that in any further development of the SNR theory, the effective algorithm of a self-consistent relationship between hydrodynamics and ionization kinetics will retain its significance.

ACKNOWLEDGMENTS

We wish to thank P.V. Sasorov for numerous helpful discussions and V. Zhakhovskoi for his help in organizing the calculations. This work was supported by the Russian Foundation for Basic Research (project no. 02-02-16500) and by grants from the Swedish Royal Academy of Sciences at Stockholm Observatory, Albanova. We are also grateful to W. Hillebrandt for his support at Max Planck Institut für Astrophysik (Garching, Germany).

REFERENCES

1. K. A. Arnaud, ASP Conf. Ser. **101**, 17 (1996); http://xspec.gsfc.nasa.gov/docs/xanadu/xspec/index.html.
2. M. Arnaud and R. Rothenflug, Astron. Astrophys., Suppl. Ser. **60**, 425 (1985).
3. O. B. Arushanyan and S. F. Zaletkin, *Numerical Solution of Ordinary Differential Equations using Fortran* (MGU, Moscow, 1990) [in Russian].
4. C. Badenes, E. Bravo, K. J. Borkowski, and I. Domínguez, Astrophys. J. **593**, 358 (2003).
5. C. P. Ballance, N. R. Badnell, and K. A. Berrington, J. Phys. B: Atom. Molec. Phys. **34**, 3287 (2001).
6. S. I. Blinnikov, R. Eastman, O. S. Bartunov, *et al.*, Astrophys. J. **496**, 454 (1998).
7. S. I. Blinnikov and E. I. Sorokina, Astrophys. Space Sci. **290**, 13 (2004).

8. N. A. Bobrova and P. V. Sasorov, Fiz. Plazmy **19**, 789 (1993).
9. K. J. Borkowski, J. M. Shull, and C. F. McKee, Astrophys. J. **336**, 979 (1989).
10. A. V. Borovskiĭ, S. A. Zapryagaev, O. I. Zatserinnyĭ, and N. L. Manakov, *Multi-Charged Ion Plasma* (Khimiya, St.-Petersburg, 1995).
11. W. Brinkmann, H. H. Fink, A. Smith, and F. Haberl, Astron. Astrophys. **221**, 385 (1989).
12. P. J. Cargill and K. Papadopoulos, Astrophys. J. **329**, L29 (1988).
13. R. A. Chevalier, Astrophys. J. **258**, 790 (1982).
14. R. S. Cohen, L. Spitzer, Jr., and P. McRoutly, Phys. Rev. **80**, 230 (1950).
15. A. Decourchelle, J. L. Sauvageot, M. Audard, *et al.*, Astron. Astrophys. **365**, L218 (2001).
16. N. V. Dunina-Barkovskaya, V. S. Imshennik, and S. I. Blinnikova, Pis'ma Astron. Zh. **27**, 412 (2001) [Astron. Lett. **27**, 353 (2001)].
17. C. W. Gear, *Numerical Initial Value Problems in Ordinary Differential Equations* (Prentice-Hall, Englewood Cliffs, 1971).
18. S. J. Goett, D. H. Sampson, and R. E. H. Clark, Astrophys. J., Suppl. Ser. **54**, 115 (1984).
19. A. J. S. Hamilton and C. L. Sarazin, Astrophys. J. **281**, 682 (1984a).
20. A. J. S. Hamilton and C. L. Sarazin, Astrophys. J. **287**, 282 (1984b).
21. U. Hwang, A. Decourchelle, S. S. Holt, and R. Petre, Astrophys. J. **581**, 1101 (2002).
22. V. S. Imshennik, Zh. Vychisl. Mat. Mat. Fiz. **2**, 206 (1962).
23. V. S. Imshennik and N. A. Bobrova, *Dynamics of Collisional Plasma* (Énergoatomizdat, Moscow, 1997) [in Russian].
24. H. Itoh, K. Masai, and K. Nomoto, Astrophys. J. **334**, 279 (1988).
25. J. M. Laming, J. C. Raymond, B. M. McLaughlin, and W. P. Blair, Astrophys. J. **472**, 267 (1996).
26. H. Lesch, Astron. Astrophys. **239**, 437 (1990).
27. S. A. Maĭorov, Zh. Vychisl. Mat. Mat. Fiz. **26**, 1735 (1986).
28. C. E. Max, C. F. McKee, and W. C. Mead, Phys. Fluids **23**, 1620 (1980).
29. C. F. McKee, Astrophys. J. **188**, 335 (1974).
30. D. K. Nadezhin, Preprint No. 1, ITÉF (Inst. Theor. Exp. Phys., Moscow, 1981).
31. D. K. Nadezhin, Astrophys. Space Sci. **112**, 225 (1985).
32. K. Nomoto, F.-K. Thielemann, and K. Yokoi, Astrophys. J. **286**, 644 (1984).
33. H. Nussbaumer and J. Storey, Astron. Astrophys. **126**, 75 (1983).
34. M. Reinecke, W. Hillebrandt, and J. C. Niemeyer, Astron. Astrophys. **386**, 936 (2002).
35. D. H. Sampson and H. L. Zhang, Astrophys. J. **335**, 516 (1988).
36. M. J. Seaton, Mon. Not. R. Astron. Soc. **119**, 81 (1959).
37. M. J. Shull and M. Van Steenberg, Astrophys. J., Suppl. Ser. **48**, 95 (1982).
38. L. Spitzer and R. Härm, Phys. Rev. **89**, 977 (1953).
39. H. van Regemorter, Astrophys. J. **136**, 906 (1962).
40. L. A. Vaĭnshteĭn, I. I. Sobel'man, and E. A. Yukov, *Atomic Excitation and Spectral Line Broadening* (Nauka, Moscow, 1979) [in Russian].
41. D. A. Verner and G. J. Ferland, Astrophys. J., Suppl. Ser. **103**, 467 (1996).
42. D. A. Verner and D. G. Yakovlev, Astrophys. Space Sci. **165**, 27 (1990).
43. A. D. Whiteford, N. R. Badnell, C. P. Ballance, *et al.*, J. Phys. B: At. Molec. Phys. **35**, 3729 (2002).
44. H. L. Zhang, D. H. Sampson, and R. E. H. Clark, Phys. Rev. A **41**, 198 (1990).

Translated by V. Astakhov

Astronomy Letters, Vol. 30, No. 11, 2004, pp. 751–758. Translated from Pis'ma v Astronomicheskiĭ Zhurnal, Vol. 30, No. 11, 2004, pp. 827–834.

Optical and X-ray Observations of Thermonuclear Bursts from GS 1826-24 during September–October 2003

A. V. Mescheryakov[1,2*], I. M. Khamitov[3], M. G. Revnivtsev[1,4], R. A. Burenin[1], M. R. Gilfanov[1,4], N. N. Pavlinsky[1], R. A. Sunyaev[1,4], Z. Aslan[3], and E. Gogush[5]

[1]*Space Research Institute, Russian Academy of Sciences, Profsoyuznaya ul. 84/32, Moscow, 117810 Russia*

[2]*Moscow State University, Vorob'evy Gory, Moscow, 119992 Russia*

[3]*TUBITAK National Observatory, Antalia, Turkey*

[4]*Max Planck Institut für Astrophysik, Karl Schwarzschild Str. 1, Postfach 1317, D-85741 Garching, Germany*

[5]*Sabanshi University, Istanbul, Turkey*

Received March 5, 2004

Abstract—The results of optical (the RTT-150 telescope) and X-ray (the RXTE observatory) observations of the burster GS 1826–24 are presented. Emphasis was placed on analyzing the emissions during thermonuclear bursts. The results obtained allowed the size of the accretion disk in GS 1826–24 and the inclination of this binary to be estimated. © *2004 MAIK "Nauka/Interperiodica".*

Key words: *bursters, thermonuclear bursts, optical and X-ray observations.*

INTRODUCTION

The X-ray source GS 1826–24 was discovered on September 8, 1988, from the Ginga satellite (Makino *et al.* 1989) and was subsequently observed often by various orbital observatories. Ten years later, the nature of this source was firmly established thanks to long-term BeppoSAX observations (Ubertini *et al.* 1997, 1999) from August 1996 through October 1998. It proved to be a stable type-I burster, i.e., a binary system with a weakly magnetized neutron star as the compact object, on the surface of which bursts of thermonuclear burning of the matter accreted occur regularly. The interval between successive bursts was found to be almost constant and equal to 5.76 ± 0.03 h (Ubertini *et al.* 1999).

The subsequent BeppoSAX and RXTE X-ray observations of the object during the period 1998–2002 showed that the burst interval gradually decreases, while the X-ray luminosity in quiescence increases (Cornelisse *et al.* 2003; Galloway *et al.* 2004). The interval between successive bursts from the burster in 2000 was 4.10 ± 0.08 h, while the burst quasi-period in July 2002 was 3.56 ± 0.03 h (Galloway *et al.* 2004). The burst profile was almost invariable during this period: an approximately linear rise to the maximum of the light curve (≈ 10 s) and a relatively long (≈ 100 s) exponential decay.

GS 1826–24 is unique among all of the type-I bursters known to date, in that its regular bursts have never been missed since their discovery in 1997 from the BeppoSAX satellite. Based on the burst energetics, recurrence time, and duration, it may be concluded that this source is an example of a hydrogen–helium burster with a nearly solar metallicity, $Z = 0.02$ (Cumming 2003).

The optical companion of GS 1826–24 was discovered in 1994 (Motch *et al.* 1994). Based on the optical observations of June 20, 1996, and August 1, 1997, Homer *et al.* (1998) suggested an orbital period of the binary, 2.1 h, that required observational confirmation. Kong *et al.* (2000) presented the results of their simultaneous optical and X-ray observations of thermonuclear bursts from the burster in June 1998. They found a delay of ≈ 3 s between the X-ray and optical burst fluxes that was assumed to be related to the reprocessing of X rays from a thermonuclear flash in the accretion disk around the neutron star.

In this paper, we present optical observations of the burster GS 1826–24 with the Russian–Turkish 1.5-m telescope (RTT-150) performed almost simultaneously with the X-ray observations from the RXTE satellite.

OPTICAL AND X-RAY OBSERVATIONS

The optical observations of GS 1826–24 were performed with the 1.5-m RTT-150 telescope

*E-mail: gardel@hea.iki.rssi.ru

1063-7737/04/3011-0751$26.00

Table 1. Log of RTT-150 observations of the X-ray binary GS 1826–24 in the fall of 2003

Date, 2003	UT	PSF[a]
Sep. 6	17:42–19:48	1.96
Sep. 7	18:01–20:30	2.00
Sep. 8	17:14–20:26	1.30
Sep. 9	18:08–20:21	1.78
Sep. 10	17:22–20:18	1.37
Sep. 11	17:07–20:15	2.12
Sep. 12	17:48–19:22	1.93
Oct. 16	16:45–17:52	1.45
Oct. 18	16:47–17:44	1.96

[a]The median FWHM of the point spread function (PSF) in arcsecs.

(Turkey, Mount Bakyrlytepe, 2547 m, $2^h01^m20^s$ E, $36°49'30''$ N). The source's field was photometrically observed over the week of September 6 through September 12, and on October 16 and 18, 2003. A log of observations is given in Table 1.

At the latitude of the observatory, GS 1826–24 can be observed only at large zenith distances, $Z > 60°$. Therefore, an R filter was used to reduce the effect of refraction on the photometric measurements. To achieve the highest time resolution, we cut out a 70×70-pixel window with the source and two nearby bright ($\sim 15^m$) stars from the entire CCD field. As a result, the CCD readout time was 4 s. Thus, at an exposure time of 4 s, the time resolution in our data was 8 s. As an example, Fig. 1 shows an image of the GS 1826–24 field with an exposure time of 4 s.

We reduced the observational data using the standard IRAF package and our own software. We performed primary data reduction: the CCD dark current was first subtracted from all images, and they were then divided by a flat field (the twilight sky). Subsequently, we performed difference aperture photometry of the object (a circular aperture $R_{\rm ap} = 1''.5$ in size) as follows: To estimate the magnitude of the object in each image, we measured the magnitudes of the object and the reference star within a given aperture and determined their difference; subsequently, the magnitude of the reference star known from the photometric solution was added to this difference. We took a neighboring bright star (denoted by the letter A in Fig. 1) as the reference star. The optical companion of GS 1826–24 has an R magnitude of $\sim 18^m$. A slightly brighter star lies at an angular distance of about $3''$ from it (Fig. 1). At good seeing, this star contributes only slightly to the aperture photometry of GS 1826–24. For a check, we simultaneously performed PSF photometry of the object using the DAOPHOT package from ASTROLIB IDL. A model PSF was constructed for each image from its bright stars. Subsequently, an $R_{ap} = 2''$ aperture was used to fit the PSF profile to the object and to a nearby faint star, and its value was corrected to the large aperture using the PSFs of the bright field stars.

In this paper, we present the results of our aperture photometry; they match those of the PSF photometry. As an example, Fig. 2 shows the light curves of GS 1826-24 obtained on September 8 and 10, 2003.

The X-ray observations of the binary GS 1826–24 were performed by the RXTE and INTEGRAL observatories as part of a campaign for broadband observations of several compact sources in the Galactic center region. Unfortunately, during its optical RTT-150 observations, the source fell only within the fields of view of the INTEGRAL hard X-ray instruments (with an effective energy range above 20 keV), which are much less sensitive to the emissions from thermonuclear X-ray bursts. Below, we did not use the INTEGRAL data for our study.

Because of the restrictions related to the RTT-150 visibility of the source, we failed to organize strictly simultaneous observations of an X-ray burst. GS 1826–24 was observed from the RXTE satellite at 01:18–2:18 (UT) on September 11, 2003, which was 5 h later than the RTT-150 observation on September 10, 2003. The RXTE observations were processed using the standard LHEASOFT/FTOOLS 5.3 software package following the RXTE GOF recommendations.[1]

RESULTS

The observed R magnitude of the optical companion of GS 1826–24 averaged over the entire observing period is $m_R \approx 18^m.2$. The long-period variability of the optical light curve for GS 1826–24 will be analyzed in a separate paper. In the six observations on September 7, 8, 9, 10 and October 16, 18, 2003, the light curve exhibited optical bursts (the light curves for September 8 and 10, 2003, are shown in Fig. 2). The epochs of maxima of the bursts detected during the optical and X-ray observations are listed in Table 2.

Previous observations of GS 1826–24 showed that the interval between neighboring bursts from the

[1]http://legacy.gsfc.nasa.gov/docs/xte/data_analysis.html

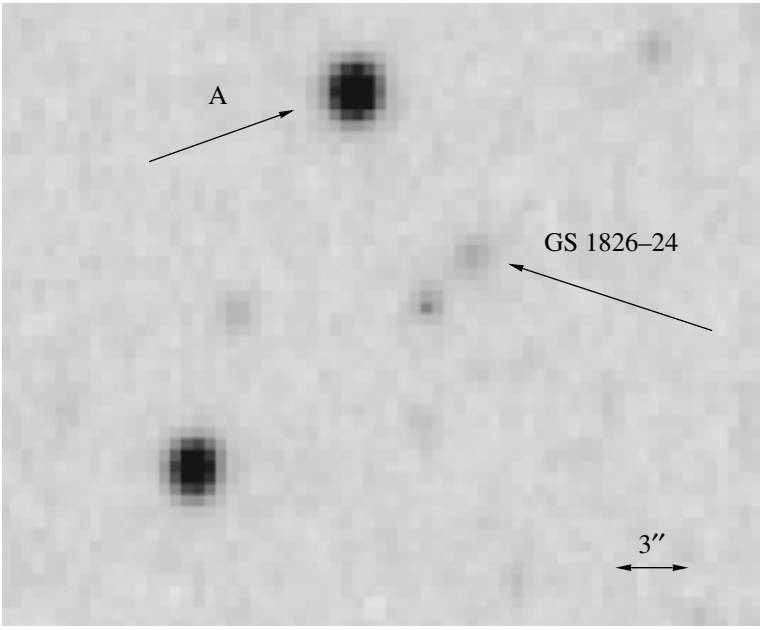

Fig. 1. Image of the GS 1826–24 field with an exposure time of 4 s (arrows indicate the source and the reference star used for difference aperture photometry).

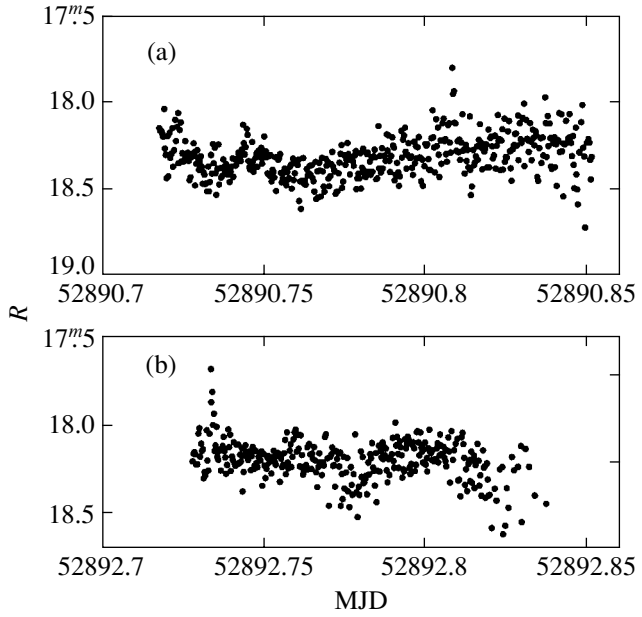

Fig. 2. *R*-band light curves of GS 1826–24 for September 8 (a) and 10 (b), 2003.

burster is constant on time scales of several days or weeks to within several minutes and gradually changes with accretion rate in the binary system (see, e.g., Galloway *et al.* 2004). Using this fact and with the epochs of maxima of the five thermonuclear bursts detected during the simultaneous RTT-150 and RXTE observations in September 2003 (see Table 2), we determined the most probable burst quasi-period for GS 1826–24 in September 2003: 3.85 ± 0.1 h.

Our observations with the 1.5-m telescope do not allow the individual burst profiles to be studied in detail. However, since the X-ray burst profiles for GS 1826–24 are very similar (Galloway *et al.* 2004),

Table 2. Epochs of the maxima of thermonuclear bursts detected at optical and X-ray wavelengths

Date, 2003	Epoch, MJD	Instrument
Sep. 7	52 889.84872	RTT-150, R filter
Sep. 8	52 890.80846	RTT-150, R filter
Sep. 9	52 891.78289	RTT-150, R filter
Sep. 10	52 892.73400	RTT-150, R filter
Sep. 11	52 893.05525	RXTE, 3–20 keV
Oct. 16	52 928.72424	RTT-150, R filter
Oct. 18	52 930.73172	RTT-150, R filter

Table 3. Parameters of the exponential decay fit to the burst profiles in various energy ranges

Range	τ^a, s
R filter (RTT-150)	58.2 ± 4.5
2–5 keV (RXTE)	51.9 ± 0.3
8–20 keV (RXTE)	35 ± 0.3
Bolometric (RXTE)	43.3 ± 0.3

[a] The e-folding decay time.

we suggest that the optical burst profiles also differ only slightly. Therefore, to measure the timing parameters of the optical bursts, we constructed an average burst profile using the observations on September 7, 8, 10 and October 16, 18, 2003. The individual light curves were brought into coincidence so that the observed maxima of the optical flux occurred at the same time. The accuracy with which the individual light curves were brought into coincidence was limited by the time resolution (8 s). This may be considered sufficient, since the expected post-maximum decay time of the optical flux is approximately an order of magnitude longer.

The derived average optical burst profile is shown in Fig. 3. We used a simple post-maximum exponential decay model to describe it. Because of the limited time resolution (8 s), the exact rise time of the flux to the burst maximum cannot be determined from our observations. The estimated decay time determined from the average optical (R band) burst profile is given in Table 3. For comparison, this table also gives the post-maximum decay times determined from the X-ray burst of September 11, 2003, in various energy ranges and from the X-ray "bolometric" light curve during the burst.

To construct the X-ray bolometric light curve, we took a set of X-ray spectra with an exposure time of 2 s that spanned the entire burst duration. The bolometric light curve was then obtained by fitting each spectrum with a blackbody model (Fig. 4). The observed flux was recalculated to the luminosity by using an upper limit for the distance to the source of 7.5 kpc (see Kong *et al.* 2000).

The burst parameters agrees with those obtained previously (Homer *et al.* 1998; Kong *et al.* 2000).

DISCUSSION

Table 4 gives the burst quasi-period for the burster GS 1826–24 and the persistent X-ray (2.5–25 keV) flux for the period 1997–2003. A gradual increase in the accretion rate onto the neutron star was observed constantly after the discovery of type-I bursts in the binary GS 1826–24; the burst rate of the burster increased with a persistent X-ray flux. Our observations show that this long-term trend is breaking down, with the correlation between the thermonuclear burst rate and the persistent X-ray flux being preserved.

At optical wavelengths, GS 1826–24 has a spectrum with an ultraviolet excess and exhibits He II and Hα emission lines (Motch *et al.* 1994; Barret *et al.* 1995). This is indicative of the strong effect of the irradiation of the outer accretion disk by X-ray emission from the inner regions of the accretion flow. The measured optical colors of the object corrected for interstellar extinction (see, e.g., Barret *et al.* 1995) suggest that the temperature of the optically emitting regions is no lower than 20 000 K. However, the presence of a hot optical companion star with such a temperature in the binary system GS 1826–24 is ruled out for reasons of energetics: the observed optical luminosity is too low for a hot young star. The observed magnitude of GS 1826–24 through the R filter used in the RTT-150 observations is $m_R \approx 18\overset{m}{.}2$. The interstellar extinction toward the object can be determined from the X-ray spectrum of GS 1826–24. RXTE data do not allow this to be done with a reasonable accuracy, because the detector energy range for this observatory begins from ≈ 3 keV. To determine the interstellar extinction, we used the archival ASCA (the operating energy range was 0.5–10 keV) observations of March 31, 1998. Fitting the observed X-ray spectrum of the source with a simple power-law energy dependence of the photon flux corrected for interstellar extinction in neutral matter yields the atomic hydrogen column

density: $N_{\rm H} \approx 6 \times 10^{21}$ atoms cm^{-2}. Using the conversion coefficient from N_H to the R-band extinction (see Bohlin *et al.* 1978; Schlegel *et al.* 1998), we obtain $A_R \approx 2.6$; hence, the magnitude of GS 1826–24 without interstellar extinction is $m_R \approx 15\overset{m}{.}6$. We find the R-band luminosity of the star to be $L_R \approx 1.5 \times 10^{34}$ erg s^{-1} (for an assumed distance to the source of 7.4–7.5 kpc; see Kong *et al.* 2000), a very low value for young stars with a temperature of $\sim 20\,000$ K. At the same time, such a temperature is typical of an irradiated accretion disk (see, e.g., the study of a similar binary system, 4U 1636–536, by Lawrence *et al.* 1983). Thus, it may be assumed that the reradiation of X-ray emission from the inner regions of the accretion flow by the outer regions of an optically thick accretion disk or by the surface of the companion star makes a major contribution to the optical flux from the binary.

Old low-mass late-type (K, M) dwarf stars are typical optical companions of type-I X-ray bursters: for bursts of unsteady thermonuclear burning to occur on the surface of an accreting neutron star, it must have a weak magnetic field and, hence, an old age. Simple estimates indicate that the solid angle subtended by the outer accretion disk in a low-mass X-ray binary is at least several times larger than the solid angle at which the dwarf star is seen from the X-ray source. We assume that the contribution from the companion star of GS 1826–24 to the reradiation of the X-ray flux is small, and that the R-band flux is determined entirely by the luminosity of the irradiated accretion disk.

Unfortunately, we have no simultaneous X-ray and optical observations of GS 1826–24 at our disposal that would allow the response function of an optically thick accretion disk to an X-ray burst to be studied. We can only compare the average optical burst profile with the profile of the X-ray burst observed from the RXTE satellite on September 11, 2003. The optical and X-ray burst profiles are similar and are well described by a post-maximum exponential decay model: $F \propto \exp(-t/\tau)$. The parameter τ (the e-folding decay time) in the R band is approximately equal to τ measured in the energy range 3–5 keV and differs from τ measured in the energy range 8–20 keV (see Table 3). This is probably because the outer accretion disk absorbs and then reprocesses into the optical wavelength range mainly soft X-ray emission at <5 keV. In this case, the fraction of the luminosity at energies >5 keV can be fairly large (e.g., near the maximum of the light curve, νF_ν has a maximum at $\approx$10 keV). The reprocessing efficiency of soft X-ray photons at energies 3–5 keV in the disk is higher than that of harder photons at energies 8–20 keV. Hard X-ray photons are mostly reflected from the disk without being absorbed (the albedo of the accretion disk increases rapidly with energy).

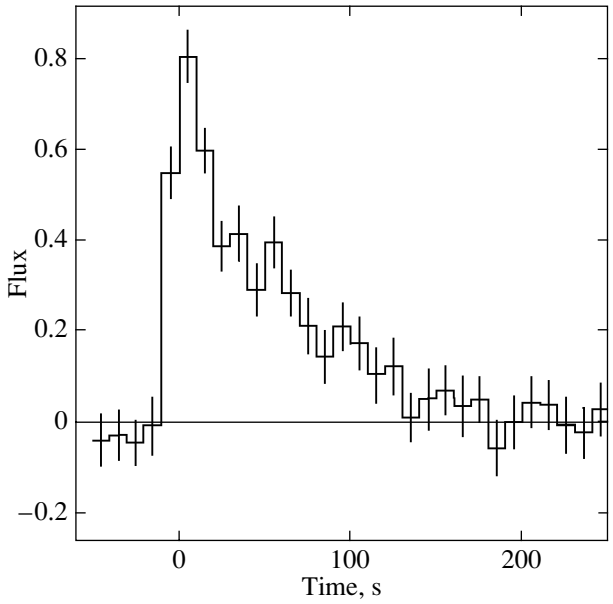

Fig. 3. Average optical (R band, RTT-150) burst profile for GS 1826–24 (as constructed from the observations on September 7, 8, 10 and October 16, 18, 2003).

To constrain the geometry of the accretion disk in the binary GS 1826–24, we used the model of a standard optically thick accretion disk under the following assumptions:

(1) The reprocessing of X rays from the central regions of the disk dominates over the internal energy release in the disk (see, e.g., Lyuty and Sunyaev 1976; Pedersen *et al.* 1982; Lawrence *et al.* 1983). This assumption holds for accretion disks around neutron stars starting from a radius of 10^9 cm (Meyer and Meyer-Hofmeister 1982).

Table 4. Long-term variations in the persistent X-ray flux $F_{\rm pers}$ and in the quasi-period δt of bursts from the burster GS 1826–24 for the period 1997–2003

Date	$F_{\rm pers}$ (2.5–25 keV), 10^{-9} erg s^{-1} cm^{-2}	δt
1997–1998[a]	1.32 ± 0.05	$5.74^{\rm h} \pm 0.13^{\rm h}$
2000[a]	1.8 ± 0.05	4.1 ± 0.08
July 2002[a]	2.19 ± 0.02	3.56 ± 0.03
September 2003[b]	1.75 ± 0.03	3.85 ± 0.1

[a] The data were taken from Galloway *et al.* (2004).

[b] Based on the simultaneous RXTE and RTT-150 observations.

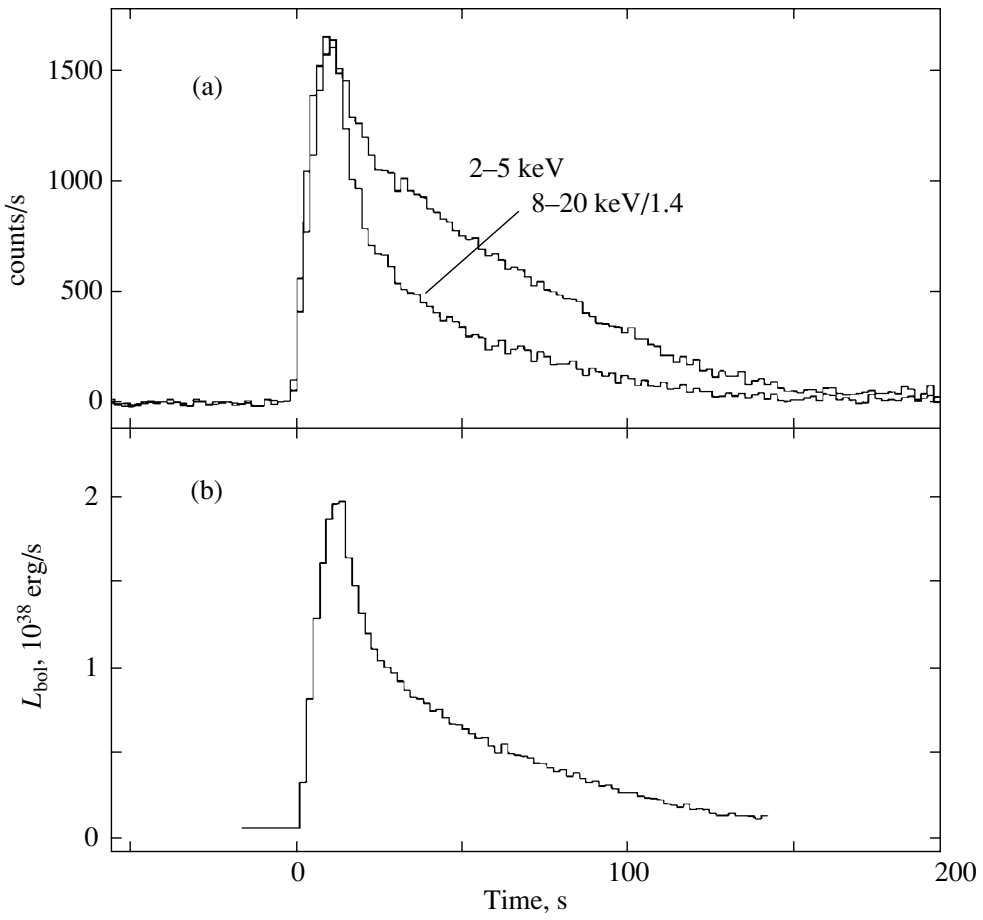

Fig. 4. (a) X-ray burst profiles for GS 1826–24 as constructed from the RXTE observations on September 11, 2003, in various energy ranges and (b) the X-ray bolometric light curve during the burst.

(2) The geometric thickness of the accretion disk depends on its radius as $H(R) \propto R^{9/7}$ (see Vrtilek *et al.* 1990).

(3) The spectrum from each infinitely small region of the disk surface at a given R is described by a blackbody model with temperature T_{eff}. In this case, T_{eff} can be determined from Eq. $2\sigma T_{eff}^4 = \frac{L_d(1-\eta_d)}{4\pi R^2}\cos\chi$, where L_d is the X-ray luminosity of the "central source" (the inner disk regions together with the neutron star), η_d is the albedo of the accretion disk, χ is the angle between the normal to the disk surface at a given point and the central plane of the disk, and σ is the Stefan–Boltzmann constant. To a first approximation, the quantity $L_d(1-\eta_d)$ may be assumed to be equal to the X-ray luminosity at energies 0.5–5 keV, because photons at these energies are reprocessed almost completely into the optical wavelength range (the albedo of the disk is low); for photons at $E > 5$ keV, the albedo of the disk is high, and this spectral range has virtually no effect on the optical flux.

The X-ray (0.5–5 keV) flux during the burst observed from the RXTE satellite rose by a factor of $R_{\rm X} = F_{\rm X,max}/F_{\rm X,min} \approx 12.5$, while the flux in the optical burst rose by a factor of only $R_R = F_{R,\rm max}/F_{R,\rm min} \approx 1.8$. The R-band and X-ray (0.5–5 keV) luminosities of GS 1826–24 in quiescence are $L_R \approx 1.5 \times 10^{34}$ erg s^{-1} and $L_X \approx 4 \times 10^{36}$ erg s^{-1}, respectively (for an assumed distance to the source of 7.5 kpc).

By assuming that the errors in the X-ray and optical luminosities are 10 and 50%, respectively (the large error in the latter case is attributable to the uncertainty in A_R for the large $N_{\rm H}$ needed to calculate L_R), we can bound the region on the disk radius–disk thickness at the outer edge of the plane. The limits obtained are shown in Fig. 5. The shaded region in the figure is the intersection of the regions constructed for the quantities at burst maximum and in quiescence. If the thickness of the disk at

the outer edge is assumed to be $(H/R)_{\rm out} \approx 0.3$–$0.4$ (Meyer and Meyer-Hofmeister 1982), then, as follows from Fig. 5, the outer radius of the accretion disk in GS 1826–24 is $R_{\rm out} \approx 5 \times 10^{10}/(\cos i)^{1/2}$ cm or $\approx 0.7 \times R_\odot/(\cos i)^{1/2}$, where i is the orbital inclination.

This estimate of the outer disk radius is valid only if the outer edge of the disk radiates in the R band. To test this assumption, we estimated the radius $R_{\rm exp}$ starting from which the contribution of the disk to the R band decreases exponentially. The temperature of the disk at this radius will be $T(R_{\rm exp}) \approx hc/(2.7k\lambda_R) \approx 8000$ K. The following effective radii correspond to the temperature $T(R_{\rm exp})$: $R_{\rm exp} \approx 2 \times 10^{11}$ cm and $R_{\rm exp} \approx 9 \times 10^{11}$ cm in quiescence and at burst maximum, respectively. Hence, $R_{\rm exp} > R_{\rm out}$; i.e., it is the outer disk that radiates in the R band.

The observed optical and X-ray fluxes are related by a relation similar to $R_{\rm X} \approx R_R^4$, suggesting that the R band ($\lambda_R = 638$ nm) is close to the Rayleigh–Jeans part of the accretion-disk spectrum. Indeed, the R band lies in the Rayleigh–Jeans part of the spectrum if the outer accretion disk has a temperature $T > hc/(k\lambda_R) \approx 22000$ K or, equivalently, the outer disk radius must be $< 2 \times 10^{10}$ cm (in quiescence) or $< 8 \times 10^{10}$ cm (at burst maximum) for a given shape of the accretion disk and a given X-ray luminosity. Our estimate of the outer disk radius is close to these values.

It is also interesting to compare the estimated $R_{\rm out}$ with the delay $c\Delta t$ determined from simultaneous X-ray and optical observations (Kong *et al.* 2000). A comparison of the X-ray (2–6.4 keV) and optical (without a filter) light curves during a burst from the burster made it possible to determine the delay between the X-ray and optical fluxes, $\Delta t = 2.8 \pm 0.7$ s. This value roughly corresponds to the time it takes for light to traverse the accretion disk that we estimated. Moreover, if we calculate the size of the accretion disk from the measured delay, $R_{\rm out} \approx c\Delta t \approx 8.4 \times 10^{10}$ cm, then we can roughly estimate the binary inclination: $i \sim 40^\circ$–70°. However, we should take into account the fact that the above estimate of the binary inclination is very rough and does not include particular features of the disk response to an X-ray burst. More detailed studies and higher-quality simultaneous X-ray and optical observations of bursts from the burster are required to clarify this question.

The size of the accretion disk allows us to estimate the radius of the Roche lobe R_L for the compact component in the binary (assuming that $R_{\rm out}/R_L \approx 0.5$–$0.8$; see de Jong 1996): $R_L \approx (4$–$7) \times 10^{10}$ cm. Assuming that the companion of GS 1826–24 is a low-mass ($M_2 \approx 0.1$–$1.0 M_\odot$) star, we can estimate the range of possible orbital periods of the binary:

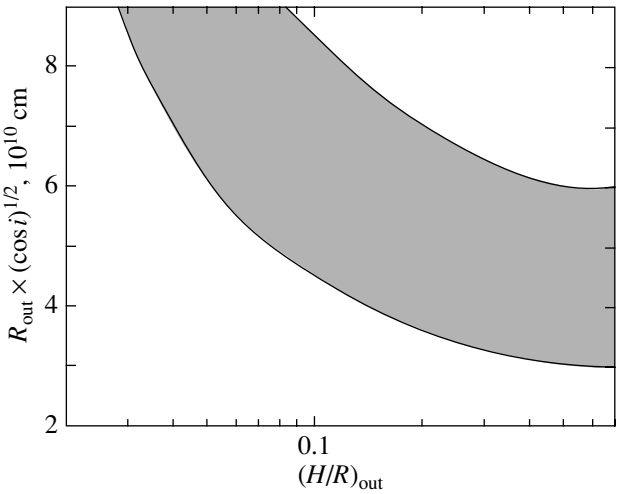

Fig. 5. Observational bounds on the parameters $R_{\rm out}$ and $(H/R)_{\rm out}$.

$P_{\rm orb} \approx 2$–7 h (see also Homer *et al.* (1998) for estimates). Evidence suggests that the orbital period of GS 1826–24 could be equal to ≈ 2.1 h (Homer *et al.* 1998). However, the statistics of the observations used are poor, and this period should be confirmed.

ACKNOWLEDGMENTS

This work was supported by the Ministry of Industry and Science (Presidential grant no. NSh-2083.2003.2), the Nonstationary Phenomena in Astronomy Program, and the Astronomy Federal Science and Technology Program (project no. 40.022.1.1.1102). M.G. Revnivtsev, R.A. Burenin, M.R. Gilfanov, N.N. Pavlinsky, and E. Gogush thank the ISSI (International Space Science Institute) for their support of this work, part of which was done during a visit to the ISSI.

REFERENCES

1. V. Arefyev and M. Gilfanov, submitted to Astrophys. J. (2004).
2. D. Barret, C. Motch, and W. Pietsch, Astron. Astrophys. **296**, 459 (1995).
3. R. C. Bohlin, B. D. Savage, and J. F. Drake, Astrophys. J. **224**, 132 (1978).
4. R. Cornelisse, J. J. M. in't Zand, F. Verbunt, *et al.*, Astron. Astrophys. **405**, 1033 (2003).
5. A. Cumming, astro-ph/0309626 (2003).
6. J. A. de Jong, J. van Paradijs, and T. Augusteijn, Astron. Astrophys. **314**, 484 (1996).
7. D. K. Galloway, A. Cumming, E. Kuulkers, *et al.*, Astrophys. J. **601**, 466 (2004).
8. L. Homer, P. A. Charles, and D. O'Donoghue, Mon. Not. R. Astron. Soc. **298**, 497 (1998).

9. A. K. H. Kong, L. Homer, E. Kuulkers, *et al.*, Mon. Not. R. Astron. Soc. **311**, 405 (2000).
10. A. Lawrence, L. Cominsky, C. Engelke, *et al.*, Astrophys. J. **271**, 793 (1983).
11. F. Makino *et al.* (The Ginga Team), IAU Circ., No. 4653 (1989).
12. F. Meyer and E. Meyer-Hofmeister, Astron. Astrophys. **106**, 34 (1982).
13. C. Motch, D. Barret, W. Pietsch, *et al.*, IAU Circ., No. 6101 (1994).
14. H. Pedersen, J. Lub, H. Inoue, *et al.*, Astrophys. J. **263**, 325 (1982).
15. D. J. Schlegel, D. P. Finkbeiner, and M. Davis, Astrophys. J. **500**, 525 (1998).
16. P. Ubertini, A. Bazzano, M. Cocchi, *et al.*, IAU Circ., No. 6611 (1997).
17. P. Ubertini, A. Bazzano, M. Cocchi, *et al.*, Astrophys. J. Lett. **514**, L27 (1999).
18. S. D. Vrtilek, J. C. Raymond, M. R. Garcia, *et al.*, Astron. Astrophys. **235**, 162 (1990).

Translated by V. Astakhov

Astronomy Letters, Vol. 30, No. 11, 2004, pp. 759–771. Translated from Pis'ma v Astronomicheskiĭ Zhurnal, Vol. 30, No. 11, 2004, pp. 835–847.

Symmetry of the Neutron and Proton Superfluidity Effects in Cooling Neutron Stars

M. E. Gusakov[1], A. D. Kaminker[1*], D. G. Yakovlev[1], and O. Yu. Gnedin[2]

[1] *Ioffe Physicotechnical Institute, Russian Academy of Sciences, ul. Politekhnicheskaya 26, St. Petersburg, 194021 Russia*

[2] *Space Telescope Science Institute, 3700 San Martin Drive, Baltimore, MD 21218, USA*

Received April 2, 2004

Abstract—We investigate the combined effect of neutron and proton superfluidities on the cooling of neutron stars whose cores consist of nucleons and electrons. We consider the singlet state paring of protons and the triplet pairing of neutrons in the cores of neutron stars. The critical superfluid temperatures T_c are assumed to depend on the matter density. We study two types of neutron pairing with different components of the total angular momentum of a Cooper pair along the quantization axis ($|m_J| = 0$ or 2). Our calculations are compared with the observations of thermal emission from isolated neutron stars. We show that the observations can be interpreted by using two classes of superfluidity models: (1) strong proton superfluidity with a maximum critical temperature in the stellar core $T_c^{\max} \gtrsim 4 \times 10^9$ K and weak neutron superfluidity of any type ($T_c^{\max} \lesssim 2 \times 10^8$ K); (2) strong neutron superfluidity (pairing with $m_J = 0$) and weak proton superfluidity. The two types of models reflect an approximate symmetry with respect to an interchange of the critical neutron and proton pairing temperatures. © *2004 MAIK "Nauka/Interperiodica".*

Key words: *neutron stars, nucleon superfluidity, thermal emission.*

INTRODUCTION

At present, the properties of superdense matter in the cores of neutron stars are known poorly. For example, the fundamental problem of the equation of state for supernuclear-density matter has not yet been solved. The existing calculations are model dependent and yield a wide variety of equations of state for matter in the cores of neutron stars (Lattimer and Prakash 2001; Haensel 2003) with different compositions of this matter (nucleons, hyperons, pion or kaon condensates, quarks). The properties of nucleon superfluidity in the inner layers of neutron stars are also unclear. The calculated critical nucleon superfluidity temperatures strongly depend on the nucleon–nucleon interaction model used and on the method of allowance for many-body effects (see, e.g., Lombardo and Schulze 2001). In particular, they can be studied by comparing the star cooling theory with the observations of thermal emission from isolated neutron stars.

Here, we continue to simulate the cooling of superfluid neutron stars whose cores contain neutrons, protons, and electrons and whose critical nucleon superfluidity temperatures depend on the matter density. We extend the class of cooling models that were proposed by Kaminker *et al.* (2001, 2002) and Yakovlev *et al.* (2001a, 2002) to interpret the observations of thermal emission from isolated neutron stars. These authors paid particular attention to the case of strong proton superfluidity and weak neutron superfluidity in the stellar core. Since the superfluidity models have a large uncertainty, we consider a broader class of models without assuming from the outset that the proton pairing is stronger than the neutron pairing. In addition, attention is given to the nonstandard neutron triplet pairing model with an anisotropic gap that vanishes along the quantization axis.

OBSERVATIONAL DATA

The observational data on thermal emission from eleven isolated middle-aged ($10^3 \lesssim t \lesssim 10^6$ yr) neutron stars are collected in the table. In what follows, T_s^∞ is the stellar surface temperature recorded by a distant observer, and t is the age of the star. The data differ from those presented previously (see, e.g., Yakovlev *et al.* 2002), because they include the results of new observations.

Two young objects, RX J0822–4300 and 1E 1207.4–5209 (=J1210–5226), are radio-quiet neutron stars in supernova remnants. Two of the

*E-mail: kam@astro.ioffe.ru

Surface temperatures of isolated neutron stars

Source	t, 10^3 yr	T_s^∞, 10^6 K	Model[a]	Confidence, %	References
PSR J0205+6449	0.82	<1.1	bb	–	Slane *et al.* (2002)
Crab	1	<2.0	bb	99.7	Weisskopf *et al.* (2004)
RX J0822–4300	2–5	1.6–1.9	H	90	Zavlin *et al.* (1999)
1E 1207.4–5209	3–20	1.4–1.9	H	90	Zavlin *et al.* (2004)
Vela	11–25	0.65–0.71	H	68	Pavlov *et al.* (2001)
PSR B1706–44	~ 17	$0.82^{+0.01}_{-0.34}$	H	68	McGowan *et al.* (2004)
PSR J0538+2817	30 ± 4	~ 0.87	H	–	Zavlin and Pavlov (2003)
Geminga	~ 340	~ 0.5	bb	90	Zavlin and Pavlov (2003)
RX J1856.4–3754	~ 500	<0.65	–	–	see text
PSR B1055–52	~ 540	~ 0.75	bb	–	Pavlov and Zavlin (2003)
RX J0720.4–3125	~ 1300	~ 0.51	H	–	Motch *et al.* (2003)

[a] The observations were interpreted in terms of either a hydrogen atmosphere model (H) or a blackbody model (bb).

three oldest objects ($t \geqslant 5 \times 10^5$ yr), RX J1856.4–3754 and RX J0720.4–3125, are also radio-quiet neutron stars. The remaining seven sources—PSR J0205+6449, the Crab pulsar (PSR B0531+21), the Vela pulsar (PSR B0833–45), PSR B1706–44, PSR J0538+2817, Geminga (PSR B0633+1746), and PSR B1055–52—are observed as radio pulsars. PSR J0205+6449 and the Crab pulsar are located in the remnants of historical supernovae; their ages are known exactly. The age of RX J0822–4300 was determined from the age of the remnant of the parent supernova Puppis A and lies within the range $t = (2–5) \times 10^3$ yr (see, e.g., Arendt *et al.* 1991), with the most probable value being $t = 3.7 \times 10^3$ yr (Winkler *et al.* 1988). The age of 1E 1207.4–5209 is assumed to be equal to the age of the remnant of the parent supernova G296.5+10. According to Roger *et al.* (1988), this age lies within the range $\sim 3 \times 10^3$ to $\sim 20 \times 10^3$ yr. The age of the Vela pulsar is assumed to lie within the range from the standard characteristic pulsar age of 1.1×10^4 yr to the age of 2.5×10^4 yr obtained by Lyne *et al.* (1996) by analyzing the pulsar spindown with allowance made for the observed glitches. Kramer *et al.* (2003) estimated the age of PSR J0538+2817, $t = (30 \pm 4) \times 10^3$ yr, from the measured proper motion of the neutron star relative to the center of the remnant of the parent supernova S147. The age of RX J1856.4–3754 was estimated by Walter (2001) from kinematic considerations and revised by Walter and Lattimer (2002). Following the latter authors, we take a mean value of $t = 5 \times 10^5$ yr and choose an error range for t that excludes the value of $t = 9 \times 10^5$ yr obtained by Walter (2001). Zane *et al.* (2002) and Kaplan *et al.* (2002) estimated the characteristic age of RX J0720.4–3125 from the X-ray measurements of the spindown rate of the star $\dot{P}$. We take a mean value of 1.3×10^6 yr with an uncertainty factor of 2. The ages of the three radio pulsars PSR B1706–44, Geminga, and PSR B1055–52 are set equal to the characteristic age with the same uncertainty factor of 2.

For the two youngest objects (the Crab pulsar and PSR J0205+6449), only upper limits were placed on T_s^∞ (Weisskopf *et al.* 2004; Slane *et al.* 2002). The surface temperatures of five sources—RX J0822–4300, 1E 1207.4–5209, Vela, PSR B1706–44, and PSR J0538+2817—were determined by using neutron-star hydrogen atmosphere models (for references, see the table). These models yield more realistic neutron-star radii and hydrogen column densities (see, e.g., Pavlov *et al.* 2002) than the blackbody model.

The pulsar PSR B0656+14 that was considered previously (see, e.g., Yakovlev *et al.* 2002) was excluded from the table. A simultaneous analysis of new X-ray and optical observations of the source

(given the distance to it improved using the parallax measurements by Brisken *et al.* (2003)) leads either to an overly small neutron-star radius (in the blackbody model) or to an overly small distance to the star (in the hydrogen atmosphere model) (Zavlin and Pavlov 2003). This makes the interpretation of the stellar thermal emission too unreliable.

For Geminga and PSR B1055−52, the blackbody model is more self-consistent. Therefore, we take the values of T_s^∞ obtained by interpreting the observed spectra in terms of this model. For PSR B1055−52, we take T_s^∞ from Pavlov and Zavlin (2003).

The surface temperature of RX J1856.4−3754 has not been determined accurately enough. The wide spread in T_s^∞ obtained for different radiation models (see, e.g., Pons *et al.* 2002; Braje and Romani 2002; Burwitz *et al.* 2003; Pavlov and Zavlin 2003; Trümper *et al.* 2003) stems from the fact that the optical and X-ray observations cannot be described by a single blackbody model. This may be attributable, for example, to the presence of hot spots on the stellar surface. Therefore, we fix only the upper limit of $T_s^\infty < 6.5 \times 10^5$ K that agrees with the value of T_s^∞ obtained both in the model of a Si-ash atmosphere (Pons *et al.* 2002) and in the model of condensed matter on the stellar surface (Burwitz *et al.* 2003). This limit is also consistent with the model of a nonuniform stellar surface temperature distribution proposed by Pavlov and Zavlin (2003). For the latter model, the mean stellar surface temperature is $T_s^\infty = 5 \times 10^5$ K and lies below the chosen upper limit.

Finally, we took the surface temperature of RX J0720.4−3125 from the paper by Motch *et al.* (2003). These authors interpreted the observed spectrum by using a finite-depth hydrogen atmosphere model.

For PSR J0538−2817, PSR B1055−52, and RX J0720.4−3125, the errors in T_s^∞ were not given by the authors (see the table). In all these case, we assume them to be equal to 20%.

NUCLEON SUPERFLUIDITY MODELS AND NEUTRINO EMISSION DUE TO COOPER PROTON PAIRING

The neutron or proton superfluidity can be described by the density profile of the critical temperature, $T_c(\rho)$. Microscopic theories predict (see, e.g., Lombardo and Schulze 2001; for references, see also the review by Yakovlev *et al.* 1999a) the existence of singlet ($^1S_0$) neutron pairing ($T_{cn} = T_{cns}$) in the inner crust and the outermost layers of the stellar core and singlet proton pairing (T_{cp}) and triplet ($^3P_2$) neutron pairing ($T_{cn} = T_{cnt}$) in the stellar core. The possibility of different angular momentum components m_J for a neutron–neutron pair along the quantization axis ($|m_J| = 0, 1, 2$) should be taken into account when triplet pairing is considered. A superposition of states with different m_J can also be an energetically favored state of the Cooper pair (see, e.g., Amundsen and Østgaard 1985; Baldo *et al.* 1992; Khodel *et al.* 1998, 2001). Only one type of triplet superfluidity with $m_J = 0$ has commonly been assumed in neutron-star cooling calculations. The papers by Schaab *et al.* (1998) and Gusakov and Gnedin (2002) constitute an exception. Below, we consider the neutron triplet pairing with $|m_J| = 0$ and 2, because the effects of these two types of superfluidity on the heat capacity and the neutrino luminosity of neutron stars are qualitatively different. Following Yakovlev *et al.* (1999a), we denote the three types of superfluidity ($^1S_0$, $^3P_2(m_J = 0)$, and $^3P_2(|m_J| = 2)$) considered here by the letters A, B, and C, respectively. The energy gap in the neutron energy spectrum, $\varepsilon(\mathbf{p})$, is isotropic in case A and anisotropic in cases B and C; i.e., it depends on the angle between the direction of the particle momentum $\mathbf{p}$ and the quantization (z) axis. In case C, the energy gap vanishes if $\mathbf{p}$ is directed along the z axis.

Nucleon superfluidity suppresses the neutrino processes involving nucleons, changes the nucleon heat capacity, and triggers an additional neutrino emission mechanism related to the Cooper nucleon pairing (Flowers *et al.* 1976). In this case, the effect of type-C neutron superfluidity on the heat capacity of the matter and the neutrino reactions differs qualitatively from the effect of type-A or -B superfluidity. Thus, for example, the suppression of the neutrino processes and the heat capacity by type-C superfluidity and type-B or -A superfluidity has power-law and exponential dependences, respectively (see, e.g., Yakovlev *et al.* 1999a).

Microscopic theories yield a wide variety of $T_c(\rho)$ profiles (see, e.g., Lombardo and Schulze 2001). The $T_c(\rho)$ maxima can take on values from $\lesssim 10^8$ to 5×10^{10} K. The $T_{cnt}(\rho)$ maxima in many models are lower than the $T_{cp}(\rho)$ and $T_{cns}(\rho)$ maxima, because the attraction between triplet-state nucleons is weaker.

We use four phenomenological model superfluidity profiles $T_c(\rho)$ (for both neutrons and protons) in the core of a neutron star. In Fig. 1, these models are denoted by *a*, *b*, *c*, and *d*. The chosen $T_c(\rho)$ profiles are similar and differ only in height (maximum value): $T_c^{max} = 10^{10}$, 4.0×10^9, 8.0×10^8, and 8.0×10^7 K (models *a*, *b*, *c*, and *d*). Superfluidities *a*, *b*, *c*, and *d* will be called *strong*, *moderately strong*, *moderate*, and *weak*, respectively. The chosen models are consistent with the theoretical calculations of $T_c(\rho)$. The $T_c(\rho)$ curves have steep slopes at $\rho > \rho_D$, where ρ_D is

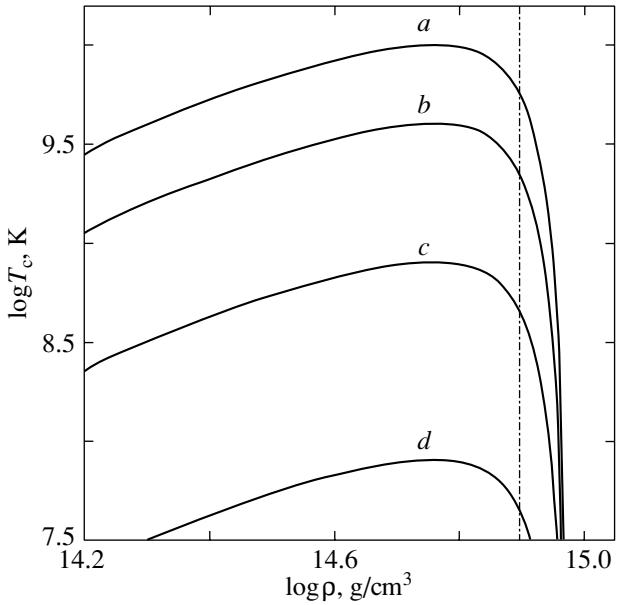

Fig. 1. Model density (ρ) profiles of the critical neutron and/or proton temperatures in the core of a neutron star. The vertical dot-dashed line indicates the threshold density of the direct URCA process.

the threshold density at which the direct URCA process opens (see below).

Below, we denote the combined nucleon superfluidity by $\alpha\beta$, where α is one of the neutron triplet (type B or C) superfluidity models (a, b, c, or d), and β is one of the proton singlet superfluidity models (a, b, c, or d).

Note that there is a large uncertainty in the rate of neutrino energy release Q_p due to Cooper proton pairing. In the nonrelativistic approximation (Yakovlev *et al.* 1999b), $Q_p \propto \zeta_p$, where $\zeta_p = c_{\rm Vp}^2$, and $c_{\rm Vp} \approx 0.08$ is the vector constant of the neutral proton current; the latter is numerically small and leads to very low values of Q_p. For comparison, the rate of neutrino energy release Q_n due to Cooper neutron triplet pairing is proportional to $\zeta_n = c_{\rm Vn}^2 + 2c_{\rm An}^2 = 4.17$, where $c_{\rm Vn} = 1$ and $c_{\rm An} = -1.26$ are the vector and axial vector constants of the neutral neutron current, respectively. According to Kaminker *et al.* (1999), applying the relativistic correction that contains the axial vector constant of the neutral proton current $c_{\rm Ap} = 1.26$ can greatly (by a factor of 10 to 50) increase the rate constant ζ_p (and the rate of energy release Q_p) compared to the nonrelativistic value of $\zeta_p = c_{\rm Vp}^2 = 0.0064$.

We used this value of ζ_p enhanced by relativistic effects in our previous neutron-star cooling calculations. At the same time, studying the cooling of stars with density-dependent critical proton temperatures $T_{\rm cp}(\rho)$ (see, e.g., Kaminker *et al.* 2002), we considered only the models of strong proton superfluidity (similar to model a). Such superfluidity arises at early cooling stages. The neutrino emission due to Cooper proton pairing at these stages cannot compete with other neutrino processes and plays no special role. In a cooler star, this neutrino emission is generated only in small volume and weakly affects the cooling of the star. Thus, in the cooling scenarios with strong proton superfluidity considered previously, the emission due to Cooper proton pairing (and the exact value of ζ_p) was unimportant.

In this paper, we also consider the models of moderate proton superfluidity in which the emission due to Cooper proton pairing can appreciably affect the star cooling and the value of the rate constant ζ_p is important. As was noted, for example, by Yakovlev *et al.* (1999b) and Kaminker *et al.* (1999), the rate constant ζ_p can be determined not only by relativistic effects, but also by the renormalization effects of the medium (many-body effects in nucleon matter). This renormalization for the process in question has not been made. Carter and Prakash (2002) gave an example of a similar renormalization of the constant of the axial vector current. For the sake of definiteness, we perform calculations by choosing the renormalized value of $\zeta_p = 1$. The sensitivity of our calculations to ζ_p is described below (see also Fig. 7).

THE COOLING OF STARS WITH STRONG PROTON SUPERFLUIDITY

Let us compare the observational data with our calculations of the cooling curves ($T_{\rm s}^{\infty}(t)$ profiles) for neutron stars. The calculations were performed using a code described by Gnedin *et al.* (2001). As in previous papers (mentioned in the Introduction), we consider the models of neutron stars whose cores are composed of neutrons n, protons p, and electrons e. We use a moderately stiff equation of state for matter in the stellar core proposed by Prakash *et al.* (1988) (model I with the compression modulus of symmetric nucleon matter at saturation $K = 240$ MeV). The maximum mass of a stable neutron star for the chosen equation of state is $M = 1.977 M_\odot$ (at a radius of $R = 10.754$ km and a central density of $\rho_{\rm c} = 2.575 \times 10^{15}$ g cm^{-3}). This equation of state permits an intense direct URCA process of neutrino generation (Lattimer *et al.* 1991) at densities ρ above the threshold density $\rho_{\rm D} = 7.851 \times 10^{14}$ g cm^{-3}, i.e., in stars with masses $M > M_{\rm D} = 1.358 M_\odot$. The radius of a star with the threshold mass $M_{\rm D}$ is $R = 12.98$ km.

The thermal evolution of a neutron star consists of three stages:

(1) The stage of *thermal relaxation* of the inner stellar layers ($t \lesssim 100$ yr);

(2) The subsequent stage of *neutrino cooling* ($10^2 \lesssim t \lesssim 10^5$ yr) of a star with an isothermal core via neutrino emission from inside the star;

(3) The final stage of *photon cooling* ($t \gtrsim 10^5$ yr) via photon emission from the stellar surface.

The cooling theory for nonsuperfluid stars cannot explain the entire set of observational data (see, e.g., Kaminker *et al.* 2002). However, this theory can be reconciled with the observations by taking into account the possible nucleon superfluidity. According to Kaminker *et al.* (2001), it will suffice to assume the existence of strong proton superfluidity and weak neutron superfluidity in the stellar cores.

Figure 2 shows the cooling curves for neutron stars of different masses with weak neutron superfluidity d and strong proton superfluidity a. Such weak neutron superfluidity switches on only at the photon cooling stage. Therefore, the type of weak neutron superfluidity (B or C) does not affect the cooling of middle-aged stars. The cooling curves for stars with masses $M \gtrsim M_\odot$ fill the hatched region. All of the observed sources fall within this region; i.e., they can be interpreted in terms of the proposed superfluidity model.

As Kaminker *et al.* (2002) showed, strong proton superfluidity with weak neutron superfluidity (or with normal neutrons) gives rise to three types of cooling neutron stars.

Low-mass stars cool down *very slowly* (more slowly than low-mass nonsuperfluid stars). The cooling curves for such stars depend weakly on their mass, the equation of state in their cores, and the proton superfluidity model (on the specific form of the $T_{\rm cp}(\rho)$ profile provided that the superfluidity in the stellar core is strong enough, $T_{\rm cp}(\rho) \gtrsim 4 \times 10^9$ K). The upper boundary of the hatched region in Fig. 2 is the cooling curve for a star with a mass of $M = 1.35 M_\odot$; it is almost indistinguishable from the cooling curve for a star with a mass of $M = 1.1 M_\odot$ and agrees with the observations of four sources, RX J0822−4300, 1E 1207.4−5209, PSR B1055−52, and RX J0720.4−3125, the hottest ones for their ages. These sources will be considered as low-mass neutron stars.

High-mass neutron stars cool down *very rapidly* via intense neutrino emission generated by the direct URCA process in the inner stellar core. At high matter densities ($\rho \gtrsim 10^{15}$ g cm^{-3}), the proton superfluidity weakens (Fig. 1) and ceases to suppress the neutrino emission. The cooling curves for such stars depend weakly on their mass, the equation of state, and the proton superfluidity model. They almost coincide with the cooling curves for high-mass nonsuperfluid stars. All of the observed isolated neutron stars are much hotter than the stars of this type.

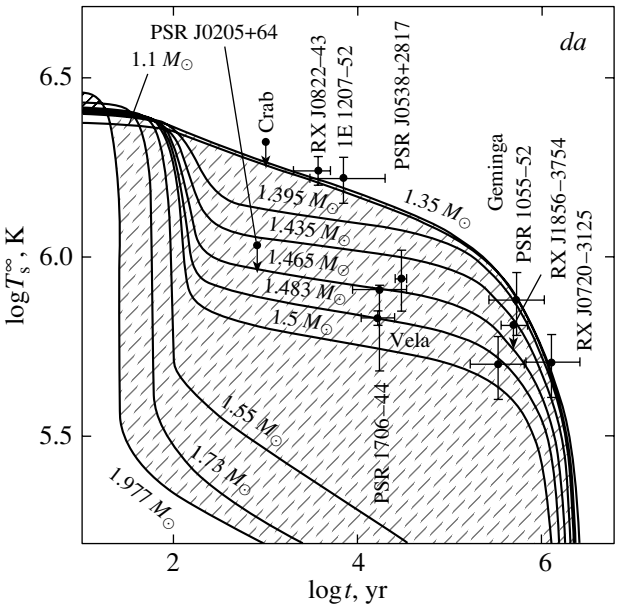

Fig. 2. Comparison of the observations (see the table) with the cooling curves for neutron stars with masses from 1.1 to 1.977 $M_\odot$ (indicated near the curves) for weak neutron superfluidity d and strong proton superfluidity a. The region filled with the cooling curves for stars of different masses is hatched.

Finally, *medium-mass* stars cool down *moderately rapidly*. Their cooling depends strongly on the mass, the equation of state, and the proton superfluidity model. By varying the stellar mass, we can obtain a family of cooling curves that fill the space between the cooling curves for low-mass and high-mass stars. We consider the sources PSR J0205+6449, Vela, PSR B1706−44, PSR J05538+2817, Geminga, and RX J1856.4−3754 as medium-mass stars.

THE COOLING OF NEUTRON STARS WITH COMBINED NUCLEON SUPERFLUIDITY

Figures 3–6 show the cooling curves for neutron stars with different superfluidities of neutrons α and protons β ($\alpha, \beta = a, b, c$, or d). The neutron superfluidity is of type B. We considered all the possible combinations of neutron and proton superfluidities. The upper cooling curve for a low-mass star ($M = 1.1 M_\odot$, with a central density of $\rho_{\rm c} = 6.23 \times 10^{14}$ g cm^{-3}) and the lower cooling curve for a high-mass star ($M = M_{\rm max}$) are shown for each combination $\alpha\beta$. The lower curve is virtually independent of the models of superfluidity $\alpha\beta$ (see the previous section). The region between the upper and lower cooling curves (similar to the hatched region in Fig. 2) can

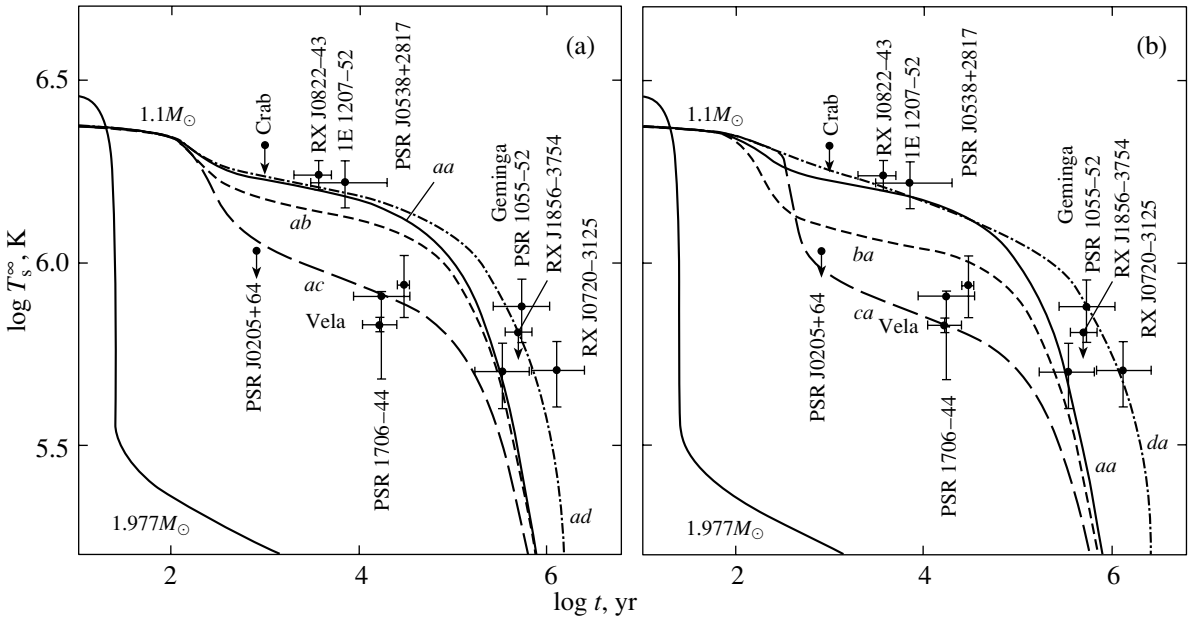

Fig. 3. (a) Cooling curves for stars of two masses, $M = 1.977M_\odot$ and $M = 1.1M_\odot$, with neutron superfluidity a and for different proton superfluidity models (a, b, c, or d); (b) the same for the proton superfluidity model a and different neutron superfluidity models (a, b, c, or d). Type-B neutron superfluidity was chosen for all cases. The theoretical curves are compared with the observations. The cooling of a star with $M = 1.977M_\odot$ does not depend on the superfluidity model.

be filled with the cooling curves of intermediate-mass stars and is admissible for the model of superfluidity $\alpha\beta$ under consideration. As in Fig. 2, the observational data are shown. The nucleon superfluidity models can be constrained by comparing the admissible T_s^∞ regions with the observational data.

Each of Figs. 3–6 consists of two panels: in panel (a), the neutron superfluidity α is fixed, and the cooling curves are given for all four proton superfluidity models; in panel (b), the proton superfluidity β is fixed, and the cooling curves are given for all four neutron superfluidity models. By comparing panels (a) and (b), we can trace the change in cooling when the proton superfluidity is replaced with the neutron superfluidity (and vice versa).

Fixed Proton Superfluidity

Let us choose a proton superfluidity model ($\beta = a, b, c,$ or d) and consider the dependence of the upper cooling curves on the models of neutron superfluidity α in Figs. 3–6.

The $b\beta$ cooling curves run below the $a\beta$ curves because of the neutrino emission due to Cooper neutron pairing. This emission is significantly suppressed in the models with strong neutron superfluidity a (see, e.g., Yakovlev *et al.* 1999a, 1999b, 2001b). All of the remaining neutrino reactions involving neutrons and the neutron heat capacity are completely suppressed by neutron superfluidity a or b. The difference between the $a\beta$ and $b\beta$ cooling curves depends on the model of proton superfluidity β. Thus, for example, as we go from model $\beta = a$ to $\beta = b$ and then to the model of moderate proton superfluidity $\beta = c$, the contribution of the neutrino energy release due to Cooper proton pairing to the neutrino luminosity of the star increases (and becomes dominant for $\beta = c$). Indeed, the neutrino emission due to Cooper pairing affects most strongly the cooling at moderate critical nucleon temperatures, $T_c \sim 2 \times (10^8$–$10^9)$ K (see, e.g., Yakovlev *et al.* 1999b, 2001b). As a result, the difference between the $a\beta$ and $b\beta$ cooling curves in Figs. 3–5 steadily decreases as we go from the model $\beta = a$ to $\beta = b$ and $\beta = c$. At the same time, the admissible theoretical cooling regions agree with the observations increasingly poorly.

For weak superfluidity $\beta = d$ (Fig. 6), the protons remain normal for $t \lesssim 10^5$ yr, until the onset of the photon cooling stage. In this case, the main neutrino process with proton involvement is bremsstrahlung during proton–proton collisions. Since the contribution of this process to the neutrino emission is much smaller than the contribution of the Cooper proton pairing in model c, the difference between the ad and bd curves again increases. As in Fig. 3 (the aa and ba curves), it is determined mainly by the more intense neutrino generation due to Cooper neutron pairing in model b than in model a. As a result, the admissible region of stellar surface temperatures for combined

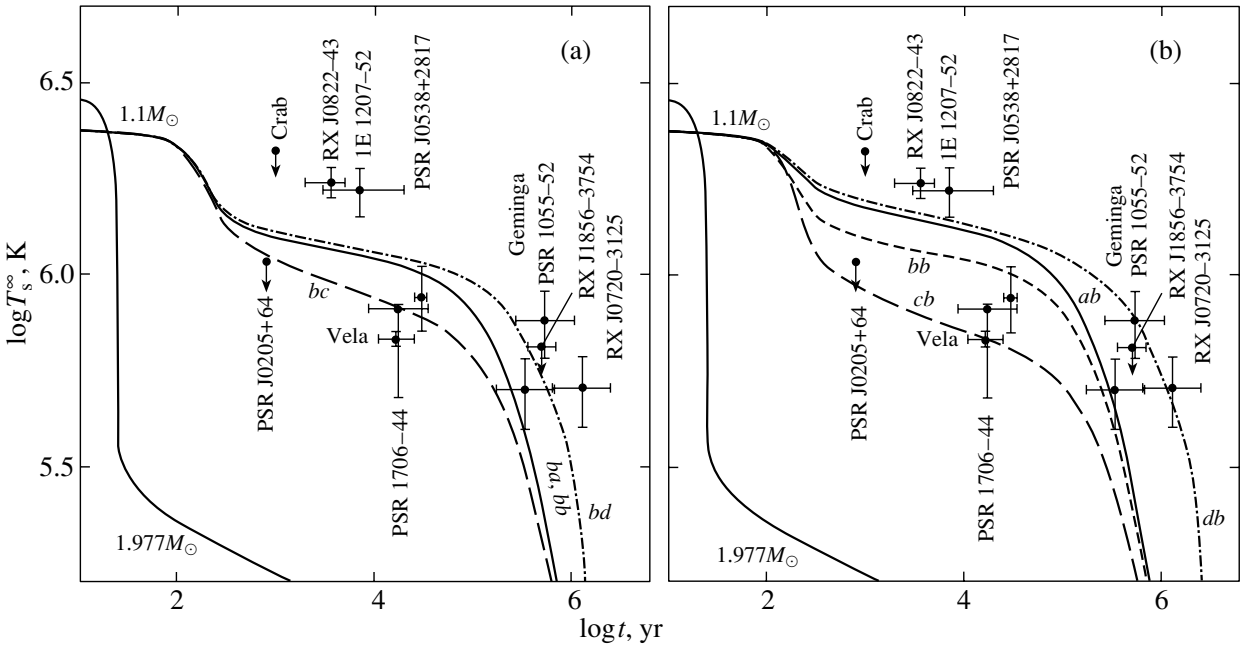

Fig. 4. Same as Fig. 3 for the fixed neutron (a) or proton (b) superfluidity model *b*.

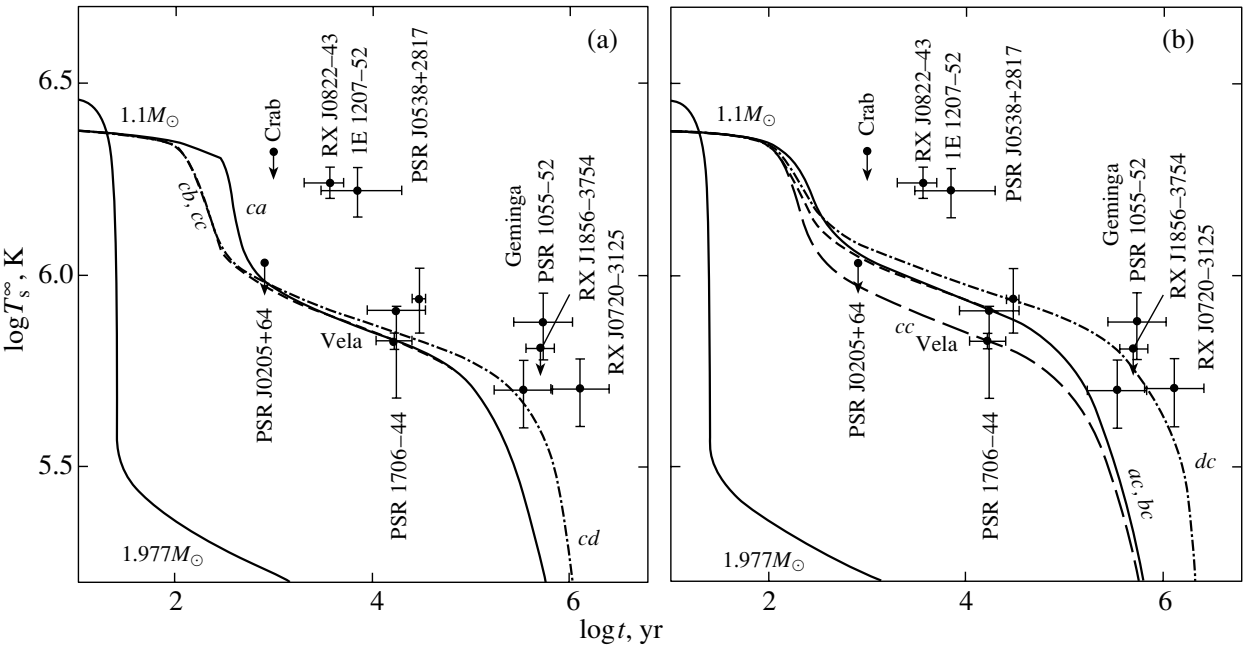

Fig. 5. Same as Fig. 3 for the neutron (a) or proton (b) superfluidity model *c*.

superfluidity *ad* (as in the case of superfluidity *da*, cf. Fig. 6 with Figs. 2 and 3) agrees with the observations.

The $a\beta$ and $b\beta$ curves approach each other at the photon cooling stage ($t \gtrsim 10^5$ yr). In this case, the influence of neutron *a* or *b* superfluidity on the cooling of the star manifests itself mainly in strong suppression of the neutron heat capacity. As a result, the heat capacity of the star is determined by the total heat capacity of the protons (also suppressed by the superfluidity β) and electrons.

For the $c\beta$ superfluidity models, the neutrino emission due to Cooper neutron pairing is particularly effective. As a result, the $c\beta$ cooling curves in Figs. 3–6 run well below the $a\beta$ and $b\beta$ curves and do not differ too much from one another. In particular, all of

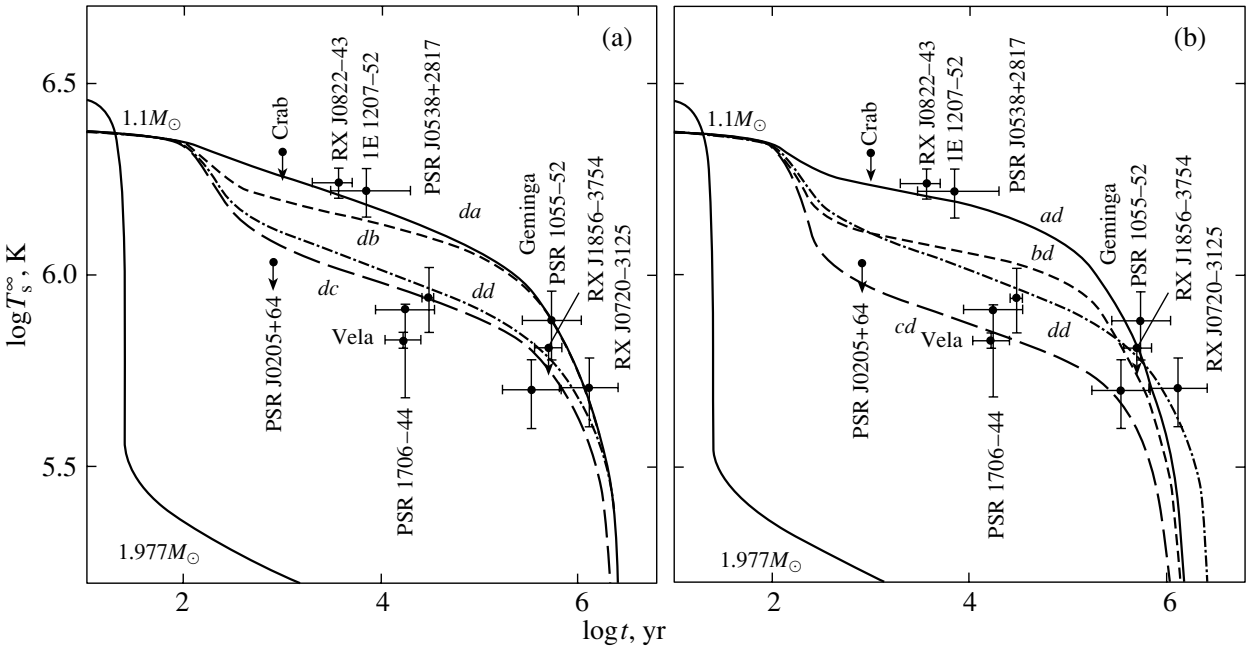

Fig. 6. Same as Fig. 3 for the neutron (a) or proton (b) superfluidity model *d*.

the $c\beta$ curves describe the sharp speedup in cooling at $t \sim 300$ yr attributable to the switch-on of neutrino emission due to neutron pairing. We can see that the admissible stellar surface temperatures obtained for the $c\beta$ superfluidity models lie well below most of the observational data points.

For the model of weak neutron superfluidity *d*, the $d\beta$ curves almost coincide with the cooling curves for normal neutrons. Differences arise only at the photon cooling stage ($t \gtrsim 10^5$ yr) from the partial suppression of the neutron heat capacity. However, at the neutrino cooling stage, the *d*-type neutron superfluidity has not yet set in. Therefore, all of the $d\beta$ cooling curves lie above the $c\beta$ curves. At $t \gtrsim 10^5$–10^6 yr, the $d\beta$ cooling curves for any β run above both the $a\beta$ and $b\beta$ curves due to the strong suppression of the neutron heat capacity by the superfluidities *a* and *b*. Finally, the cooling curve for the model of combined superfluidity *dd* is close to the standard cooling curve for nonsuperfluid low-mass ($M < M_{\rm D}$) neutron stars. This cooling curve disagrees with the observations of many neutron stars (both the hottest and coolest for their ages).

Fixed Neutron Superfluidity

Let us choose a neutron superfluidity model ($\alpha = a, b, c,$ or d) and consider the dependence of the upper cooling curves on the proton superfluidity models β. A comparison of panels (a) and (b) in Figs. 3–6 reveals a qualitative similarity between the cooling curves of low-mass ($M = 1.1M_\odot$) stars when the neutron and proton superfluidities are inverted (i.e., for the models $\alpha\beta$ and $\beta\alpha$).

The quantitative differences between the $\alpha\beta$ and $\beta\alpha$ cooling curves are attributable to different neutron and proton concentrations in the cores of neutron stars and to different types of neutron (triplet) and proton (singlet) pairing. This results in a slightly asymmetric effect of neutrons and protons on the neutrino luminosity and the heat capacity (see, e.g., Yakovlev *et al.* 1999a). Thus, for example, at temperatures T slightly below $T_{\rm c}$, the rate of neutrino energy release due to neutron pairing is approximately an order of magnitude higher than that due to proton pairing (even for the chosen rate constant $\zeta_p = 1$). Therefore, the $b(\beta = a, d)$ and $c(\beta = a, b, d)$ cooling curves (panel (a) in Figs. 4 and 5) lie below the "inverse" $(\alpha = a, d)b$ and $(\alpha = a, b, d)c$ cooling curves (panel (b) in the same figures). On the other hand, the *ad* curve (Fig. 3a) at the photon cooling stage ($t \gtrsim 10^5$ yr) runs below the *da* curve (Fig. 3b). This is because the heat capacity of the neutron-star core is more strongly suppressed by the neutron superfluidity $\alpha = a$ than by the proton superfluidity $\beta = a$. In the remaining cases, the inversion of the neutron and proton superfluidities leads to qualitatively similar (roughly symmetric) cooling curves in Figs. 3–6. For high-mass ($M > M_{\rm D}$) neutron stars, this symmetry was found by Levenfish *et al.* (1999) in their simplified cooling calculations for stars with constant critical neutron and proton temperatures over the stellar core.

A comparison of the upper cooling curves with the observations in Figs. 3–6 shows that there are only

two models of combined nucleon superfluidity that are consistent with the set of observational data. These include the *da* model discussed in the previous section and the "inverse" *ad* model (Figs. 3 and 6). In other words, one (neutron or proton) superfluidity must be weak, while the other must be strong. The remaining models are unable to simultaneously explain the observational data, primarily for four neutron stars (RX J0822−4300, 1E 1207.4−5209, PSR B1055−52, and RX J0720.4−3125), the hottest ones for their ages.

Varying the nucleon superfluidity models, we can constrain the critical nucleon temperatures at which the theory agrees with the observations. In general, the following conditions must be satisfied simultaneously: either $T_{\rm cnt}^{\rm max} \lesssim 2\times10^8$ K and $T_{\rm cp}^{\rm max} \gtrsim 4\times10^9$ K or $T_{\rm cnt}^{\rm max} \gtrsim 5\times10^9$ K and $T_{\rm cp}^{\rm max} \lesssim 2\times10^8$ K.

The models of *moderate neutron and/or proton superfluidity* in the cores of neutron stars with maximum temperatures $T_{\rm cnt}^{\rm max}$ and/or $T_{\rm cp}^{\rm max}$ in the range $\sim (2\times10^8{-}4\times10^9)$ K are inconsistent with the observations of the hottest neutron stars for their ages. We can show that this conclusion is valid for a much broader class of nucleon superfluidity models than those used here (see above). Nevertheless, there is a narrow region of nucleon superfluidity parameters at which the combination of strong nucleon superfluidity of one type and moderate nucleon superfluidity of another type can be reconciled with the observations (see Gusakov *et al.*).

Rate Constant of Neutrino Energy Release due to Cooper Proton Pairing

Let us briefly discuss the sensitivity of the cooling curves to the constant ζ_p in the expression for the rate of neutrino energy release due to Cooper proton pairing. Recall that the value of ζ_p that includes many-body effects is known poorly. In our calculations, we used the (renormalized) value of $\zeta_p = 1$.

As an example, Fig. 7 shows the cooling curves of a low-mass neutron star for three neutron and proton superfluidity models (*db*, *dc*, and *bc*). As was shown above, the neutrino emission due to Cooper pairing is particularly important precisely in low-mass stars. As everywhere in this section, we consider the type-B neutron superfluidity. The lower of the two curves for each superfluidity model was computed with the renormalized constant $\zeta_p = 1$, while the upper curve was computed with the nonrenormalized constant (but obtained by taking into account relativistic effects; see Kaminker *et al.* 1999).

In the *db* model, the proton superfluidity *b* is moderately strong and arises at an early cooling stage.

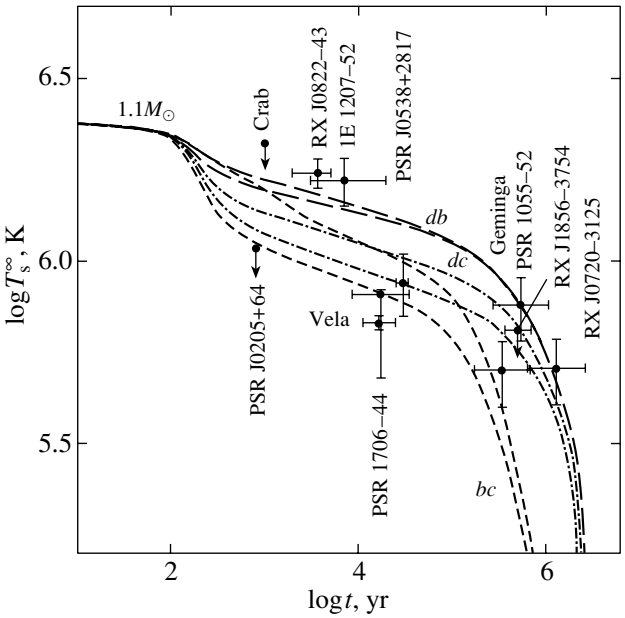

Fig. 7. Cooling curves of a low-mass ($M = 1.1\,M_\odot$) star for three nucleon superfluidity models (*db*, long dashes; *dc*, dashes and dots; *bc*, short dashes) in comparison with the observations. The lower and upper curves for each superfluidity model were computed with the renormalized ($\zeta_p = 1$) and nonrenormalized rate constant of neutrino energy release due to Cooper proton pairing, respectively.

The neutrino emission due to proton pairing plays a relatively minor role, and the exact value of ζ_p weakly affects the cooling.

In the *dc* and, particularly, the *bc* model, moderate proton pairing $\beta = c$ results in intense neutrino emission and appreciably speeds up the cooling. In these cases, the cooling curves are most sensitive to ζ_p. However, as we see from Fig. 7, the ζ_p variations considered cannot lead to agreement of the *dc* and *bc* cooling curves with the observations and, hence, do not affect our conclusions. We believe the renormalized value of $\zeta_p = 1$ to be more realistic than its nonrenormalized value. The existing uncertainty in ζ_p introduces uncertainty into the cooling theory. In particular, for the nonrenormalized value of ζ_p, the approximate symmetry of the cooling curves relative to the inversion of the models of nucleon superfluidity $\alpha\beta$ and $\beta\alpha$ noted above is much less pronounced than that for the renormalized value (see also Yakovlev *et al.* 1999a). The choice of ζ_p may subsequently prove to be important for reconciling the theory with the observations.

THE TWO TYPES OF NEUTRON TRIPLET SUPERFLUIDITY

Let us compare the influence of the two types of neutron triplet superfluidity (B and C) on the cooling

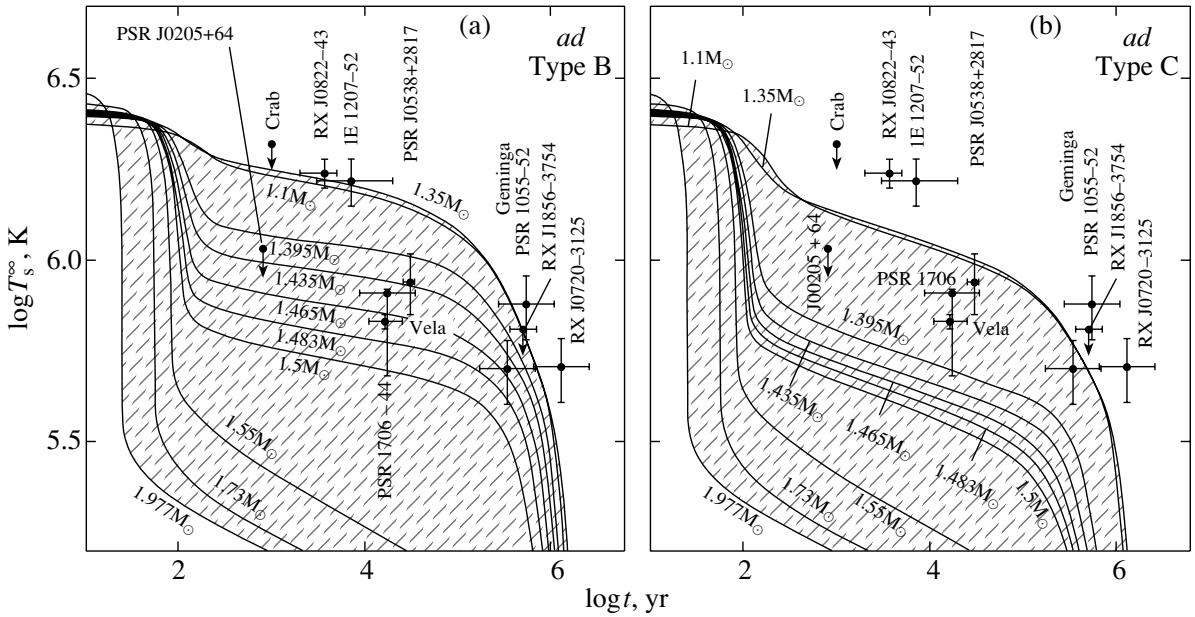

Fig. 8. Same as Fig. 2 for the model *a* of strong type-B (a) and type-C (b) superfluidity and the model *d* of weak proton superfluidity.

of neutron stars. Clearly, significant differences might be expected for strong neutron superfluidity. As follows from the results of the previous section, strong type-B neutron superfluidity (the model *a*) with weak proton superfluidity (the model *d*) can ensure agreement between the theory and the observations. Let us consider this case in more detail. Figure 8 shows the cooling curves for neutron stars of different masses with superfluidity *ad*: in panels (a) and (b), we took the type-B and type-C neutron pairing models, respectively.

It follows from an examination of Fig. 8a that, just as for the *da* model (Fig. 2), we can identify the same three types of cooling neutron stars: *low-mass*, slowly cooling stars; *high-mass*, rapidly cooling stars; and *medium-mass* stars with a moderate cooling rate.

The cooling of neutron stars with type-C neutron superfluidity was first calculated by Schaab *et al.* (1998). However, these authors used an oversimplified description of the influence of superfluidity on the neutrino reactions. More accurate calculations were performed by Gusakov and Gnedin (2002), who compared the results obtained for type-B and -C superfluidities. The authors used the approximation of constant critical temperatures $T_{\rm cp}$ and $T_{\rm cnt}$ over the stellar core. Calculations indicate that, in many cases, the shape of the cooling curves does not change if effective constant critical temperatures close to $T_{\rm cp}(\rho_{\rm c})$ and $T_{\rm cnt}(\rho_{\rm c})$ at the stellar center ($\rho = \rho_{\rm c}$) are used in place of the actual $T_{\rm cp}(\rho)$ and $T_{\rm cnt}(\rho)$ profiles. This approximation is valid when $T_{\rm c}(\rho)$ changes smoothly near the stellar center (e.g., in low-mass stars).

Gusakov and Gnedin (2002) showed that type-C neutron superfluidity speeds up the neutron-star cooling (compared to type-B superfluidity). This is attributable to the power-law suppression of the neutrino processes by type-C superfluidity (in contrast to the exponential suppression in case B; see, e.g., Yakovlev *et al.* 1999a; Gusakov 2002). Our calculations (Fig. 8) indicate that the above conclusion also remains valid in a more realistic approach that takes into account the variations of the critical temperatures $T_{\rm cnt}(\rho)$ and $T_{\rm cp}(\rho)$ over the stellar core.

The cooling curves for low- and medium-mass stars in Fig. 8b lie well below those for stars of the same masses in Fig. 8a. On the other hand, the cooling curves for high-mass ($M \gtrsim 1.55\ M_\odot$) stars in both panels of the figure almost coincide for the obvious reason: the critical temperatures are low in the central regions of these stars ($T_{\rm cnt} \lesssim 10^8$ K, see Fig. 1), so the superfluidity ceases to affect the cooling altogether.

Thus, according to Fig. 8, strong type-C neutron superfluidity disagrees with the observations of the hottest neutron stars for their ages. This superfluidity is still too weak to completely suppress the modified URCA process in a low-mass star, thereby making the star hotter. Of course, the theory can be reconciled with the observations by choosing the model of stronger type-C superfluidity. Our calculations indicate that this requires a $T_{\rm cnt}(\rho)$ profile with the maximum at $T_{\rm cnt}^{\rm max} \sim 10^{11}$ K. However, such strong triplet

superfluidity seems unrealistic. Khodel *et al.* (1998, 2001) gave theoretical arguments against the emergence of type-C superfluidity in neutron stars.

CONCLUSIONS

We have analyzed the cooling of neutron stars with neutron triplet superfluidity and proton singlet superfluidity in their cores. Our results are summarized below.

(1) The cooling curves for neutron stars are qualitatively symmetric relative to the inversion of the neutron and proton superfluidity models. For low-mass ($M < M_{\rm D}$) stars, this symmetry is largely determined by the dimensionless constant $\zeta_p \sim 1$ in the expression for the rate of neutrino energy release due to Cooper proton pairing. At $\zeta_p \ll 1$, obtained without the renormalization of ζ_p including multipartice effects, the symmetry is much less distinct than it is at $\zeta_p \sim 1$, which might be expected after renormalization.

(2) Two types of neutron and proton superfluidity models are consistent with the observations of thermal emission from isolated neutron stars. First, these include the models of strong (type A) proton superfluidity and weak (or completely absent) (type B or C) neutron superfluidity with maximum (over the stellar core) critical temperatures $T_{\rm cp}^{\rm max} \gtrsim 4 \times 10^9$ K and $T_{\rm cnt}^{\rm max} \lesssim 2 \times 10^8$ K. Second, these include the models of strong (type B) neutron superfluidity and weak (or completely absent) proton superfluidity with $T_{\rm cnt}^{\rm max} \gtrsim 5 \times 10^9$ K and $T_{\rm cp}^{\rm max} \lesssim 2 \times 10^8$ K. The models of the first type seem more realistic. Let us note, in particular, a recent paper by Schwenk and Friman (2004), who predicted a weakening of the neutron triplet pairing by effects of the medium.

(3) The models of moderate (type B or C) neutron superfluidity and/or moderate (type A) proton superfluidity with maximum critical temperatures $T_{\rm cnt}^{\rm max}$ and $T_{\rm cp}^{\rm max}$ in the range $\sim 2 \times 10^8$ to $\sim 4 \times 10^9$ K are inconsistent with the observations of primarily the hottest young neutron stars RX J0822−4300 and 1E 1207.4−5209. However, as was shown by Gusakov *et al.* (2004), there is a narrow region of model neutron and proton superfluidity parameters at which agreement between the cooling theory and the observations is also possible for moderate neutron superfluidity ($T_{\rm cnt}^{\rm max} \sim 6 \times 10^8$ K). This possibility was considered Gusakov *et al.* (2004).

(4) Strong type-C neutron triplet superfluidity can appreciably speed up the cooling of middle-aged ($10^3 \lesssim t \lesssim 10^5$ yr) neutron stars compared to type-B superfluidity for the same $T_{\rm cnt}(\rho)$ profiles. For strong type-C neutron superfluidity ($T_{\rm cnt}^{\rm max} \sim 5 \times 10^9$ K) and weak proton superfluidity ($T_{\rm cp}^{\rm max} \lesssim 2 \times 10^8$ K), the theory can no longer be reconciled with the observations of RX J0822−4300, 1E 1207.4−5209, PSR B1055−52, and RX J0720.4−3125, the hottest sources for their ages. For any models of strong or moderate neutron superfluidity, the transition from type-B to type-C superfluidity just enhances the difference between the theory and the observations.

Our analysis is simplified, because we considered only the cores of neutron stars composed of neutrons, protons, and electrons (disregarding the possible existence of hyperons, pion and kaon condensates, or quark matter). Moreover, we chose only one equation of state for matter in the cores of neutron stars and similar profiles of the critical neutron and proton temperatures $T_{\rm c}(\rho)$ in the stellar cores. Varying the equation of state (for the same composition of the matter) leads to a shift in the switch-on threshold of the direct URCA process (to a change in $\rho_{\rm D}$ and $M_{\rm D}$). Varying the $T_{\rm c}(\rho)$ profiles (with their general shape retained) at high $T_{\rm c}^{\rm max} \gtrsim 2 \times 10^9$ K leads to shifts in the characteristic values of ρ at which the superfluidity weakens and ceases to suppress the intense neutrino emission. Both lead to shifts in the boundary masses that separate the three types of cooling neutron stars (Kaminker *et al.* 2002), but do not alter our main conclusions. Significantly, the simplest model of neutron stars with strong proton superfluidity (even without neutron superfluidity) is capable of explaining the available observations.

It should be noted that the cooling of neutron stars also depends on the (singlet) neutron superfluidity in the inner stellar crust, on the magnetic field in the outermost stellar layers, and on the presence or absence of a surface layer of light elements (see, e.g., Potekhin *et al.* 2003). In general, however, these factors have a weaker effect on the cooling than the nucleon superfluidity in the cores of neutron stars considered here. We disregarded them by restricting our analysis to the superfluidity effects in the stellar cores. Our cooling code allows these factors to be easily taken into account, and this may be necessary for interpreting individual sources, primarily the hottest objects for their ages (see, e.g., Potekhin *et al.* 2003). The cooling of neutron stars may also depend on the stellar heating mechanisms related, for example, to the viscous dissipation of differential rotation energy (see, e.g., Page 1998a, 1998b). We emphasize that these heating mechanisms are model dependent. At the same time, the available observations can also be interpreted without invoking them.

Note that the surface temperatures of neutron stars $T_{\rm s}^{\infty}$ are difficult to determine from observational data (see, e.g., Pavlov *et al.* 2002). Reliable observational data and theoretical models of neutron star atmospheres are required to solve this problem.

The existing values of T_s^∞ can change appreciably, which can strongly affect the offered interpretation of the observations of primarily RX J0822–4300, 1E 1207.4–5209, PSR B1055–52, and RX J0720.4–3125. Future observations of the thermal emissions from isolated neutron stars will be crucial in understanding the superfluidity properties of dense matter in stellar cores.

ACKNOWLEDGMENTS

This work was supported by the Russian Foundation for Basic Research (project nos. 02-02-17668 and 03-07-90200), the Russian Leading Scientific Schools Program (project no. 1115.2003.2), and the INTAS YSF (grant no. 03-55-2397).

REFERENCES

1. L. Amundsen and E. Østgaard, Nucl. Phys. A **442**, 163 (1985).
2. R. G. Arendt, E. Dwek, and R. Petre, Astrophys. J. **368**, 474 (1991).
3. M. Baldo, J. Cugnon, A. Lejeune, and U. Lombardo, Nucl. Phys. A **536**, 349 (1992).
4. T. M. Braje and R. W. Romani, Astrophys. J. **580**, 1043 (2002).
5. W. F. Brisken, S. E. Thorsett, A. Golden, and W. M. Goss, Astrophys. J. Lett. **593**, L89 (2003).
6. V. Burwitz, F. Haberl, R. Neuhäuser, *et al.*, Astron. Astrophys. **399**, 1109 (2003).
7. G. W. Carter and M. Prakash, Phys. Lett. B **525**, 249 (2002).
8. E. G. Flowers, M. Ruderman, and P. G. Sutherland, Astrophys. J. **205**, 541 (1976).
9. O. Y. Gnedin, D. G. Yakovlev, and A. Yu. Potekhin, Mon. Not. R. Astron. Soc. **324**, 725 (2001).
10. M. E. Gusakov, Astron. Astrophys. **389**, 702 (2002).
11. M. E. Gusakov and O. Yu. Gnedin, Astron. Lett. **28**, 669 (2002).
12. M. E. Gusakov, A. D. Kaminker, D. G. Yakovlev, and O. Y. Gnedin, Astron. Astrophys. **606**, 444 (2004); astro-ph/0404002.
13. P. Haensel, *Final Stages of Stellar Evolution,* Ed. by J.-M. Hameury and C. Motch (EAS Publ. Ser. EDP Sci., 2003), p. 249.
14. A. D. Kaminker, P. Haensel, and D. G. Yakovlev, Astron. Astrophys. **345**, L14 (1999).
15. A. D. Kaminker, P. Haensel, and D. G. Yakovlev, Astron. Astrophys. **373**, L17 (2001).
16. A. D. Kaminker, D. G. Yakovlev, and O. Y. Gnedin, Astron. Astrophys. **383**, 1076 (2002).
17. D. L. Kaplan, S. R. Kulkarni, M. H. van Kerkwijk, and H. L. Marshall, Astrophys. J. Lett. **570**, L79 (2002).
18. V. A. Khodel, J. W. Clark, and M. V. Zverev, Phys. Rev. Lett. **87**, 031103 (2001).
19. V. A. Khodel, V. V. Khodel, and J. W. Clark, Phys. Rev. Lett. **81**, 3828 (1998).
20. M. Kramer, A. G. Lyne, G. Hobbs, *et al.*, Astrophys. J. Lett. **593**, L31 (2003).
21. J. M. Lattimer, C. J. Pethick, M. Prakash, and P. Haensel, Phys. Rev. Lett. **66**, 2701 (1991).
22. J. M. Lattimer and M. Prakash, Astrophys. J. **550**, 426 (2001).
23. K. P. Levenfish, Yu. A. Shibanov, and D. G. Yakovlev, Pis'ma Astron. Zh. **25**, 491 (1999) [Astron. Lett. **25**, 417 (1999)].
24. U. Lombardo and H.-J. Schulze, *Physics of Neutron Star Interiors,* Ed. by D. Blaschke *et al.* (Springer, Berlin, 2001), p. 30.
25. A. G. Lyne, R. S. Pritchard, F. Graham-Smith, and F. Camilo, Nature **381**, 497 (1996).
26. K. E. McGowan, S. Zane, M. Cropper, *et al.*, Astrophys. J. **600**, 343 (2004).
27. N. Motch, V. E. Zavlin, and F. Haberl, Astron. Astrophys. **408**, 323 (2003).
28. D. Page, NATO ASI Ser. C **515**, 539 (1998).
29. D. Page, *Neutron Stars and Pulsars*, Ed. by N. Shibazaki *et al.* (Univ. Acad. Press, Tokyo, 1998), p. 183.
30. G. G. Pavlov and V. E. Zavlin, in *Proceedings of the XXI Texas Symposium on Relativistic Astrophysics,* Ed. by R. Bandiera *et al.* (World Sci., Singapore, 2003), p. 319.
31. G. G. Pavlov, V. E. Zavlin, D. Sanwal, *et al.*, Astrophys. J. Lett. **552**, L129 (2001).
32. G. G. Pavlov, V. E. Zavlin, and D. Sanwal, *WE-Heraeus Seminar on Neutron Stars, Pulsars and Supernova Remnants No. 270*, Ed. by W. Becker *et al.* (MPE-Report No. 278, Garching, 2002), p. 273.
33. J. A. Pons, F. Walter, J. Lattimer, *et al.*, Astrophys. J. **564**, 981 (2002).
34. A. Y. Potekhin, D. G. Yakovlev, G. Chabrier, and O. Y. Gnedin, Astrophys. J. **594**, 404 (2003).
35. M. Prakash, T. L. Ainsworth, and J. M. Lattimer, Phys. Rev. Lett. **61**, 2518 (1988).
36. R. S. Roger, D. K. Milne, M. J. Kesteven, *et al.*, Astrophys. J. **332**, 940 (1988).
37. Ch. Schaab, F. Weber, and M. K. Weigel, Astron. Astrophys. **335**, 596 (1998).
38. A. Schwenk and B. Friman, Phys. Rev. Lett. **92**, 082501 (2004).
39. P. O. Slane, D. J. Helfand, and S. S. Murray, Astrophys. J. Lett. **571**, L45 (2002).
40. J. E. Trümper, V. Burwitz, F. Haberl, and V. E. Zavlin, astro-ph/0312600 (2003).
41. F. M. Walter, Astrophys. J. **549**, 433 (2001).
42. F. M. Walter and J. M. Lattimer, Astrophys. J. Lett. **576**, L145 (2002).
43. M. C. Weisskopf, S. L. O'Dell, F. Paerels, *et al.*, Astrophys. J. **601**, 1050 (2004).
44. P. F. Winkler, J. H. Tuttle, R. P. Kirshner, and M. J. Irwin, *Supernova Remnants and the Interstellar Medium,* Ed. by R. S. Roger and T. L. Landecker (Cambridge Univ. Press, Cambridge, 1988), p. 65.
45. D. G. Yakovlev, O. Y. Gnedin, A. D. Kaminker, and A. Y. Potekhin, *WE-Heraeus Seminar on Neutron Stars, Pulsars and Supernova Remnants No. 270*, Ed. by W. Becker *et al.* (MPE-Report No. 278, Garching, 2002), p. 287.

46. D. G. Yakovlev, A. D. Kaminker, and O. Y. Gnedin, Astron. Astrophys. **379**, L5 (2001).
47. D. G. Yakovlev, A. D. Kaminker, O. Y. Gnedin, and P. Haensel, Phys. Rep. **354**, 1 (2001).
48. D. G. Yakovlev, A. D. Kaminker, and K. P. Levenfish, Astron. Astrophys. **343**, 650 (1999).
49. D. G. Yakovlev, K. P. Levenfish, and Yu. A. Shibanov, Usp. Fiz. Nauk **169**, 825 (1999).
50. S. Zane, F. Haberl, M. Cropper, *et al.*, Mon. Not. R. Astron. Soc. **334**, 345 (2002).
51. V. E. Zavlin and G. G. Pavlov, in *Proceedings of the EPIC Consortium, Palermo, Oct. 14–16, 2003*; astro-ph/0312326 (2003).
52. V. E. Zavlin, G. G. Pavlov, and D. Sanwal, Astrophys. J. **606**, 444 (2004); astro-ph/0312096.
53. V. E. Zavlin, J. Trümper, and G. G. Pavlov, Astrophys. J. **525**, 959 (1999).

Translated by V. Astakhov

Astronomy Letters, Vol. 30, No. 11, 2004, pp. 772–778. Translated from Pis'ma v Astronomicheskiĭ Zhurnal, Vol. 30, No. 11, 2004, pp. 848–854.

Broadband X-ray Spectrum of the Intermediate Polar V2400 Oph

M. G. Revnivtsev[1,2*], A. A. Lutovinov[1], B. F. Suleimanov[3,2], S. V. Molkov[1], and R. A. Sunyaev[1,2]

[1]*Space Research Institute, Russian Academy of Sciences, Profsoyuznaya ul. 84/32, Moscow 117810, Russia*
[2]*Max Planck Institut für Astrophysik, Karl Schwarzschild Str. 1, Postfach 1317, D-85741 Garching, Germany*
[3]*Kazan State University, ul. Lenina 18, Kazan, 420008 Tatarstan, Russia*

Received May 12, 2004

Abstract—We present the results of our analysis of the observations of the intermediate polar V2400 Oph by the INTEGRAL and RXTE observatories. We reconstructed the spectrum of the source over a wide (3–100 keV) energy range. The spectrum obtained can be fitted by a computed theoretical model of the post-shock emitting region with $T_{\max} \sim 22$ keV. As a result, we estimated the mass ($0.59 M_{\odot}$) and radius (8.8×10^8 cm) of the white dwarf in the system V2400 Oph. © *2004 MAIK "Nauka/Interperiodica".*

Key words: *X-ray sources, white dwarfs.*

INTRODUCTION

The magnetic cataclysmic variables (binary systems with a white dwarf as the compact object) are subdivided into two large classes, depending on the influence of the magnetic field of the white dwarf on the configuration of the accreting system (see, e.g., Warner 1995): ordinary and intermediate polars. The white dwarf in an ordinary polar has a magnetic field strength (10–50 MG) such that it synchronizes its rotation with the orbital motion of the binary system. In such systems, matter flows (accretes) along magnetic field lines directly onto the surface of the white dwarf without the formation of an accretion disk. The magnetic field in intermediate polars is weaker, ~ 10 MG, which enables the matter flowing from the optical companion through the inner Lagrangian point of the system to form an accretion disk. Subsequently, the accretion disk is destroyed as it approaches the surface of the white dwarf, and matter accretes onto the polar caps of the white dwarf just as in ordinary polars (see, e.g., Aizu 1973; Lamb and Masters 1979). There is the unique system V2400 Oph among the discovered polars that, on the one hand, shows evidence of an intermediate polar: the spin period of the white dwarf is much shorter than the binary period. On the other hand, there is ample evidence that the system has no accretion disk (Buckley *et al.* 1995, 1997; Hellier and Beardmore 2002). The X-ray emission produced by the optically thin radiation of a shock-heated hot plasma near the surface of the white dwarf pulsates in this system with a period that differs from the spin period of the white dwarf. The reason is that the matter outflowing through the inner Lagrangian point accretes alternately on one and the other magnetic poles of the white dwarf. As a result, the X-ray emission pulsates with the beat period between the orbital period ($P_{\rm orb} \sim 3.42$ h) and the spin period of the white dwarf ($P_{\rm WD} \sim 927$ s): $P_{\rm pul} \sim 1003$ s.

The X-ray emission mechanism for intermediate polars provides a unique opportunity to estimate the mass of the white dwarf directly from X-ray observations (Rothschild *et al.* 1981). Much of the energy in such objects is emitted in the region immediately behind the shock front that emerges near the surface of the white dwarf in the path of the accreting matter (Aizu 1973; Fabian *et al.* 1976; Lamb and Masters 1979). The emergent X-ray spectrum of an object can be calculated by calculating the structure of this region and the temperature and density profiles of the settling matter. The maximum temperature in the post-shock region is directly related to the mass and radius of the white dwarf (Fabian *et al.* 1976). Since the radius of the white dwarf is determined mainly by its mass (see, e.g., Nauenberg 1972), the maximum temperature actually depends only on the mass of the white dwarf. In contrast to ordinary polars, intermediate polars have a much weaker magnetic field. This rules out the strong influence of cyclotron losses on the energy balance in the post-shock region (Wu *et al.* 1995) and, thus, greatly simplifies the calculations of the structure of this region and its emergent spectrum.

*E-mail: mikej@hea.iki.rssi.ru

1063-7737/04/3011-0772$26.00

The typical parameters of white dwarfs (their masses and radii) are such that the maximum post-shock temperature ranges from 10 to 40 keV. Thus, for the spectral shape of polars to be constrained, the sensitivity must be high at energies >20 keV. Until recently, there have been very few measurements of the polar spectra at these energies (see, e.g., Rothschild *et al.* 1981; Di Martino *et al.* 2001, 2004). Now, with the launch of the INTEGRAL observatory, we may expect great progress in this field.

In this paper, we present the hard X-ray spectra of the intermediate polar V2400 Oph (RX J1712–2414), as constructed from INTEGRAL and RXTE data. We estimate the mass and radius of the white dwarf by comparing the observed and computed spectra.

DATA ANALYSIS

The INTEGRAL (International Gamma-Ray Astrophysics Laboratory) observatory was launched into a high-apogee orbit by a Proton launcher from the Baikonur Cosmodrome on October 17, 2002 (Eismont *et al.* 2003). The scientific payload of the observatory included four instruments that enable simultaneous studies of a source in the X-ray, gamma-ray, and optical ranges (Winkler *et al.* 2003).

In August–September 2003, the INTEGRAL observatory performed deep observations of the region of the Galactic Center (Revnivtsev *et al.* 2004). Several dozen sources, including the intermediate polar V2400 Oph, were detected within the INTEGRAL field of view at a statistically significant level. The total effective exposure time for the source (with allowance made for the dependence of the effective area on the distance from the center of the telescope's field of view) was $\sim 1.2 \times 10^6$ s.

Since the source during these observations was far from the optical axis of the INTEGRAL telescopes, it was outside the field of view of the JEM-X X-ray monitor. The data from the SPI/INTEGRAL spectrometer were also difficult to use, because its angular resolution is $\sim 2.^\circ5$ (Vedrenne *et al.* 2003) and because the bright Oph cluster of galaxies lies at a distance of $\sim 50'$ from V2400 Oph. Therefore, we analyzed only the data from the ISGRI detector of the IBIS telescope with a high angular resolution (Lebrun *et al.* 2003). The ISGRI/IBIS image of the sky region around V2400 Oph in the energy range 18–60 keV is shown in Fig. 1.

The data obtained were processed using methods described previously (Revnivtsev *et al.* (2004)). To construct the spectrum of the source, we used the ratio of its fluxes, measured in different energy ranges, to the IBIS/ISGRI fluxes recorded from the Crab Nebula in the same energy ranges. In this case, the standard shape of the spectrum for the Crab Nebula $dN(E) = 10E^{-2.1}dE$ phot. cm^{-2} s^{-1} keV^{-1} was used. To test the validity of the algorithms used for data processing and for estimating the amplitude of the systematic uncertainties in the spectra obtained, we applied the method mentioned above to a series of calibration observations for the Crab Nebula. Our analysis of the IBIS/ISGRI data revealed a systematic uncertainty of 2–5% for the spectral analysis and $\sim$10% for the absolute flux normalization. Therefore, we subsequently renormalized the IBIS/ISGRI flux to the RXTE/PCA spectrum.

To supplement the hard X-ray data with observational data in the standard X-ray range and to obtain a broadband X-ray spectrum of V2400 Oph, we used publicly available RXTE data, those from the PCA and HEXTE spectrometers obtained over the period 1996–2003. The RXTE data were analyzed by means of the standard FTOOLS/LHEASOFT package, version 5.3. To reduce the systematic uncertainties in the spectra, we used only the upper layer of the PCA detector anodes and excluded from our analysis the data from the PCU0 detector, because it had had no propane veto layer; this greatly reduced the influence of the background on the results obtained since 2000. The background of the PCA spectrometer was calculated using the CM17_240 model for weak sources. The HEXTE spectrometer continuously monitors the background spectrum of its detectors by repointing at a distance of $\pm 1.^\circ5$ from the object. We used only those observations for which the background spectra of the HEXTE detectors at angular distances of $+1.^\circ5$ and $-1.^\circ5$ from the object were identical. The total exposure time of the observations used was $\sim 230 \times 10^3$ s.

Observations indicate that the shapes of the spectra for intermediate polars change only slightly with time, which allowed us to investigate the spectrum of the source averaged over all RXTE observations.

THE MODEL AND RESULTS

The emission from intermediate polars at energies $\sim$3–100 keV can be roughly decomposed into three spectral components, in order of significance of their influence on the spectral shape:

(1) The optically thin radiation of the hot post-shock region;

(2) The photoabsorption of part of this radiation in the stream of cold pre-shock accreting matter;

(3) The reflection and reprocessing of the hard X-ray emission from the hot region in the upper surface layers of the white dwarf.

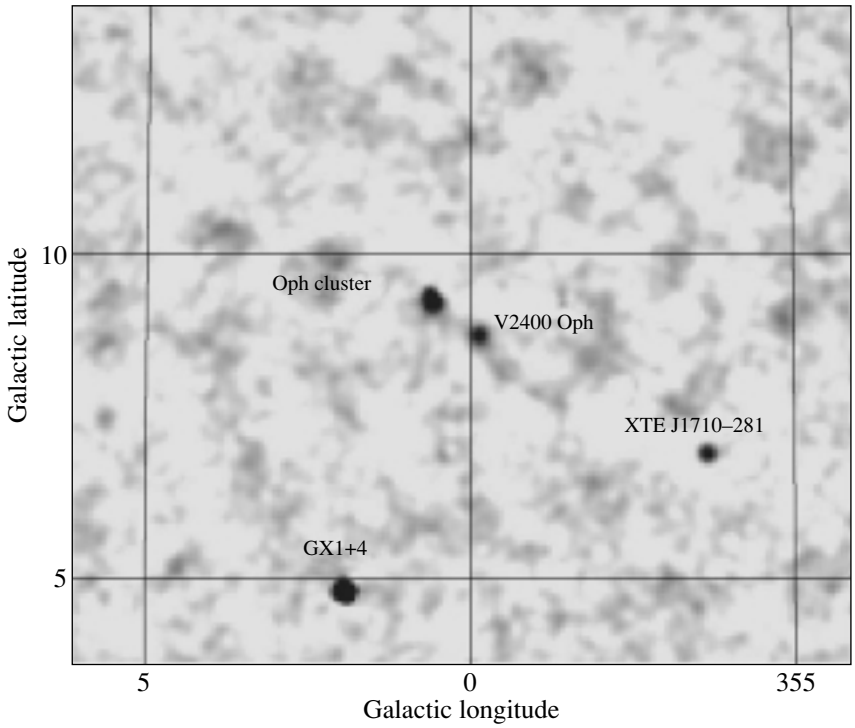

Fig. 1. Image of the sky region with the intermediate polar V2400 Oph constructed from ISGRI detector data in the energy range 18–60 keV.

The contribution of the cyclotron component to the total spectrum of intermediate polars is assumed to be small (see, e.g., Wu *et al.* 1995), because their magnetic fields are relatively weak (<10 MG).

To a first approximation, the spectrum of the hot post-shock region may be assumed to be described by the radiation of a single-temperature, optically thin plasma with the contribution of emission lines (see, e.g., Di Martino 2001, 2004). However, a more detailed analysis shows that the mass of the white dwarf (estimated from the temperature of the optically thin post-shock plasma) proves to be slightly underestimated for this spectral fit. For the mass to be estimated more accurately, we must abandon the assumption that the post-shock layer is a single-temperature one and calculate its structure.

The steady-state one-dimensional structure of the post-shock region is described by the following equations (see, e.g., Wu 1994; Wu *et al.* 1994):

the continuity equation

$$\frac{d}{dz}(\rho v) = 0, \tag{1}$$

the momentum equation

$$\frac{d}{dz}(\rho v^2 + P) = -\frac{GM_{\rm WD}}{z^2}\rho, \tag{2}$$

the energy equation

$$v\frac{dP}{dz} + \gamma P\frac{dv}{dz} = -(\gamma - 1)\Lambda, \tag{3}$$

and the equation of state for an ideal gas

$$P = \frac{\rho kT}{\mu m_{\rm H}}. \tag{4}$$

Here, z is the coordinate measured from the center of the white dwarf; v, ρ, T, and P are the plasma velocity, density, temperature, and pressure, respectively; $M_{\rm WD}$ is the mass of the white dwarf; $\gamma = 5/3$ is the adiabatic index; and $\mu = 0.62$ is the mean molecular weight of the accreting plasma with solar elemental abundances. The rate of cooling through optically thin plasma radiation, Λ, was calculated as

$$\Lambda = \left(\frac{\rho}{\mu m_{\rm H}}\right)^2 \Lambda_N(T), \tag{5}$$

where $\Lambda_N(T)$ is the cooling function for a plasma with solar elemental abundances taken from the paper by Sutherland and Dopita (1993).

Equation (1) has the integral

$$\rho v = a, \tag{6}$$

where a is the local accretion rate ($[a]$=g cm^{-2} s^{-1}), a free parameter of the model under consideration. However, further calculations show that the spectrum is virtually independent of this parameter.

Equations (2) and (3) can be rewritten using (6) with the substitution $z' = z_0 - z$, where z_0 is the coordinate of the shock front, as

$$\frac{dv}{dz'} = g(z')\frac{1}{v} - \frac{1}{a}\frac{dP}{dz'}, \quad (7)$$

$$\frac{dP}{dz'} = \frac{(\gamma-1)\Lambda a + g(z')\gamma P a/v}{\gamma P - av}, \quad (8)$$

where

$$g(z') = \frac{GM_{WD}}{(z_0 - z')^2}.$$

Equations (7) and (8) were solved from $z = z_0$ ($z' = 0$) to $z = R_{\rm WD}$ ($z' = z_0 - R_{WD}$) with the following boundary conditions at $z = z_0$ (Wu *et al.* 1994):

$$v_0 = 0.25\sqrt{2GM_{\rm WD}/z_0}, \quad (9)$$

$$\rho_0 = a/v_0, \quad (10)$$

$$P_0 = 3av_0, \quad (11)$$

$$T_0 = 3\frac{\mu m_{\rm H}}{k}v_0^2. \quad (12)$$

In our model, we assumed the radius of the white dwarf to be related to its mass by the relation (Nauenberg 1972)

$$R_{WD} = 7.8\times10^8 \quad (13)$$
$$\times\left[\left(\frac{1.44M_\odot}{M_{\rm WD}}\right)^{2/3} - \left(\frac{M_{\rm WD}}{1.44M_\odot}\right)^{2/3}\right]^{1/2} \text{ cm}.$$

Here, it is important to note that the accretion structure under consideration is optically thin to most of the hard X-ray radiation emitted by it. This is also true for the preshock cold gas. Therefore, the radiative heating of the preshock gas has no appreciable effect on the structure of the model considered here.

The structure of the post-shock region in the described model depends on two parameters: the mass of the white dwarf and the specific mass accretion rate a (i.e., the accretion rate per unit surface area of the white dwarf). As was noted above, an analysis of the solutions obtained shows that the dependence of the emergent spectrum on the specific accretion rate a is very weak. Therefore, although the structure of the post-shock region, in particular, the shock height, the velocity v_0 and density of the matter, depend on the local accretion rate, in fact, the X-ray spectrum being formed in it depends only on the mass of the white dwarf. For this reason, in our subsequent calculations, we took the specific accretion rate to be $1\ \text{g cm}^{-2}\ \text{s}^{-1}$.

The computed post-shock plasma density and temperature profiles are shown in Fig. 2 for a white dwarf with a mass of $M_{\rm WD} = 0.6M_\odot$ in arbitrary units. The maximum post-shock matter temperature $T_{\max}$ and density $\rho_{\max}$ are reached immediately behind the shock front and near the surface of the white dwarf, respectively. In this case, the maximum density is arbitrary, because in our model we do not consider the joining of the post-shock region and the atmosphere of the white dwarf. The model under consideration is more accurately described by the density immediately behind the shock front, $\rho_0 \sim 9.4\times10^{-9}\ \text{g cm}^{-3}$ (which corresponds to a specific accretion rate of $a = 1\ \text{g cm}^{-2}\ \text{s}^{-1}$ and a velocity of $v_0 \sim 1.06\times10^8\ \text{cm s}^{-1}$).

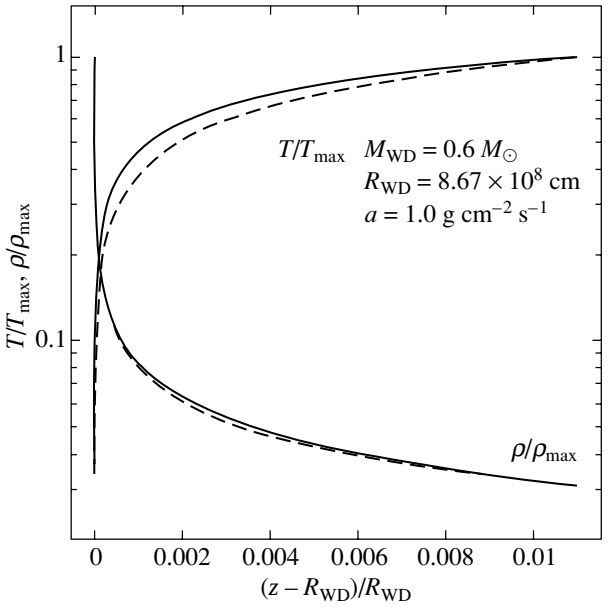

Fig. 2. Post-shock plasma temperature and density profiles. The curves indicate the post-shock plasma temperature and density profiles computed under the simplified assumptions of the model by Frank *et al.* (2002). $T_{\max}$ and $\rho_{\max}$ are the maximum post-shock temperature and density, respectively.

To test the validity of the model under consideration, it is interesting to compare our computed density and temperature profiles with those obtained in the analytical model by Frank *et al.* (2002) (see Fig. 2). The structure of the post-shock region in their model is described by the solutions

$$T(z) = T_0\left(\frac{z - R_{\rm WD}}{z_0 - R_{\rm WD}}\right)^{2/5}, \quad (14)$$

$$\rho(z) = \rho_0\left(\frac{z - R_{\rm WD}}{z_0 - R_{\rm WD}}\right)^{-2/5}. \quad (15)$$

The analytical model assumes that the post-shock pressure is constant, while the pressure in our calculations increases as the surface of the white dwarf

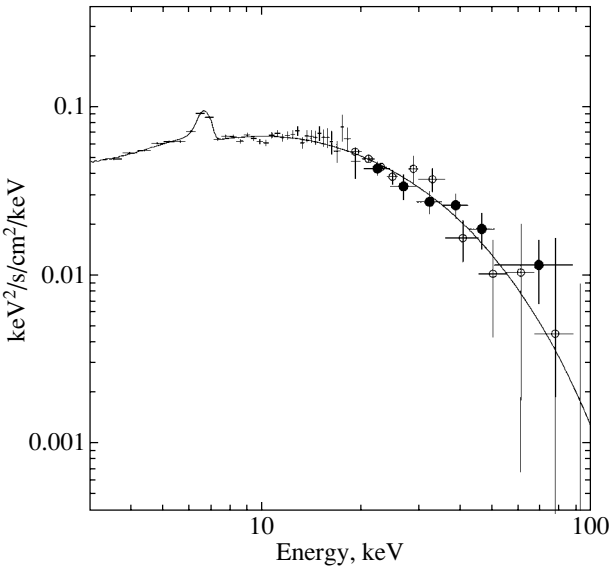

Fig. 3. Broadband spectrum of V2400 Oph obtained by the INTEGRAL and RXTE observatories. The open and filled circles and the crosses indicate the RXTE/HEXTE, INTEGRAL/IBIS/ISGRI, and RXTE/PCA measurements, respectively.

is approached. The dashed lines in Fig. 2 indicate the temperature and density profiles that are given by solutions (14) and (17) normalized to our values of $T_{\max}$, ρ_0, and z_0. We see that our solution is in good agreement with the analytical model. However, since the pressure in the model under study increases as the surface of the white dwarf is approached, the temperature and density in it prove to be slightly higher. The spectrum exhibits only a region with energies above 3 keV; therefore, we did not accurately calculate the relatively cold transition region between the atmosphere of the white dwarf and the accretion structure, the contribution of which is small at these energies.

Best-fit parameters for the broadband spectrum of V2400 Oph

Parameter	Value
$M_{\rm WD}$, $M_\odot$	0.59 ± 0.05
$C_f^{\rm a}$	0.4 ± 0.1
$N_{\rm H}$, 10^{22} cm^{-2}	29 ± 10
$F_{3-100}^{\rm b}$, 10^{-10} erg s^{-1} cm^{-2}	2.43 ± 0.05
$F_{0.1-100}^{\rm c}$, 10^{-10} erg s^{-1} cm^{-2}	5.6

[a] Part of the absorbed X-ray flux.
[b] Observed X-ray flux in the energy range 3–100 keV.
[c] Bolometric X-ray flux in the energy range 0.1–100 keV obtained from the model and corrected for photoabsorption.

Since a detailed study of emission lines in the spectrum of the source was not our objective and since the spectral resolution of the instruments used was not high enough ($\sim$ 1–1.5 keV at energy 6–7 keV), we used a simple bremsstrahlung model (without emission lines) to compute the continuum. This simple approach does not allow any emission lines in the spectrum to be described. However, most of the lines are emitted at energies below 3 keV, i.e., in an unobservable spectral range. In addition, apart from the lines of the hot post-shock region proper, the observed set of lines near 6.6 keV includes the K_α iron line formed through the reflection of hard X-ray emission of the region under consideration from the atmosphere of the white dwarf outside the accretion structure. Since in our case we could not separate the lines of the hot region from the line formed through the reflection, we did not compute them. At the same time, it should be noted that a theoretical study of the observed set of lines is of interest both in testing the model and in investigating the physics of the ongoing processes. This problem will be studied in a separate paper. In the subsequent fitting of the observed spectrum, the presence of emission lines was taken into account by introducing a broad Gaussian line at energy $\sim$ 6.6 keV.

The emitted spectrum of the hot region was calculated as follows:

$$F_E = \int\limits_{R_{WD}}^{z_0} j(z)dz, \qquad (16)$$

where the local spectra of an optically thin plasma (at each height from the surface of the white dwarf) were taken in the form (Zombeck 1990)

$$j(z) = 9.52 \times 10^{-38} \left(\frac{\rho(z)}{\mu m_{\rm H}}\right)^2 \qquad (17)$$
$$\times\, T(z)^{-1/2} \left(\frac{E}{kT(z)}\right)^{-2/5} e^{-\frac{E}{kT(z)}}.$$

To obtain the total spectrum of the intermediate polar, we also took into account the photoabsorption of part of the radiation from the hot region in the stream of cold accreting matter (the fraction C_f of the radiation is absorbed in neutral matter with an equivalent column density $N_{\rm H}$).

As was shown, for example, by Cropper *et al.* (1998), the contribution of the reflection component for polars changes the shape of the spectrum only slightly. Moreover, including the INTEGRAL and RXTE spectral measurements of V2400 Oph at energies above 20 keV further reduces the influence of

the reflection component on the parameters of the emitting region of the white dwarf being determined. Therefore, we disregarded the contribution of this component in our model.

Thus, the model parameters in our fit are:

(1) The mass of the white dwarf;

(2) The fraction of the flux that undergoes photoabsorption;

(3) The equivalent photoabsorption column density.

Figure 3 shows the broadband energy spectrum of the intermediate polar V2400 Oph obtained by the INTEGRAL and RXTE observatories in the energy range 3–100 keV. We see that the flux from the source for the INTEGRAL data is recorded up to energies ~ 80–100 keV at a statistically significant level. We used a grid of theoretical spectra for the model described above to fit the spectrum obtained. The only grid parameter on which the shape of the spectrum depends is the mass of the white dwarf. The availability of high-quality data at energies above 20 keV allows us to determine the model parameters much more accurately, in particular, to reliably record the exponential cutoff in the spectrum of the intermediate polar. We see from Fig. 3 that the model used (solid line) describes well the observed spectrum of the source. The best-fit parameters are given in the table.

As was noted above, the energy resolution of the RXTE/PCA spectrometer is too low to reliably resolve the set of emission lines at energies of 6–7 keV. Therefore, the table does not give the parameters of the broad line at these energies that was formally included in the model and is present in the figure.

CONCLUSIONS

In the previous section, we considered the radiation model for an intermediate polar in which we took into account the fact that the post-shock layer was not a single-temperature one and computed the temperature and density profiles in it. The X-ray spectrum forming in this layer was shown to depend only on the mass of the white dwarf. The model considered was used to describe the broadband spectrum of the intermediate polar V2400 Oph obtained by the RXTE and INTEGRAL observatories in the energy range 3–100 keV. The best-fit parameters yield a mass estimate for the white dwarf in this system, $M_{\rm WD} = 0.59 \pm 0.05 M_\odot$. Using Eq. (13), we obtained the radius of the compact object in V2400 Oph, $R_{\rm WD} = (8.8 \pm 0.7) \times 10^8$ cm. Our value of the mass of the white dwarf is slightly lower than that from Ramsay (2000). This may be because we used data at energies above 20 keV, which significantly reduces the systematic uncertainties in the masses of white dwarfs in systems of polars.

Based on the suggested model and the parameters of the white dwarf determined by fitting the spectrum of the intermediate polar V2400 Oph, we can estimate the height of the shock above its surface, $H_{\rm s} \simeq 0.011 R_{\rm WD} (a/1\ {\rm g\ cm^2\ s^{-1}})^{-1} = 9.68 \times 10^6 (a/1\ {\rm g\ cm^2\ s^{-1}})^{-1}$ cm. For comparison, the analytically estimated height of the shock (Frank *et al.* 2002) is slightly larger at $a = 1$ g cm^2 s^{-1}: $H_{\rm s}^{\rm FKR} \simeq 0.016 R_{\rm WD} = 1.41 \times 10^7$ cm. The temperature in the post-shock region decreases in accordance with the solution of the system of equations (7)–(8) shown in Fig. 2 from a maximum value of $T_{\rm max} \sim 22$ keV ($\sim 2.5 \times 10^8$ K) at the boundary of the shock front to a minimum value near the surface of the white dwarf that cannot not be determined accurately in our model. Here, it is pertinent to note that the broadband spectrum of the intermediate polar V2400 Oph can be satisfactorily described by the simpler bremsstrahlung model of a single-temperature, optically thin plasma with $kT = 15 \pm 1$ keV, in agreement with the temperature profile derived from our model. However, it is important to know the maximum temperature in the post-shock region to properly estimate the mass of the white dwarf, and we would underestimate the mass of the white dwarf if we used a single-temperature spectral fit.

ACKNOWLEDGMENTS

We wish to thank E.M. Churazov, who developed the algorithms for analyzing the IBIS data and who provided us with the software. This work was supported by the Ministry of Industry and Science (Presidential grant no. NSh-2083.2003.2), the Nonstationary Phenomena in Astronomy Program of the Russian Academy of Sciences, and the Russian Foundation for Basic Research (project no 04-02-17276). We are grateful to the INTEGRAL Science Data Centre (Versoix, Switzerland) and the Russian INTEGRAL Science Data Center (Moscow, Russia). The results of this work are based on observations of the INTEGRAL observatory, a ESA mission with the participation of Denmark, France, Germany, Italy, Spain, Switzerland, the Czech Republic, Poland, Russia, and the USA. We also used data from the High-Energy Astrophysics Science Archive Research Center (HEASARC) of the Goddard Space Flight Center.

REFERENCES

1. K. Aizu, Prog. Theor. Phys. **49**, 1184 (1973).

2. D. Buckley, F. Haberl, C. Motch, *et al.*, Mon. Not. R. Astron. Soc. **287**, 117 (1997).
3. D. Buckley, K. Sekiguchi, C. Motch, *et al.*, Mon. Not. R. Astron. Soc. **275**, 1028 (1995).
4. M. Cropper, G. Ramsay, and K. Wu, Mon. Not. R. Astron. Soc. **293**, 222 (1998).
5. D. Di Martino, G. Matt, T. Belloni, *et al.*, Astron. Astrophys. **415**, 1009 (2004).
6. D. Di Martino, G. Matt, K. Mukai, *et al.*, Astron. Astrophys. **377**, 499 (2001).
7. N. A. Eismont, A. V. Ditrikh, G. Janin, *et al.*, Astron. Astrophys. **411**, L37 (2003).
8. J. Frank, A. King, and D. Raine, *Accretion Power in Astrophysics*, 3rd ed. (Cambridge Univ. Press, Cambridge, 2002).
9. A. Fabian, J. Pringle, and M. Rees, Mon. Not. R. Astron. Soc. **175**, 43 (1976).
10. C. Hellier and A. Beardmore, Mon. Not. R. Astron. Soc. **331**, 407 (2002).
11. D. Lamb and A. Masters, Astrophys. J. Lett. **234**, L117 (1979).
12. F. Lebrun, J. Leray, P. Lavocat, *et al.*, Astron. Astrophys. **411**, L141 (2003).
13. M. Nauenberg, Astrophys. J. **175**, 417 (1972).
14. G. Ramsay, Mon. Not. R. Astron. Soc. **314**, 403 (2000).
15. M. G. Revnivtsev, R. A. Syunyaev, D. A. Varshalovich, *et al.*, Astron. Zh. **30**, 426 (2004) [Astron. Rep. **30**, 382 (2004)].
16. R. E. Rothschild, D. E. Gruber, F. K. Knight, *et al.*, Astrophys. J. **250**, 723 (1981).
17. R. S. Sutherland and M. A. Dopita, Astrophys. J., Suppl. Ser. **88**, 253 (1993).
18. G. Vedrenne, J.-P. Roques, V. Schonfelder, *et al.*, Astron. Astrophys. **411**, L63 (2003).
19. B. Warner, *Cataclysmic Variable Stars* (Cambridge Univ. Press, Cambridge, 1995).
20. C. Winkler, T. J.-L. Courvoisier, G. Di Cocco, *et al.*, Astron. Astrophys. **411**, L1 (2003).
21. K. Wu, Astron. Soc. Australia Proc. **11**, 61 (1994).
22. K. Wu, G. Chanmugam, and G. Shaviv, Astrophys. J. **426**, 664 (1994).
23. K. Wu, G. Chanmugam, and G. Shaviv, Astrophys. J. **455**, 260 (1995).
24. M. V. Zombeck, *Handbook of Astronomy and Astrophysics* (Cambridge Univ. Press, Cambridge, 1990).

Translated by V. Astakhov

Astronomy Letters, Vol. 30, No. 11, 2004, pp. 779–784. Translated from Pis'ma v Astronomicheskiĭ Zhurnal, Vol. 30, No. 11, 2004, pp. 855–860.

Photometric Variability and Spectrum of the Post-AGB Candidate IRAS 19200+3457

V. P. Arkhipova*, N. P. Ikonnikova, R. I. Noskova, G. V. Komissarova, and V. F. Esipov

Sternberg Astronomical Institute, Universitetskii pr. 13, Moscow, 119992 Russia

Received March 25, 2004

Abstract—We present our photoelectric and spectroscopic observations of the early B supergiant with an IR excess IRAS 19200+3457, a poorly known post-AGB candidate. The star has been found to be photometrically variable. We observed rapid irregular brightness variations with amplitudes up to $\Delta V = 0\overset{m}{.}4$, $\Delta B = 0\overset{m}{.}4$, and $\Delta U = 0\overset{m}{.}5$. IRAS 19200+3457 and three other hot post-AGB stars—V886 Her, V1853 Cyg, and LSIV−12°111—exhibit a similar variability pattern. Our low-resolution spectroscopic observations in the period 2001–2003 show that the spectrum of IRAS 19200+3457 represents an early B star with hydrogen emission lines originating from a circumstellar gaseous envelope. The HeI λ5876 Å, λ6678 Å, λ7065 Å, and OI λ7774 Å lines are in absorption. The hydrogen and, probably, HeI lines proved to be variable. Our observations confirm the conclusion that IRAS 19200+3457 belongs to the class of intermediate-mass protoplanetary objects. © *2004 MAIK "Nauka/Interperiodica"*.

Key words: *post-AGB supergiants, photometry and spectroscopy.*

INTRODUCTION

LSII +34°1 =IRAS 19200+3457 ($19^{\rm h}21^{\rm m}55^{\rm s}$ + 35°02′55″ (2000)) is a star from the *Catalog of Luminous Stars* (Stock *et al.* 1960). The IRAS satellite recorded far-infrared emission from the object for which cold dust with $T = 166$ K is responsible (Preite-Martinez 1988). The star was also detected by Stephenson (1986) during an Hα sky survey. Based on the far-infrared color characteristics of the star, Preite-Martinez (1986) included IRAS 19200+3457 in the list of possible planetary nebulae. Gauba *et al.* (2003) consider IRAS 19200+3457 as a hot post-AGB candidate, since this B supergiant lies at a high Galactic latitude $b = +9\overset{\circ}{.}51$), has a detached cold dust envelope, and exhibits far-infrared color indices similar to those of planetary nebulae. These authors performed $UBVRIJHK$ photometry of the star and estimated the total and interstellar extinction, but their observations with an Hα filter revealed no line intensity excess above the continuum.

The goal of our study was to perform photometric and spectroscopic observations of IRAS 19200+3457 to reveal the star's possible variability. Knowledge of the variability pattern can provide the key to understanding the processes in the star at the evolutionary phase in question.

Studies of other hot emission-line stars with detectable far-infrared emission, the possible progenitors of planetary nebulae (OY Gem, V886 Her, V1853 Cyg, LSIV−12°111), have revealed the common properties of this (as yet small) group of stars (Arkhipova 1989; Arkhipova and Ikonnikova 1992; Arkhipova *et al.* 1996, 2001a, 2001b, 2002; Smith and Lambert 1994). The low-amplitude photometric variability on short time scales, the appreciable variability of the emission-line profiles, and the P Cyg profiles of some of these lines suggest the possible pulsational activity and the ongoing mass loss in these stars.

UBV OBSERVATIONS OF IRAS 19200+3457

In 2001, we began systematic photometric observations of IRAS 19200+3457 aimed at studying the possible variability of the star. Our measurements were made with a UBV photometer attached to the 60-cm Zeiss-1 telescope at the Crimean Station of the Sternberg Astronomical Institute (SAI). The comparison star was HD 181163 ($V = 8\overset{m}{.}35$, $B = 8\overset{m}{.}31$, $U = 8\overset{m}{.}13$; Deutschman *et al.* 1976). The measurement error was $\sim 0\overset{m}{.}010$ in all three bands.

We obtained 77 magnitude estimates for the star over three years of its observations. Table 1 presents our UBV observations, while Fig. 1 shows the UBV light curves of the star. The mean magnitude of IRAS 19200+3457 was $\langle U\rangle = 10\overset{m}{.}76$, $\langle B\rangle = 11\overset{m}{.}45$,

*E-mail: vera@sai.msu.ru

1063-7737/04/3011-0779$26.00

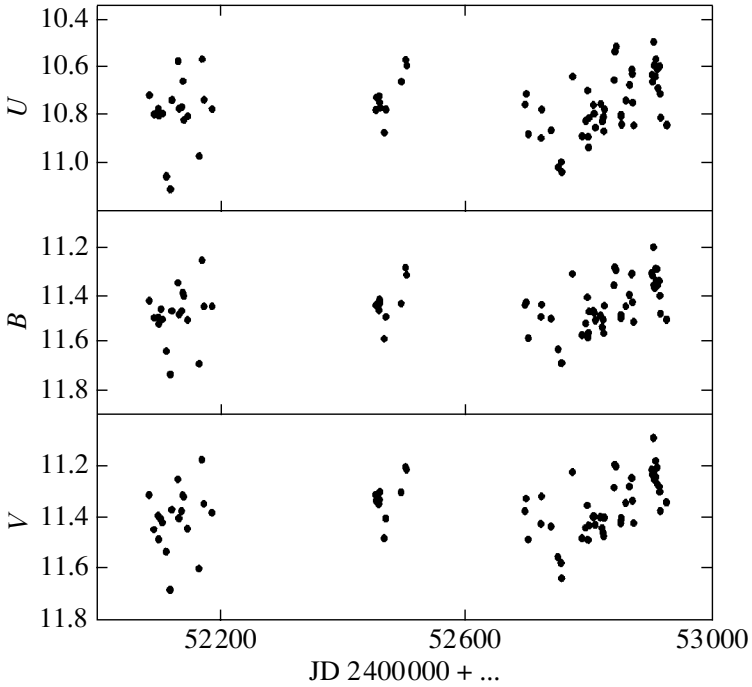

Fig. 1. Light curves of IRAS 19200+3457 in the period 2001–2003.

$\langle V \rangle = 11^m.36$. Over the observing period, the star exhibited rapid (on a time scale of several days) irregular brightness variations with maximum amplitudes of $\Delta V = 0^m.4$, $\Delta B = 0^m.4$, $\Delta U = 0^m.5$. Our search for periodicities revealed no statistically significant peaks in the periodogram. There is no color–magnitude correlation in the $(B-V)-V$ diagram (Fig. 2a), while a weak correlation between $(U-B)$ and V (Fig. 2b) is traceable.

UBV observations of IRAS 19200+3457 were also performed previously. In September 1973, Drilling (1975) obtained the following characteristics for the star: $V = 11^m.22$, $B-V = 0.14$, $U-B = -0.62$. According to the estimates of Gauba *et al.* (2003), the star in April 2000 had $V = 11^m.25$, $B-V = 0.10$, $U-B = -0.76$. In addition, the catalog of luminous stars (Stock *et al.* 1960) gives $m_{pg} = 11^m.4$ for LSII +34°1, which is almost equal to the current B magnitude of the star. The star's mean brightness appears to have changed only slightly over the last half a century.

The photometric variability of IRAS 19200+3457 bears a strong similarity to that of other hot post-AGB stars. As we reported previously (Arkhipova *et al.* 1996, 1998, 2001a, 2001b, 2002), the objects V886 Her, LSIV–12°111, and V1853 Cyg also exhibit rapid irregular photometric variability with amplitudes up to $0^m.3$ in V and no correlation between the $(B-V)$ color and the magnitude. As we suggested previously, a variable stellar wind is mainly responsible for the photometric variability of these stars, although rapid pulsations cannot be ruled out either.

EXTINCTION

Gauba *et al.* (2003) estimated the extinction for IRAS 19200+3457. These authors took the normal color index $(B-V)_0 = -0.20$ for Be stars, which corresponds to an effective temperature of 20 000 K. According to the observations by Gauba *et al.* (2003), IRAS 19200+3457 has $(B-V) = 0.1$ and, hence, $E(B-V) = 0.30$. These authors determined the interstellar extinction using maps from Schlegel *et al.* (1998). They estimated the interstellar component of $E(B-V)$ for IRAS 19200+3457 to be 0.14.

We also estimated the interstellar extinction toward IRAS 19200+3457. Using the SIMBAD database, we chose 23 stars with known spectral types and B and V magnitudes from a $1° \times 1°$ field around IRAS 19200+3457. The maximum color excess for them does not exceed 0.12.

Thus, the circumstellar component accounts for about half of the total extinction for IRAS 19200+3457. Similar results are also obtained for the other high-latitude hot post-AGB stars LSIV–12°111 and V886 Her (Arkhipova *et al.* 1998, 2002).

Table 1. *UBV* observations of IRAS 19200+3457

JD 2 400 000+	*U*	*B*	*V*	*U*−*B*	*B*−*V*	JD 2 400 000+	*U*	*B*	*V*	*U*−*B*	*B*−*V*
52 086	10.720	11.423	11.14	−0.703	0.109	52 790	10.891	11.568	11.482	−0.677	0.086
52 093	10.800	11.495	11.447	−0.695	0.048	52 796	10.827	11.519	11.441	−0.692	0.078
52 100	10.778	11.493	11.395	−0.715	0.098	52 798	10.701	11.409	11.355	−0.708	0.054
52 101	10.805	11.521	11.486	−0.716	0.035	52 799	10.893	11.579	11.487	−0.686	0.095
52 104	10.797	11.459	11.408	−0.662	0.051	52 800	10.938	11.558	11.489	−0.620	0.069
52 107	10.797	11.502	11.420	−0.705	0.082	52 801	10.814	11.469	11.431	−0.655	0.038
52 113	11.058	11.635	11.534	−0.577	0.101	52 808	10.761	11.466	11.398	−0.705	0.068
52 119	11.110	11.732	11.683	−0.622	0.049	52 809	10.797	11.472	11.397	−0.675	0.075
52 122	10.740	11.467	11.372	−0.727	0.095	52 811	10.855	11.506	11.429	−0.651	0.077
52 131	10.578	11.349	11.253	−0.771	0.096	52 820	10.757	11.485	11.400	−0.728	0.085
52 133	10.775	11.481	11.405	−0.706	0.076	52 823	10.829	11.534	11.441	−0.705	0.093
52 137	10.769	11.467	11.378	−0.699	0.090	52 824	10.811	11.503	11.461	−0.692	0.042
52 139	10.661	11.390	11.315	−0.729	0.075	52 825	10.870	11.560	11.473	−0.690	0.087
52 141	10.823	11.403	11.321	−0.580	0.082	52 826	10.780	11.444	11.402	−0.664	0.042
52 147	10.808	11.504	11.444	−0.696	0.060	52 841	10.657	11.359	11.286	−0.702	0.073
52 166	10.974	11.688	11.600	−0.714	0.088	52 842	10.538	11.285	11.196	−0.747	0.089
52 170	10.570	11.254	11.177	−0.684	0.077	52 844	10.518	11.296	11.203	−0.778	0.093
52 174	10.739	11.448	11.349	−0.709	0.099	52 852	10.805	11.490	11.418	−0.685	0.072
52 187	10.779	11.448	11.384	−0.669	0.064	52 853	10.842	11.484	11.403	−0.642	0.081
52 454	10.782	11.442	11.313	−0.660	0.129	52 860	10.742	11.446	11.346	−0.704	0.100
52 455	10.730	11.441	11.338	−0.711	0.103	52 866	10.677	11.399	11.282	−0.722	0.117
52 459	10.723	11.463	11.350	−0.740	0.113	52 869	10.614	11.312	11.247	−0.698	0.065
52 460	10.750	11.419	11.333	−0.669	0.086	52 870	10.631	11.310	11.249	−0.679	0.061
52 461	10.772	11.432	11.302	−0.660	0.130	52 871	10.751	11.430	11.337	−0.679	0.093
52 468	10.875	11.584	11.482	−0.709	0.100	52 873	10.845	11.512	11.422	−0.667	0.090
52 470	10.780	11.491	11.406	−0.711	0.085	52 902	10.636	11.308	11.217	−0.672	0.091
52 495	10.663	11.435	11.304	−0.772	0.131	52 903	10.665	11.316	11.236	−0.651	0.080
52 502	10.572	11.284	11.206	−0.712	0.078	52 905	10.498	11.200	11.091	−0.702	0.109
52 504	10.597	11.315	11.214	−0.718	0.101	52 906	10.596	11.359	11.231	−0.763	0.128
52 697	10.759	11.441	11.377	−0.682	0.064	52 907	10.642	11.370	11.255	−0.728	0.115
52 699	10.714	11.429	11.328	−0.715	0.101	52 908	10.570	11.289	11.181	−0.720	0.108
52 702	10.882	11.581	11.487	−0.699	0.094	52 909	10.606	11.341	11.246	−0.735	0.095
52 723	10.899	11.491	11.425	−0.592	0.066	52 911	10.612	11.291	11.208	−0.679	0.083
52 724	10.780	11.440	11.320	−0.660	0.120	52 912	10.691	11.360	11.274	−0.669	0.086
52 739	10.867	11.499	11.436	−0.632	0.063	52 914	10.600	11.341	11.282	−0.741	0.109
52 751	11.021	11.628	11.555	−0.607	0.073	52 915	10.715	11.402	11.303	−0.687	0.099
52 756	10.999	11.685	11.578	−0.686	0.107	52 916	10.815	11.478	11.378	−0.663	0.100
52 757	11.040	11.684	11.638	−0.644	0.046	52 926	10.844	11.503	11.344	−0.659	0.065
52 774	10.642	11.311	11.224	−0.669	0.087						

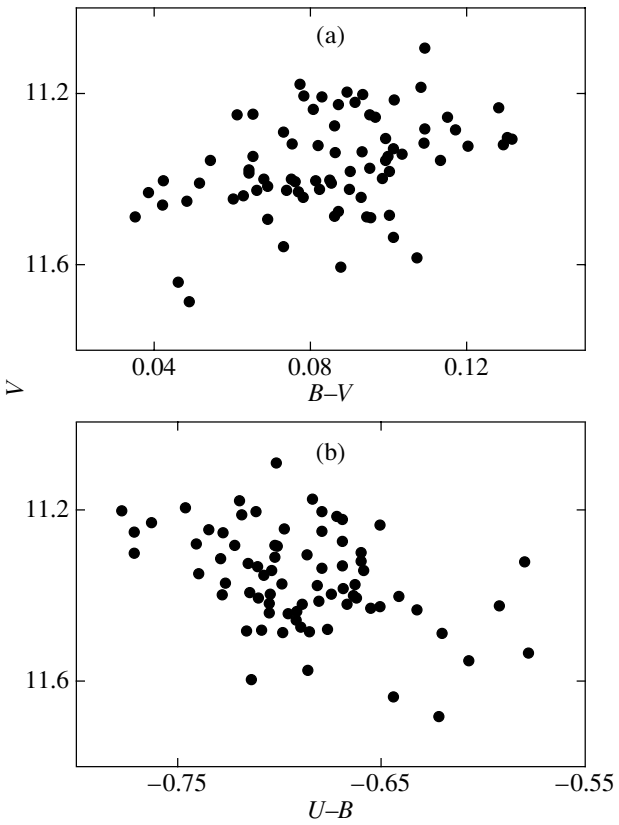

Fig. 2. Color–magnitude diagrams for IRAS 19200+3457.

SPECTROSCOPIC OBSERVATIONS OF IRAS 19200+3457

We took ten low-resolution spectrograms of IRAS 19200+3457 in the period 2001–2003. The observations were performed with a fast spectrograph attached to the 125-cm reflector at the Crimean Station of the SAI. The detector was a SBIG ST-6 274×375-pixel CCD array; it gave a resolution of 5.5 Å per pixel with a 600 lines mm^{-1} diffraction grating. A log of our observations is given in Table 2.

Table 2. Log of spectroscopic observations for IRAS 19200+3457

Date	Range, Å	Exposure time, s
Oct. 10, 2001	4000–5900, 5700–7600	1800, 1800
May 7, 2002	4000–5900, 5700–7600	1800, 600
Aug. 23, 2003	4000–5900, 5700–7600, 7300–9300	1800, 1800,1800
Aug. 24, 2003	4000–5900	1800
Sep. 24, 2003	4000–5900, 5700–7600	1800, 1200

Figure 3 shows a portion of the spectrum for IRAS 19200+3457 in the wavelength range λ4700–6800 Å. The standard star was 3 Vul (B9V), whose absolute spectral energy distribution is given in the paper by Voloshina *et al.* (1982).

The most prominent features in the spectrum of IRAS 19200+3457 are the strong Hα and Hβ emission lines. The HeI λ6678 Å and λ7065 Å lines and the infrared oxygen triplet, OI λ7774 Å, are in absorption. The HeI λ5876 Å line is observed in the wing of the blend containing the NaI D1 and D2 doublet lines. Part of the NaI doublet intensity originates in the circumstellar envelope, while the remaining part is of an interstellar origin. The spectrum also exhibits diffuse interstellar bands (DIBs), the strongest of which, λ5780 Å and λ6284 Å, are clearly seen.

The depths of HeI λ6678 Å and λ7065 Å lines vary in our spectrograms and correlate with the hydrogen line intensity (Fig. 4). The HeI lines probably contain variable emission components that are unresolvable in our spectra.

The typical full widths at half maximum of the Hα and Hβ emission lines in our spectra are FWHM $\sim$ 10 Å; they are essentially instrumental because of the low spectral resolution. We measured the equivalent widths of the Hα and Hβ lines; they vary within the ranges 19.3–26.1 and 1.7–2.8 Å, respectively. The error in the equivalent widths is $\sim 10\%$. Since the ranges of the $W(\mathrm{H}\alpha)$ and $W(\mathrm{H}\beta)$ variations exceed 3σ, we consider them to be real. The HI and HeI line profiles were also found to be variable for other hot post-AGB stars: V1853 Cyg and V886 Her (Smith and Lambert 1994; Arkhipova *et al.* 2001b).

We measured the equivalent width of the OI λ7774 Å triplet, $W(\mathrm{OI}) = 1.2$ Å, in the spectrogram taken on August 23, 2003. $W(\mathrm{OI})$ is known to be a good indicator of the stellar luminosity (Keenan and Hynek 1950). $W(\mathrm{OI}) = 1.2$ Å is the maximum value for B stars and indicates that the luminosity of IRAS 19200+3457 is high.

The spectral energy distribution of the object under study corrected for the extinction with the color excess $E(B-V) = 0.3$ (Gauba *et al.* 2003) corresponds to an early B star.

In the *Catalog of Luminous Stars* (Stock *et al.* 1960), LSII +34°1 is classified as OB+. Gauba *et al.* (2003) adopted the spectral type B for this star. Our low-resolution spectroscopy suggests only that IRAS 19200+3457 is an early B star with hydrogen emission lines in its spectrum. High-resolution spectroscopy is required to determine the chemical

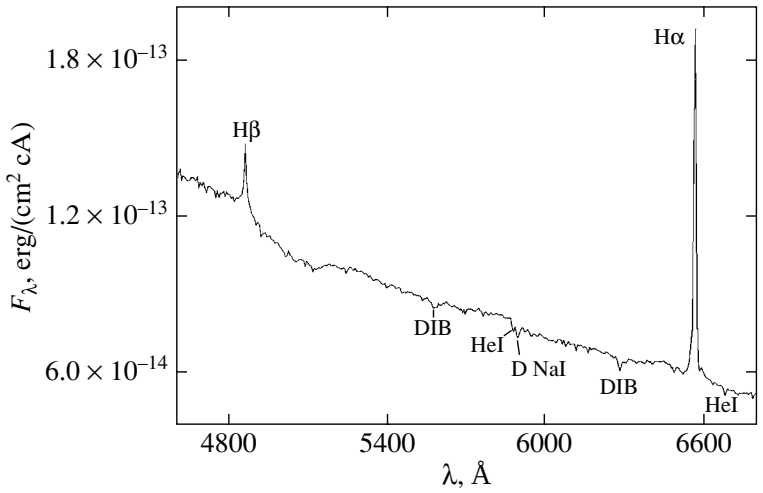

Fig. 3. Absolute spectral energy distribution for IRAS 19200+3457 in the wavelength range λ4600–6800 Å obtained on October 10, 2001.

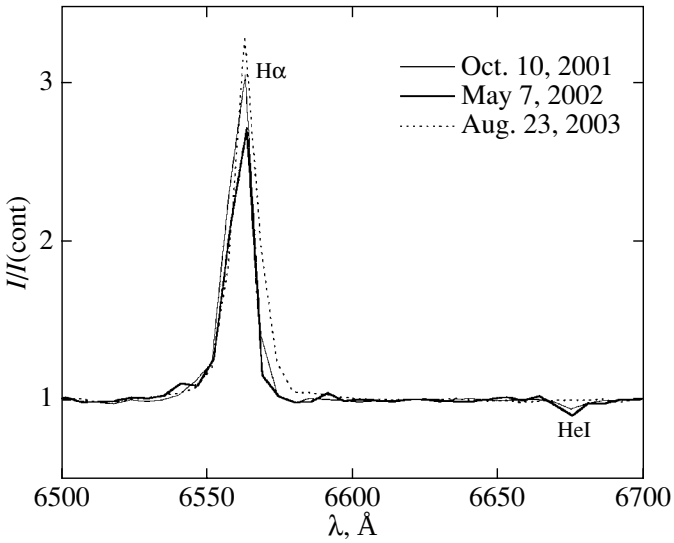

Fig. 4. Spectrum of IRAS 19200+3457 in the wavelength range λ6500–6700 Å.

composition of the star to refine its evolutionary status and to study the variability pattern of its line profiles.

CONCLUSIONS

Our UBV observations of the supergiant with an infrared excess IRAS 19200+3457 during 77 nights in the period 2001–2003 revealed rapid irregular brightness variations with a total amplitude up to $0^m.4$ in V.

Our spectroscopic observations of IRAS 19200+3457 in the period 2001–2003 showed that the star has an early-B-subtype spectrum with hydrogen emission lines. We found appreciable variability of the Hα and Hβ hydrogen emission lines and, probably, the He I λ6678 and λ7065 Å lines. The significant depth of the OI λ7774 Å oxygen infrared triplet confirms that IRAS 19200+3457 is a supergiant.

A similar pattern of photometric variability for IRAS 19200+3457 and three other hot post-AGB stars—V886 Her, V1853 Cyg, and LSIV–12°111—is an additional argument that all these stars are related objects.

A comparison of the currently available photometry and spectroscopy for IRAS 19200+3457 with previous observations leads us to conclude that the star's mean brightness and spectral type appear to have not changed over the last several decades. Since the

star has not shown any rapid evolutionary changes, it may be considered to be an intermediate-mass ($M \sim 0.6 M_\odot$) protoplanetary object.

ACKNOWLEDGMENTS

Our program of studying the variability and evolution of post-AGB stars is supported by the Russian Foundation for Basic Research (project no. 01-02-16530).

REFERENCES

1. V. P. Arkhipova, Pis'ma Astron. Zh. **15**, 925 (1989) [Sov. Astron. Lett. **15**, 400 (1989)].
2. V. P. Arkhipova and N. P. Ikonnikova, Pis'ma Astron. Zh. **18**, 1018 (1992) [Sov. Astron. Lett. **18**, 418 (1992)].
3. V. P. Arkhipova, N. P. Ikonnikova, V. F. Esipov, and R. I. Noskova, Pis'ma Astron. Zh. **22**, 526 (1996) [Astron. Lett. **22**, 470 (1996)].
4. V. P. Arkhipova, N. P. Ikonnikova, R. I. Noskova, *et al.,* Pis'ma Astron. Zh. **25**, 30 (1999) [Astron. Lett. **25**, 25 (1999)].
5. V. P. Arkhipova, N. P. Ikonnikova, R. I. Noskova, *et al.,* Astron. Zh. **27**, 841 (2001) [Astron. Lett. **27**, 719 (2001)].
6. V. P. Arkhipova, N. P. Ikonnikova, R. I. Noskova, and G. V. Komissarova, Pis'ma Astron. Zh. **28**, 298 (2002) [Astron. Lett. **28**, 257 (2002)].
7. V. P. Arkhipova, V. G. Klochkova, and G. V. Sokol, Pis'ma Astron. Zh. **27**, 122 (2001) [Astron. Lett. **27**, 99 (2001)].
8. W. A. Deutschman, R. J. Davis, and R. E. Schild, Astrophys. J., Suppl. Ser. **30**, 97 (1976).
9. J. S. Drilling, Astron. J. **80**, 128 (1975).
10. G. Gauba, M. Parthasarathy, Kumar Brijesh, *et al.*, Astron. Astrophys. **404**, 305 (2003).
11. P. C. Keenan and J. A. Hynek, Astrophys. J. **111**, 1 (1950).
12. A. Preite-Martinez, Astron. Astrophys., Suppl. Ser. **76**, 317 (1988).
13. D. J. Schlegel, D. P. Finkbeiner, and M. Davis, Astrophys. J. **500**, 525 (1998).
14. V. V. Smith and D. L. Lambert, Astrophys. J. **424**, L123 (1994).
15. C. B. Stephenson, Astrophys. J. **300**, 779 (1986).
16. J. Stok, J. J. Nassau, and C. B. Stephenson, Hamburger Sternw. Warner and Swasey Observ. **2** (1960).
17. I. B. Voloshina, I. N. Glushneva, and V. T. Doroshenko, *Spectrophotometry of Bright Stars* (Nauka, Moscow, 1982) [in Russian].

Translated by N. Samus'

Astronomy Letters, Vol. 30, No. 11, 2004, pp. 785–796. Translated from Pis'ma v Astronomicheskiĭ Zhurnal, Vol. 30, No. 11, 2004, pp. 861–873.

Kinematic Peculiarities of Gould Belt Stars

V. V. Bobylev*

Pulkovo Astronomical Observatory, Russian Academy of Sciences,
Pulkovskoe shosse 65, St. Petersburg, 196140 Russia

Received November 12, 2004

Abstract—We analyzed the space velocities of Gould Belt stars younger than 125 Myr located at heliocentric distances < 650 pc. We determined the rotation and expansion parameters of the Gould Belt by assuming the existence of a single kinematic center whose direction was found to be the following: $l_o = 128^\circ$ and $R_o = 150$ pc. The linear velocities reach their maximum at a distance of $\approx$300 pc from the center and are -6 km s^{-1} for the rotation (whose direction coincides with the Galactic rotation) and $+4$ km s^{-1} for the expansion. The stellar rotation model used here is shown to give a more faithful description of the observed velocity field than the linear model based on the Oort constants A_G and B_G. We present evidence that the young clusters β Pic, Tuc/HorA, and TWA belong to the Gould Belt structure.

Key words: *Gould Belt, Galaxy (Milky Way), OB associations, TW Hydrae, β Pictoris, Tucana.*

INTRODUCTION

The star-and-gas complexes associated with star-formation processes in our Galaxy and in other galaxies have a hierarchical structure (Efremov 1998; Efremov and Elmegreen 1998). Giant star-and-gas (GSG) complexes trace the spiral pattern of the Galaxy (Efremov 1998). The GSG complexes have masses of $\approx 1\times10^6\ M_\odot$, sizes as large as 1000 pc, and lifetimes $\tau < 10^8$ yr. Less massive structures, such as OB associations, open star clusters, and giant molecular clouds, are part of a GSG complex. The Sun lies within a GSG complex that is known as the Gould Belt (with a radius of $\approx$500 pc and a lifetime of $\tau \approx 60 \times 10^6$ yr). In turn, the Gould Belt is part of an older ($\tau \approx 5 \times 10^8$ yr) and more massive ($\approx 2\times10^7\ M_\odot$) structure about 1000 pc in size that is known as the Local (Orion) Arm or the Local system of stars perceived as a gravitationally bound, long-lived system. Its kinematics suggests that it is associated (Olano 2001) with the Sirius star supercluster (Eggen 1984, 1992). Since the mean residual velocity of the Sirius supercluster stars relative to the local standard of rest (LSR) is low, the center of mass of the Local system of stars has made several turns around the Galactic center in a nearly circular orbit. Over its lifetime, the Gould Belt has probably experienced a single impact from a spiral density wave.

An important indicator of the stability of such a system as the Gould Belt is the existence of proper rotation. Such rotation is reliably found from observations of Gould Belt stars (Lindblad 2000; Bobylev 2004). Over its lifetime, the Gould Belt has been affected by the shock wave generated by a spiral density wave at least once. An analysis of the motions of the OB associations that fill the interarm space ($r \leq 3$ kpc) reveals a complex periodic structure of their residual velocities attributable to the influence of spiral density waves (Mel'nik *et al.* 2001; Zabolotskikh *et al.* 2002; Mel'nik 2003). One of these features is the prominent structure in the radial residual velocity distribution in Galactocentric distance in the Gould Belt region (see Fig. 3a in Mel'nik *et al.* 2001) that we associate with the well-known positive K-effect or with the expansion of young stars. In this paper, based on a sample of individual stars that are members of OB associations, we study this effect in detail.

The goal of this work is to study the motion of the Gould Belt using data on stars with reliable age estimates. For this purpose, we use young and near-by OB associations with age estimates obtained by different authors on the basis of currently available observations and methods. The rotation and expansion parameters of the Gould Belt are determined by assuming the existence of a single kinematic center. To this end, we use Bottlinger's formulas in a form that allows the direction of the single kinematic center to be analytically determined simultaneously with the rotation and expansion–contraction parameters.

*E-mail: vbobylev@gao.spb.ru

METHODS OF ANALYSIS

Bottlinger's Formulas

In this paper, we use a rectangular Galactic coordinate system with the axes directed away from the observer toward the Galactic center ($l = 0°$, $b = 0°$, the X axis), along the Galactic rotation ($l = 90°$, $b = 0°$, the Y axis), and toward the North Galactic Pole ($b = 90°$, the Z axis). We derived the basic equations from Bottlinger's standard formulas (Ogorodnikov 1965). By assuming the existence of a single kinematic center of rotation and expansion–contraction (l_o, R_o), we transformed the formulas to

$$\begin{aligned} V_r &= u_G \cos b \cos l + v_G \cos b \sin l + w_G \sin b \quad (1)\\ &- D_1(R - R_o)\sin(l - l_o)\cos b - D_2(R - R_o)\\ &\times \cos(l - l_o)\cos b - F_1(R - R_o)^2 \sin(l - l_o)\cos b\\ &- F_2(R - R_o)^2 \cos(l - l_o)\cos b + k_o r \cos^2 b\\ &+ k'_o r(R - R_o)\cos^2 b + 0.5k''_o r(R - R_o)^2 \cos^2 b, \end{aligned}$$

$$\begin{aligned} 4.74 r\mu_l \cos b &= -u_G \sin l + v_G \cos l\\ &+ \omega_o r \cos b + \omega'_o r(R - R_o)\cos b + 0.5\omega''_o r\\ &\times \cos b(R - R_o)^2 - D_1(R - R_o)\cos(l - l_o)\\ &+ D_2(R - R_o)\sin(l - l_o) - F_1(R - R_o)^2\\ &\times \cos(l - l_o) + F_2(R - R_o)^2 \sin(l - l_o), \end{aligned}$$

$$\begin{aligned} 4.74 r\mu_b &= -u_G \cos l \sin b - v_G \sin l \sin b\\ &+ w_G \cos b + D_1(R - R_o)\sin(l - l_o)\sin b\\ &+ D_2(R - R_o)\cos(l - l_o)\sin b + F_1(R - R_o)^2\\ &\times \sin(l - l_o)\sin b + F_2(R - R_o)^2 \cos(l - l_o)\sin b\\ &- k_o r \cos b \sin b - k'_o r(R - R_o)\cos b \sin b\\ &- 0.5k''_o r(R - R_o)^2 \cos b \sin b. \end{aligned}$$

Here, the coefficient 4.74 is the quotient of the number of kilometers in an astronomical unit by the number of seconds in a tropical year, $r = 1/\pi$ is the heliocentric distance of the star, R_o is the distance from the Sun to the kinematic center, and R is the distance from the star to the kinematic center. Since we corrected the observed motions for the peculiar solar motion with respect to the LSR (Dehnen and Binney 1998), the quantities u_G, v_G, and w_G are (in contrast to the standard approach, we reversed the signs) the velocity components of the centroid of the stars under consideration with respect to the LSR; the components of the stellar proper motion $\mu_l \cos b$ and μ_b are in mas yr^{-1} (milliarcseconds per year), the radial velocity V_r is in km s^{-1}, the parallax π is in mas (milliarcseconds), and the distances R, R_o, and r are in kpc. The quantity ω_o is the angular velocity of the stellar system at distance R_o; k_o is the radial expansion (or contraction) rate of the stellar system at distance R_o; ω'_o, ω''_o and k'_o, k''_o are the corresponding derivatives with respect to the heliocentric distance taken at distance R_o; and l_o is the direction of the kinematic center. R can be calculated using the expression

$$R^2 = (r\cos b)^2 - 2R_o r \cos b \cos(l - l_o) + R_o^2. \quad (2)$$

In Eqs. (1), we use the unknowns

$$\begin{aligned} D_1 &= D\cos l_\theta, \quad D_2 = -D\sin l_\theta, \quad (3)\\ F_1 &= F\cos l_\theta, \quad F_2 = -F\sin l_\theta, \end{aligned}$$

where $D = \sqrt{D_1^2 + D_2^2} = \omega'_o R_o$ and $F = \sqrt{F_1^2 + F_2^2} = 0.5\omega''_o R_o$. Based on relations (3), we determine the correction l_θ to the assumed value of l_o twice:

$$\tan(l_\theta)_D = -D_2/D_1, \quad \tan(l_\theta)_F = -F_2/F_1; \quad (4)$$

in this case, the new direction is $l_o + l_\theta$. On the other hand, we may introduce similar quantities, $G = k'_o R_o$ and $H = 0.5k''_o R_o$, with the unknowns G_1, G_2, H_1, and H_2 for the expansion to obtain

$$\begin{aligned} G_1 &= G\cos l_R = -G\sin l_\theta, \quad (5)\\ G_2 &= -G\sin l_R = G\cos l_\theta,\\ H_1 &= H\cos l_R = -H\sin l_\theta,\\ H_2 &= -H\sin l_R = H\cos l_\theta. \end{aligned}$$

The orthogonality of the expansion and rotation effects ($l_\theta = l_R + 90°$) is reflected in relations (5); as a result, the unknowns in Eqs. (1) cannot be separated. Therefore, to determine the direction of the kinematic center, it will suffice to use one of the sets of unknowns, for example, D_1, D_2, F_1, and F_2, in Eqs. (1). Based on the described approach, we can independently estimate the distance from the Sun to the kinematic center. This estimate can be obtained from the formulas that follow from relations (3)–(5):

$$\begin{aligned} D &= R_o|\omega'_o - k'_o|, \quad (6)\\ F &= 0.5R_o|\omega''_o - k''_o|. \end{aligned}$$

Equations (1) contain thirteen sought unknowns: u_G, v_G, w_G, ω_o, ω'_o, ω''_o, k_o, k'_o, k''_o, D_1, D_2, F_1, and F_2, which can be determined by the least-squares method. If the direction of the kinematic center is known, then the equations have the original form

$$\begin{aligned} V_r &= u_G \cos b \cos l + v_G \cos b \sin l + w_G \sin b \quad (7)\\ &- R_o(R - R_o)\sin(l - l_o)\cos b\omega'_o\\ &- 0.5R_o(R - R_o)^2 \sin(l - l_o)\cos b\omega''_o + \cos^2 b k_o r\\ &+ (R - R_o)[r\cos b - R_o\cos(l - l_o)]\cos b k'_o\\ &+ 0.5(R - R_o)^2[r\cos b - R_o\cos(l - l_o)]\cos b k''_o, \end{aligned}$$

$$\begin{aligned} 4.74 r\mu_l \cos b &= -u_G \sin l + v_G \cos l\\ &- (R - R_o)(R_o\cos(l - l_o) - r\cos b)\omega'_o \end{aligned}$$

$$-0.5(R-R_\odot)^2(R_\odot\cos(l-l_\odot)-r\cos b)\omega''_\odot + r\cos b\omega_\odot + R_\odot(R-R_\odot)\sin(l-l_\odot))k'_\odot + 0.5R_\odot(R-R_\odot)^2\sin(l-l_\odot))k''_\odot,$$

$$4.74r\mu_b = -u_G\cos l\sin b - v_G\sin l\sin b + w_G\cos b + R_\odot(R-R_\odot)\sin(l-l_\odot)\sin b\omega'_\odot + 0.5R_\odot(R-R_\odot)^2\sin(l-l_\odot)\sin b\omega''_\odot - \cos b\sin bk_\odot r - (R-R_\odot)[r\cos b - R_\odot\cos(l-l_\odot)]\sin bk'_\odot - 0.5(R-R_\odot)^2\times[r\cos b - R_\odot\cos(l-l_\odot)]\sin bk''_\odot.$$

These equations contain nine sought unknowns: u_G, v_G, w_G, $\omega_\odot$, $\omega'_\odot$, $\omega''_\odot$, $k_\odot$, $k'_\odot$, and $k''_\odot$.

A peculiarity of this method is that it requires the existence of derivatives only with respect to the distance. A sample of stars uniformly distributed even in one Galactic quadrant can satisfy this requirement.

The Statistical Method

We use the standard statistical method (Trümpler and Weaver 1953; Parenago 1954; Ogorodnikov 1965) that consists in determining and analyzing the symmetric moment tensor or the stellar residual velocity dispersion tensor. When both the radial velocities and proper motions of stars are used to determine the six unknown components of the dispersion tensor, we have six equations that can be written for each star. The semiaxes of the residual velocity (Schwarzschild) ellipsoid that we denote by $\sigma_{1,2,3}$ can be determined by analyzing the eigenvalues of the dispersion tensor. We denote the directions of the principal axes of this ellipsoid by $l_{1,2,3}$ and $b_{1,2,3}$. A peculiarity of the approach used here is that the stellar velocities corrected for the peculiar solar motion with respect to the LSR and for the general Galactic rotation are used as the residual velocities.

The Ogorodnikov–Milne Model

In the linear Ogorodnikov–Milne model, we use the same notation that was introduced by Clube (1972, 1973) and used by du Mont (1977, 1978). We modify the linear model developed to describe the general Galactic rotation to describe the peculiarities of the velocity field of nearby stars. To within terms of the first order of smallness $r/R_\odot \ll 1$, the observed velocity $\mathbf{V}(r)$ of a star with a heliocentric radius vector $\mathbf{r}$ is described by the vector equation

$$\mathbf{V}(r) - \mathbf{V}_{GR} - \mathbf{V}_{\odot LSR} = \mathbf{V}_G + M\mathbf{r} + \mathbf{V}'. \quad (8)$$

Here, $\mathbf{V}_{GR}$ is the systematic velocity of the star attributable to the general Galactic rotation, $\mathbf{V}_{\odot LSR}$ is the peculiar solar motion with respect to the LSR, $\mathbf{V}_G(u_G, v_G, w_G)$ is the velocity of the centroid of the stars under consideration relative to the LSR, $\mathbf{V}'$ is the residual stellar velocity (the residual stellar velocities are assumed to be distributed randomly), and M is the displacement matrix that describes systematic motions similar to the proper rotation and expansion–contraction effects. The components of the matrix M are the partial derivatives of $\mathbf{u}(u_1, u_2, u_3)$ with respect to $\mathbf{r}(r_1, r_2, r_3)$:

$$M_{pq} = \left(\frac{\partial u_p}{\partial r_q}\right)_\odot, \quad p, q = 1, 2, 3. \quad (9)$$

The matrix M can be separated into symmetric, M^+, and antisymmetric, M^-, parts. Following Ogorodnikov (1965), we call them the local deformation and local rotation tensors, respectively:

$$M^+_{pq} = \frac{1}{2}\left(\frac{\partial u_p}{\partial r_q} + \frac{\partial u_q}{\partial r_p}\right)_\odot, \quad (10)$$

$$M^-_{pq} = \frac{1}{2}\left(\frac{\partial u_p}{\partial r_q} - \frac{\partial u_q}{\partial r_p}\right)_\odot, \quad (p, q = 1, 2, 3).$$

The basic equations are

$$V_r = u_G\cos b\cos l + v_G\cos b\sin l + w_G\sin b + r(\cos^2 b\cos^2 lM_{11} + \cos^2 b\cos l\sin lM_{12} + \cos b\sin b\cos lM_{13} + \cos^2 b\sin l\cos lM_{21} + \cos^2 b\sin^2 lM_{22} + \cos b\sin b\sin lM_{23} + \sin b\cos b\cos lM_{31} + \cos b\sin b\sin lM_{32} + \sin^2 bM_{33}), \quad (11)$$

$$4.74r\mu_l\cos b = -u_G\sin l + v_G\cos l + r(-\cos b\cos l\sin lM_{11} - \cos b\sin^2 lM_{12} - \sin b\sin lM_{13} + \cos b\cos^2 lM_{21} + \cos b\sin l\cos lM_{22} + \sin b\cos lM_{23}),$$

$$4.74r\mu_b = -u_G\cos l\sin b - v_G\sin l\sin b + w_G\cos b + r(-\sin b\cos b\cos^2 lM_{11} - \sin b\cos b\sin l\cos lM_{12} - \sin^2 b\cos lM_{13} - \sin b\cos b\sin l\cos lM_{21} - \sin b\cos b\sin^2 lM_{22} - \sin^2 b\sin lM_{23} + \cos^2 b\cos lM_{31} + \cos^2 b\sin lM_{32} + \sin b\cos bM_{33}),$$

where the stellar velocity components corrected for the general Galactic rotation and for the peculiar solar motion with respect to the LSR appear on the left-hand sides. Equations (11) contain twelve sought unknowns: the three velocity components

$\mathbf{V}_G(u_G, v_G, w_G)$ and the nine components M_{pg} that can be determined by the least-squares method. The deformation and rotation tensor components can be calculated using the values of M_{pq} derived from relations (10).

This method requires the existence of all derivatives with respect to the coordinates. A sample of stars that densely fill each coordinate axis is needed to meet this requirement.

OBSERVATIONAL MATERIAL

Data on Stars

We compiled our working list of stars located no farther than ≈ 650 pc from the Sun using the following sources: we took the Hipparcos (ESA 1997) star numbers for the Col 121, Per OB2, Vel OB2, Tr 10, LCC, UCL, US, Cep OB2, Lac OB1, Cep OB6, α Per (Per OB3), and Cas Tau associations from de Zeeuw *et al.* (1999); for the Ori OB1 a–d associations from Brown *et al.* (1994); for the IC 2391, IC 2602, NGC 2232, NGC 2451, NGC 2516, NGC 2547, and Pleiades clusters from the list by Robichon *et al.* (1999); the list of members of the TW Hydrae (TWA), β Pic, and Tucana/HorA associations from Song *et al.* (2003); and for the a Car cluster from Platais *et al.* (1998). The data on 24 stars having X-ray emissions and located no farther than 50 pc from the Sun were taken from Makarov (2003), where they are denoted as an XY sample. The star HIP 30030 in Makarov's list is a member of the TWA cluster, belongs to the Tucana/HorA group, and is designated TWA42 (Song *et al.* 2003). The data on 34 stars located no farther than 100 pc from the Sun were taken from Wichmann *et al.* (2000, 2003). Four stars were not included in other lists; we placed them in group 2. Table 1 gives the ages of the selected clusters. We took the equatorial coordinates, parallaxes, and proper motions from the Hipparcos catalog and the radial velocities from the catalog by Barbier-Brossat and Figon (2000). We use only single stars (the astrometric orbital binaries marked by the symbol O were rejected) for which the parallaxes, radial velocities, and proper motions are available. Based on the stellar ages (Table 1), we divided the stars into three groups: (1) the youngest stars with ages <10 Myr (group 1); (2) the stars with middle ages of 10–60 Myr (group 2); and (3) the old stars with ages of 60–125 Myr (group 3).

Allowance for the Galactic Rotation

We took into account the general Galactic rotation using the parameters found previously (Bobylev 2004): $\omega_o = -28.0 \pm 0.6$ km s^{-1} kpc^{-1}, $\omega'_o = +4.17 \pm 0.14$ km s^{-1} kpc^{-2}, and $\omega''_o = -0.81 \pm 0.12$ km s^{-1} kpc^{-3}. The Galactocentric distance of the Sun was assumed to be $R_o = 7.1$ kpc, which corresponds to the short distance scale (Dambis *et al.* 2001).

The radial velocities and proper motions of the stars were corrected for peculiar solar motion with respect to the LSR using the values obtained by Dehnen and Binney (1998): $(u_\odot, v_\odot, w_\odot) = (10.0, 5.3, 7.2)$ km s^{-1}.

RESULTS

A preliminary analysis of the stellar space velocities showed the necessity of setting a limit on the total stellar velocity, $\sqrt{U^2 + V^2 + W^2} < 30$ km s^{-1}, which we use below. The residual velocities U, V, and W were calculated from standard formulas (Kulikovskii 1985). We used stars with parallaxes $\pi > 1.5$ mas ($r < 667$ pc). The number of stars used is given in the last column of Table 1. Thus, each of groups 1, 2, and 3 always contains a fixed number of stars, 114, 342, and 150, respectively. For our sample of stars, the mean error in the parallax is 15–17%. The mean errors in the proper motion components of the stars $4.74r\mu_l \cos b$ and $4.74r\mu_b$, including the errors in the parallaxes, are ≈ 1 km s^{-1}. For ≈ 40% of the stars, there are no data on the errors in the radial velocities (Barbier-Brossat and Figon 2000); for stars with available information about the errors, the mean error is ≈ 3.5 km s^{-1}.

The group 1 stars are distributed exclusively in Galactic quadrant III. The group 2 stars fill the solar neighborhood within $r \approx 650$ pc of the Sun most uniformly. The group 3 stars densely fill a compact zone within $r \approx 50$ pc of the Sun in Galactic quadrant II. We also formed a combined group of young (<60 Myr) stars composed of the group 1 and group 2 stars. For the latter combined group, the application of all kinematic models proved to be possible.

As the first approximation for the direction of the kinematic center, we take $l_o = 160°$ and $R_o = 150$ pc (Bobylev 2004). Solving the system of equations (1) for the combined group of young stars (group 1 + group 2) yielded the following kinematic parameters of the linear motion of the stars: $(u_G, v_G, w_G) = (0.0 \pm 0.7, -12.3 \pm 0.7, 1.3 \pm 0.3)$ km s^{-1}. Consequently, the stars under consideration move with respect to the LSR at a velocity of $V_G = 12.3 \pm 0.7$ km s^{-1} in the direction $L_G = 270 \pm 3°$ and $B_G = 6 \pm 1°$. Further,

$$\omega_o = -32.4 \pm 3.8 \text{ km s}^{-1} \text{ kpc}^{-1}, \quad (12)$$
$$\omega'_o = +93.2 \pm 28.3 \text{ km s}^{-1} \text{ kpc}^{-2},$$
$$\omega''_o = -170.5 \pm 107.8 \text{ km s}^{-1} \text{ kpc}^{-3},$$

Table 1. Data on nearby clusters and OB associations

Cluster/association name	Age, Myr	Reference	N_*
Group 1			
Ori OB1a	11.4 ± 1.9	Brown *et al.* (1994)	29
Ori OB1b	1.7 ± 1.1	Brown *et al.* (1994)	20
Ori OB1c	4.6 ± 2	Brown *et al.* (1994)	25
Ori OB1d	<1	Brown *et al.* (1994)	3
Col 121	5	de Zeeuw *et al.* (1999)	20
TW Hydrae (TWA)	≤ 10	Song *et al.* (2003) (f)	17
Group 2			
Per OB2	2–15	Jiménez and Clausen (1994)	9
NGC 2232	30–60	Torra *et al.* (2000)	4
NGC 2451	50	Carrier *et al.* (1999) (c)	5
NGC 2516	30–60	Torra *et al.* (2000)	6
NGC 2547	30–40	Jeffries and Tolley (1998)	5
Vel OB2	20	de Zeeuw *et al.* (1999)	29
IC 2391	35–55	Montes *et al.* (2001) (d)	10
Tr 10	15–30	de Zeeuw *et al.* (1999) (c)	6
a Car	<60	Platais *et al.* (1998) (c)	4
IC 2602	30	Luhman (2001) (c, d, g)	8
LCC	16–20	Sartori *et al.* (2003) (a)	46
UCL	16–20	Sartori *et al.* (2003) (b)	67
US	8–10	Sartori *et al.* (2003)	44
Cep OB2	5–10	de Zeeuw *et al.* (1999)	16
Lac OB1	15–25	de Zeeuw *et al.* (1999)	29
β Pic	<30	Song *et al.* (2003)	8
Tucana/HorA	<30	Song *et al.* (2003) (h)	8
Макаров (XY)	<60	Makarov (2003)	24
Wichmann-1	<14	Wichmann *et al.* (2000)	2
Wichmann-2 (ZAMS)	$\ll 90$	Wichmann *et al.* (2003)	2
Group 3			
Cep OB6	≈ 50	de Zeeuw *et al.* (1999) (e)	10
α Per (Per OB3)	≈ 50	de Zeeuw *et al.* (1999)	46
Cas Tau	≈ 50	de Zeeuw *et al.* (1999) (e)	56
Pleiades	70–125	Soderblom *et al.* (1993)	14
Wichmann (PL)	≈ 100	Wichmann *et al.* (2003)	30

Note: (a) 17–20 Myr (Mamajek *et al.* 2002); (b) 15–22 Myr (Mamajek *et al.* 2002); (c) 30–60 Myr (Torra *et al.* 2000); (d) 30 Myr (Stauffer *et al.* 1997); (e) 50–60 Myr (Asiain *et al.* 1999); (f) 10 Myr (Luhman 2001); (g) 30 Myr (Randich *et al.* 1997); (h) 30^{+20}_{-5} Myr (Luhman 2001).

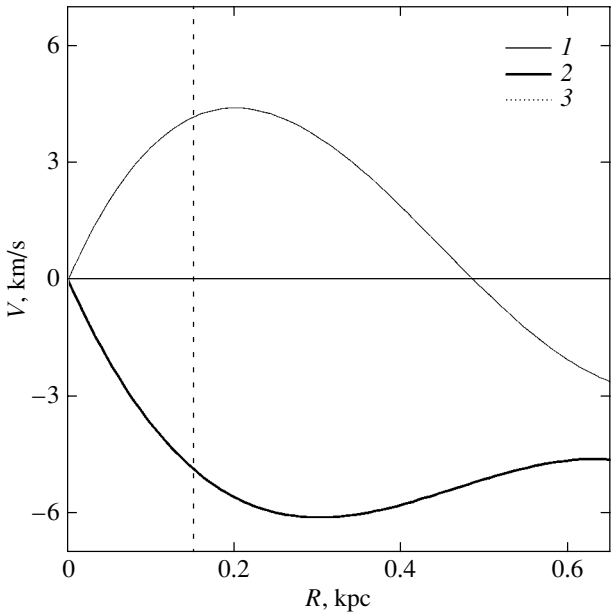

Fig. 1. Expansion (*1*) and rotation (*2*) curves of Gould Belt stars with ages ≤60 Myr (Group 1 + Group 2); the position of the Sun is marked (*3*). The parameters of the curves were obtained for the center with $l_o = 128^\circ$ and $R_o = 150$ pc.

$$k_o = +27.9 \pm 3.8 \text{ km s}^{-1} \text{ kpc}^{-1},$$
$$k'_o = -122.3 \pm 28.3 \text{ km s}^{-1} \text{ kpc}^{-2},$$
$$k''_o = +233.7 \pm 107.8 \text{ km s}^{-1} \text{ kpc}^{-3},$$
$$l_o = 128^\circ,$$
$$(l_\theta)_D = 2^\circ,$$
$$(l_\theta)_F = 181^\circ,$$
$$(R_o)_D = 180 \text{ pc},$$
$$(R_o)_F = 410 \text{ pc}.$$

The results of the solution of (12) are presented in Fig. 1, where line *1* indicates the derived expansion curve with the estimated parameters k_o, k'_o, and k''_o; line *2* indicates the rotation curve with the estimated parameters ω_o, ω'_o, and ω''_o. As we see from the solution of (12), the value of $R_o = 180$ pc calculated using the first derivatives is in satisfactory agreement with the $R_o = 150$ pc found previously (Bobylev 2004). The expansion curve constructed by solving (12) has a velocity maximum of $V = 4.4$ km s^{-1} at $R = 200$ pc from the center. Based on these data, we determined the time elapsed from the onset of expansion, $\tau = 44$ Myr, and it is in good agreement with the ages of the stars under consideration.

Applying the Ogorodnikov–Milne model (Eqs. (11)) to the combined group of young stars (group 1 + group 2), we found the following components of the tensors M, M^+, and M^- (km s^{-1} kpc^{-1}):

$$M = \begin{pmatrix} 13.0_{(3.3)} & 8.1_{(1.4)} & -4.4_{(8.6)} \\ -21.5_{(3.3)} & 2.9_{(1.4)} & -7.0_{(8.6)} \\ 4.6_{(3.3)} & 4.3_{(1.4)} & -18.8_{(8.6)} \end{pmatrix}, \quad (13)$$

$$M^+ = \begin{pmatrix} 13.0_{(3.3)} & -6.7_{(1.8)} & 0.1_{(4.6)} \\ -6.7_{(1.8)} & 2.9_{(1.4)} & -1.4_{(4.3)} \\ 0.1_{(4.6)} & -1.4_{(4.3)} & -18.8_{(8.6)} \end{pmatrix},$$

$$M^- = \begin{pmatrix} 0 & 14.8_{(1.8)} & -7.1_{(5.0)} \\ -14.8_{(1.8)} & 0 & -4.5_{(4.6)} \\ 4.5_{(4.6)} & 5.7_{(4.3)} & 0 \end{pmatrix}.$$

The Oort parameters are: $A_G = M^+_{21} = -6.7 \pm 1.8$ km s^{-1} kpc^{-1}, $B_G = M^-_{21} = -14.8 \pm 1.8$ km s^{-1} kpc^{-1}, $C_G = 0.5(M^+_{11} - M^+_{22}) = 5.1 \pm 1.8$ km s^{-1} kpc^{-1}, $K_G = 0.5(M^+_{11} + M^+_{22}) = 8.0 \pm 1.8$ km s^{-1} kpc^{-1}. In Eqs. (11), the X axis is directed toward the Galactic center ($l_o = 0^\circ$). The deformation tensor in the principal axes M^+_G is (km s^{-1} kpc^{-1}):

$$M^+_G = \begin{pmatrix} 16.4 & 0 & 0 \\ 0 & -0.4 & 0 \\ 0 & 0 & -18.9 \end{pmatrix};$$

the directions of the principal axes are

$$L_1 = 153.5^\circ \pm 0.2^\circ, \quad B_1 = -1.1^\circ \pm 0.0^\circ, \quad (14)$$
$$L_2 = 243^\circ \pm 10^\circ, \quad B_2 = 4^\circ \pm 8^\circ,$$
$$L_3 = 81^\circ \pm 10^\circ, \quad B_3 = 86^\circ \pm 11^\circ.$$

The vertex deviation in the XY plane that we determined from the formula $\tan 2l_{XY} = -C/A$ is $l_{XY} = 19^\circ \pm 6^\circ$ and indicates one of the directions of the rotation center; the other direction is $l = 109^\circ$ and is close to the direction of the kinematic center $l_o = 128^\circ$ that we found using Eqs. (1).

An analysis of the deformation tensor (19), (20) leads us to the important conclusion (which cannot be drawn from model (1)) that expansion takes place exclusively in the Galactic XY plane.

The results of applying the statistical method are given in Table 2. As we see from this table, the direction of the rotation center for the combined group of stars (Group 1 + Group 2) is determined accurately, $l_1 = 132.7^\circ \pm 0.4^\circ$. The first axis of the residual velocity ellipsoid (the vertex deviation) changes its direction with the age of the stars under consideration. This is consistent with the dynamic model of

Table 2. Principal semiaxes of the residual velocity ellipsoid $\sigma_{1,2,3}$ and their directions $l_{1,2,3}$, $b_{1,2,3}$

Group	Age, Myr	$\sigma_1, \sigma_2, \sigma_3$, km s^{-1}	l_1, l_2, l_3	b_1, b_2, b_3
1+2	<60	9.1 ± 1.9	$132.7° \pm 0.4°$	$-6.0° \pm 0.0°$
		6.8 ± 1.9	$225° \pm 27°$	$-19° \pm 4°$
		2.8 ± 1.9	$206° \pm 27°$	$70° \pm 3°$
1	<10	7.6 ± 2.3	$172° \pm 1°$	$-10° \pm 2°$
		7.2 ± 2.3	$263° \pm 42°$	$-2° \pm 6°$
		3.5 ± 2.2	$186° \pm 42°$	$80° \pm 6°$
2	10–60	9.4 ± 2.0	$131° \pm 1°$	$-7° \pm 1°$
		5.5 ± 2.0	$224° \pm 18°$	$-22° \pm 5°$
		2.7 ± 1.9	$205° \pm 18°$	$66° \pm 4°$
3	50–125	10.3 ± 2.3	$36° \pm 1°$	$4° \pm 0°$
		6.1 ± 2.3	$127° \pm 10°$	$17° \pm 4°$
		2.5 ± 2.3	$293° \pm 10°$	$73° \pm 5°$
β Pic + Tuc + TWA		5.6 ± 1.7	$47°$	$34°$
		3.5 ± 1.7	$126°$	$-16°$
		2.1 ± 1.6	$194°$	$51°$

Table 3. Kinematic parameters of the Gould Belt stars calculated from Eqs. (7) with the assumed $l_o = 128°$, $R_o = 150$ pc for group 1+2 and $l_o = 36°$, $R_o = 150$ pc for group 3

Group	Age, Myr	u_G, v_G, w_G	V_G, L_G, B_G	$\omega_o, \omega'_o, \omega''_o$	k_o, k'_o, k''_o
1+2	<60	1.1 ± 0.4	11.9 ± 0.4	-35.3 ± 3.6	12.1 ± 2.7
		-11.8 ± 0.4	$275° \pm 2°$	132.6 ± 25.7	-9.0 ± 13.2
		1.3 ± 0.3	$6° \pm 1°$	-292.5 ± 87.9	-47.6 ± 29.9
1+2	<60	2.3 ± 0.3	12.0 ± 0.4	-23.1 ± 2.2	14.0 ± 2.2
		-11.1 ± 0.3	$285° \pm 2°$	31.3 ± 6.5	-27.3 ± 6.5
		1.3 ± 0.3	$6° \pm 2°$	–	–
3	50–125	0.7 ± 0.8	11.2 ± 0.8	54.7 ± 9.2	-23.2 ± 9.2
		-11.2 ± 0.8	$273° \pm 4°$	-103.5 ± 42.6	123.4 ± 42.7
		-0.1 ± 0.5	$-1° \pm 2°$	–	–

Note: The linear velocities u_G, v_G, w_G, and V_G are in km s^{-1}; the angular velocities ω_o and k_o are in km s^{-1} kpc^{-1}; the derivatives ω'_o and k'_o are in km s^{-1} kpc^{-2}; and the derivatives ω''_o and k''_o are in km s^{-1} kpc^{-3}.

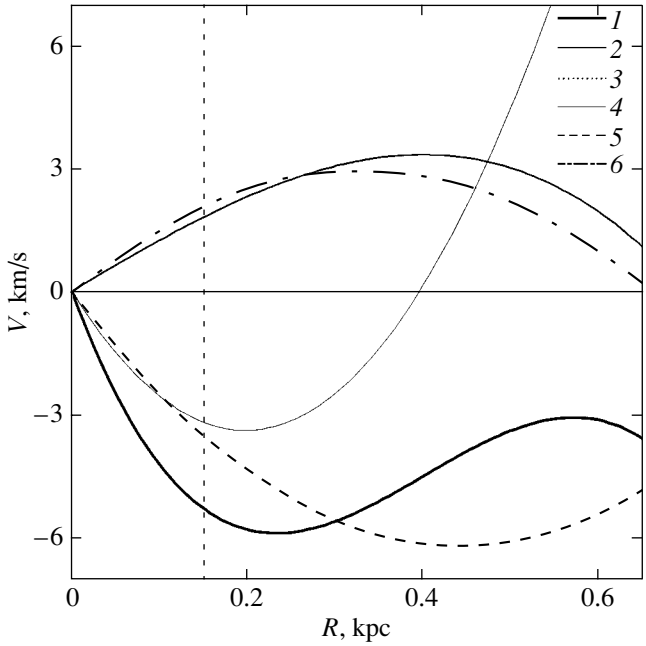

Fig. 2. Expansion (*2*, *6*) and rotation (*1*, *4*, *5*) curves of Gould Belt stars with ages <60 Myr (group 1 + group 2); the position of the Sun is marked (*3*). The parameters of the curves were obtained for the center with $l_o = 128^\circ$ and $R_o = 150$ pc.

Olano (2001). As Olano showed, the direction of the vertex rotation depends on the critical stellar density in the solar neighborhood ρ/ρ^*, where ρ is given in $M_\odot$ pc^{-3}. Following Olano's estimates ($\rho/\rho^* = 1.5$), we assume that the change occurs counterclockwise in the coordinate system under consideration. Thus, the vertex deviation changes from $l_1 = 36^\circ$ for the sample of old stars (Group 3) to $l_1 = 131^\circ$ for the sample of middle-aged stars (Group 2) and to $l_1 = 172^\circ$ for the sample of the youngest stars (Group 1). Associating this direction with the direction of the kinematic center, we can see that the center does not remain constant. Therefore, its independent determination is required for each sample of stars. There is good agreement of the orientation of the residual velocity tensor for the Group 1 and Group 2 stars that we found (Table 2) with the geometric characteristics of the Gould Belt (Torra *et al*. 2000). For example, for the group-2 stars, the directions $l_2 = 224^\circ \pm 18^\circ$ and $b_2 = -22^\circ \pm 5^\circ$ almost match the characteristics of the Gould Belt $\Omega_G = 275^\circ - 295^\circ$ and $i_G = 16^\circ - 20^\circ$ (here, Ω_G is the direction of the line of nodes of the Gould Belt and i_G is the inclination of the disk to the Galactic plane) found by Torra *et al*. (2000).

For the combined group of stars (Group 1 + Group 2), we obtained the solutions of Eqs. (7) in which we used $l_o = 128^\circ$ and $R_o = 150$ pc. Equations (7) were solved for two cases, with nine and seven unknowns in the first and second cases, by assuming that the second derivatives ω_o'' and k_o'' are equal to zero. The results are presented in Table 3 and Fig. 2. In Fig. 2, curves *1* and *2* were constructed using the data in the upper part of Table. 3; curves *5* and *6* were constructed using the data in the lower part of Table 3 (seven unknowns). Curve *4* in Fig. 2 represents the results of applying the Oort–Lindblad model, which for $l_o = 128^\circ$ are the following: $A_G = 6.5 \pm 1.8$ km s^{-1} kpc^{-1} and $B_G = -14.8 \pm 1.8$ km s^{-1} kpc^{-1} (these values were obtained from the equations of the Ogorodnikov–Milne model, but the curve is essentially the Oort–Lindblad approximation). The time elapsed from the onset of expansion for curves *2* and *6* is about $\tau = 120$ Myr, which significantly exceeds the estimate obtained by solving (12).

The results of solving Eqs. (7) for group 3 are given in the lower part of Table 3. The parameters derived for group 3 differ significantly from those of young stars: the rotation and the expansion have opposite signs. We associate the kinematic peculiarities of the Local system of stars that were found by Tsvetkov (1995a, 1995b, 1997) by studying type-A and-F stars with these stars. It is the influence of the Group 3 stars that led to the paradox that younger OB stars showed a slower rotation than older stars (Bobylev 2004).

Figures 3 and 4 show the residual velocities U, V, and W of middle-aged Gould Belt stars in projection onto the Galactic XY and XZ planes. These velocities are residual in every sense, because they were corrected from both the peculiar solar motion and the total velocity V_G that we found. Thus, we relate the

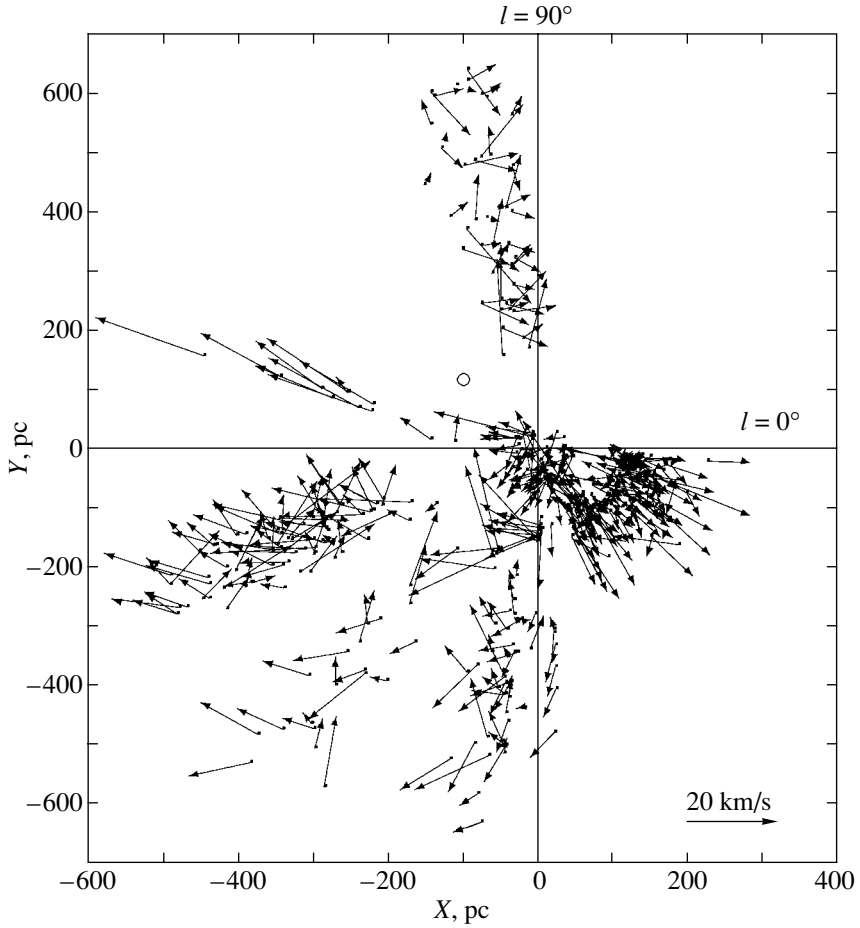

Fig. 3. Residual velocities U and V of Gould Belt stars with ages <60 Myr (Group 1 + Group 2) in projection onto the Galactic XY plane. The Sun is located at the coordinate origin. The circle marks the kinematic center with $l_\circ = 128^\circ$ and $R_\circ = 150$ pc.

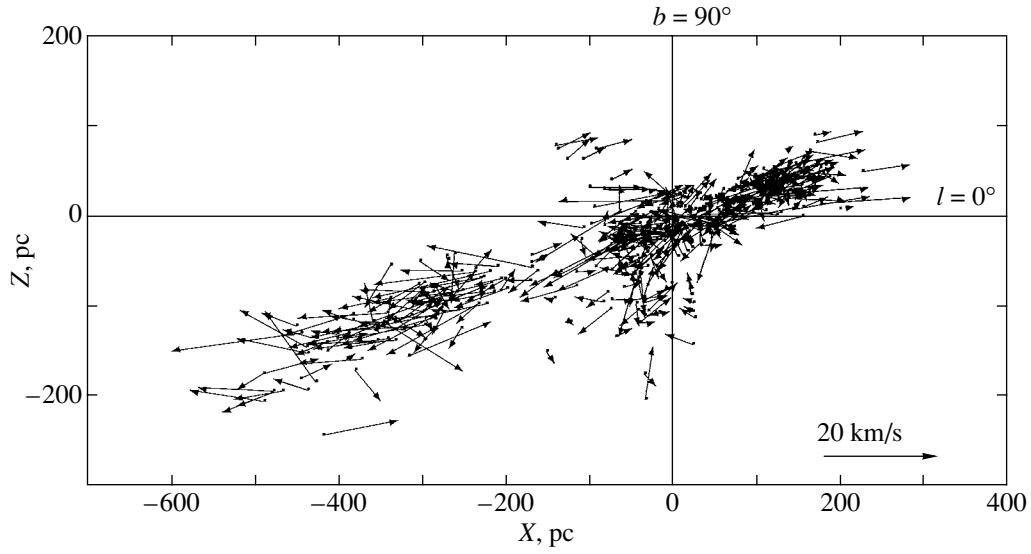

Fig. 4. Residual velocities U and W of Gould Belt stars with ages <60 Myr (Groups 1 and 2) in projection onto the Galactic XZ plane. The Sun is located at the coordinate origin.

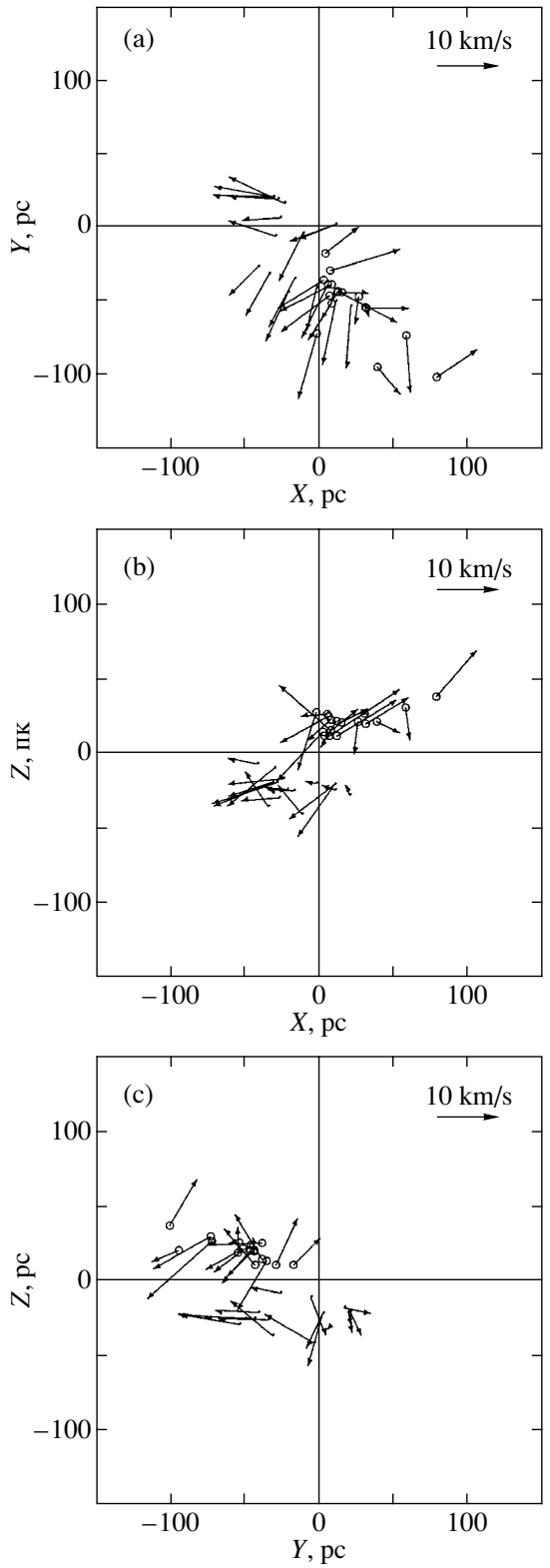

Fig. 5. Residual velocities of β Pic and Tuc/HorA cluster stars (the positions of the stars from both groups are indicated by the circles) together with TWA cluster stars: U and V in projection onto the Galactic XY plane (a); U and W in projection onto the Galactic XZ plane (b); V and W in projection onto the Galactic YZ plane (c).

velocities to a coordinate system whose center is the center of mass of the Gould Belt that moves with respect to the LSR.

Figure 5 shows the residual velocities of stars in the young β Pic and Tuc/HorA clusters together with TWA cluster stars.

DISCUSSION

The kinematic parameters that we derived using the linear Ogorodnikov–Milne model are in excellent agreement with the kinematic model of the Gould Belt suggested by Lindblad (2000), which is based on an analysis of the results by Comerón (1999) and Torra *et al.* (1997) for the age interval of Gould Belt stars 20–40 Myr. Lindblad's model assumes the proper rotation of the Gold Belt stars with an angular velocity of $\omega_G = B - A_\omega = -24\,\mathrm{km\,s^{-1}\,kpc^{-1}}$ ($A_\omega = 6.4$ km s^{-1} kpc^{-1} and $B = -17.4$ km s^{-1} kpc^{-1}) and the expansion with $K = 11.3$ km s^{-1} kpc^{-1} in the direction of the center $l_0 = 127°$. An analysis of the curves in Fig. 2 indicates that the linear model faithfully describes the observed velocity field of the stars under consideration no farther than 200–300 pc from the kinematic center.

Our rotation parameters for the Gould Belt are consistent with the model by Olano (2001) and with the evolution model of the youngest moving clusters by Asiain *et al.* (1999).

The question of whether the β Pic, Tuc/HorA, and TWA clusters belong to the Gould Belt structure is currently being debated. Makarov and Fabricius (2001) directly associate these clusters with the Gould Belt; Song *et al.* (2003) cast doubt on this association. In our opinion, a comparison of the stellar residual velocities for all of the clusters (β Pic, Tuc/HorA, and TWA) in Fig. 5 with our rotation and expansion curves suggests that the cluster stars belong to the Gould Belt structure. The last row in Table 2 gives our calculated parameters of the residual velocity ellipsoid for all 33 stars of the β Pic, Tuc/HorA, and TWA clusters. An analysis of l_1, b_1, l_2, b_2, l_3, b_3 and a comparison of Figs. 4 and 5 indicate that these stars belong to the disk of the Gould Belt. Ortega *et al.* (2002) performed model calculations of the orbits of β Pic cluster members in the Galactic field of attraction for an interval of 11.5 Myr and used them to determine the birthplace of the cluster. As follows from an analysis of our rotation curve for the Gould Belt (line *1* in Fig. 2), the Gould Belt has a substantial mass. Therefore, in our view, to determine the birthplaces of the β Pic, Tuc/HorA, and TWA clusters, the gravitational potential of the Gould Belt ($\approx 2\times10^6\ M_\odot$) or the entire Local system of stars ($\approx 2\times10^7\ M_\odot$) must be taken into account.

CONCLUSIONS

We have analyzed the residual velocity field of nearby and young Gould Belt stars by assuming the existence of a single kinematic center (the center of proper rotation and expansion). The direction of the kinematic center of the Gould Belt was found to be: $l_o = 128°$ and $R_o = 150$ pc.

Using the Ogorodnikov–Milne model, we showed that the vectors of the radial component of the residual velocity field (a positive K effect) lie in the Galactic XY plane unrelated to the plane of symmetry of the Gould Belt disk. This led us to conclude that the effect in question results from the impact of a spiral density wave propagating precisely through the Galactic disk on the cloud of gas out of which the stars under consideration were subsequently formed. In contrast, the effect of proper rotation is closely related to the plane of symmetry of the Gould Belt disk.

We have considered an approach that, in our view, allows the observed residual velocity field of the Gould Belt stars to be described more faithfully than does the linear (Oort–Lindblad) model. The linear velocities that we found for a sample of stars younger than 60 Myr reach their maximum at a distance of ≈ 300 pc from the kinematic center and are -6 km s^{-1} for the rotation and $+4$ km s^{-1} for the expansion. Our constructed proper rotation curve for the sample of young stars in the Gould Belt suggests that its mass is substantial. This conclusion is in agreement with the spatial distribution of faint stars with X-ray emission (Guillout *et al.* 1998).

We argue that the young β Pic, Tuc/HorA, and TWA clusters belong to the Gould Belt structure.

ACKNOWLEDGMENTS

I am grateful to A.T. Baikova for her help and useful discussions. This work was supported by the Russian Foundation for Basic Research (project no. 02-02-16570).

REFERENCES

1. R. Asiain, F. Figueras, and J. Torra, Astron. Astrophys. **350**, 434 (1999).
2. M. Barbier-Brossat and P. Figon, Astron. Astrophys., Suppl. Ser. **142**, 217 (2000).
3. V. V. Bobylev, Pis'ma Astron. Zh. **30**, 185 (2004) [Astron. Lett. **30**, 159 (2004)].
4. A. G. A. Brown, E. J. de Geus, and P. T. de Zeeuw, Astron. Astrophys. **289**, 101 (1994).
5. F. Carrier, G. Burki, and C. Richard, Astron. Astrophys. **341**, 469 (1999).
6. S. V. M. Clube, Mon. Not. R. Astron. Soc. **159**, 289 (1972).
7. S. V. M. Clube, Mon. Not. R. Astron. Soc. **161**, 445 (1973).
8. F. Comerón, Astron. Astrophys. **351**, 506 (1999).
9. A. K. Dambis, A. M. Mel'nik, and A. S. Rastorguev, Pis'ma Astron. Zh. **27**, 68 (2001) [Astron. Lett. **27**, 58 (2001)].
10. W. Dehnen and J. J. Binney, Mon. Not. R. Astron. Soc. **298**, 387 (1998).
11. P. T. de Zeeuw, R. Hoogerwerf, J. H. J. de Bruijne, *et al.*, Astron. J. **117**, 354 (1999).
12. B. du Mont, Astron. Astrophys. **61**, 127 (1977).
13. B. du Mont, Astron. Astrophys. **66**, 441 (1978).
14. Y. N. Efremov, Astron. Astrophys. Trans. **15**, 3 (1998).
15. Y. N. Efremov and B. G. Elmegreen, Mon. Not. R. Astron. Soc. **299**, 588 (1998).
16. O. J. Eggen, Astron. J. **89**, 1350 (1984).
17. O. J. Eggen, Astron. J. **104**, 1493 (1992).
18. A. Giménez and J. V. Clauzen, Astron. Astrophys. **291**, 795 (1994).
19. P. Guillout, M. F. Sterzik, J. H. M. M. Schmitt, *et al.*, Astron. Astrophys. **337**, 113 (1998).
20. R. D. Jeffries and A. J. Tolley, Mon. Not. R. Astron. Soc. **300**, 331 (1998).
21. P. G. Kulikovskiĭ, *Stellar Astronomy* (Nauka, Moscow, 1985) [in Russian].
22. K. L. Luhman, Astrophys. J. **560**, 287 (2001).
23. P. O. Lindblad, Astron. Astrophys. **363**, 154 (2000).
24. V. V. Makarov, Astron. J. **126**, 1996 (2003).
25. V. V. Makarov and C. Fabricius, Astron. Astrophys. **368**, 866 (2001).
26. E. E. Mamajek, M. Meyer, and J. Liebert, Astron. J. **124**, 1670 (2002).
27. A. M. Mel'nik, Pis'ma Astron. Zh. **29**, 349 (2003) [Astron. Lett. **29**, 304 (2003)].
28. A. M. Mel'nik, A. K. Dambis, and A. S. Rastorguev, Pis'ma Astron. Zh. **27**, 611 (2001) [Astron. Lett. **27**, 521 (2001)].
29. D. Montes, J. López-Santiago, M. C. Gálvez, *et al.*, Mon. Not. R. Astron. Soc. **328**, 45 (2001).
30. K. F. Ogorodnikov, *Dynamics of Stellar Systems* (Fizmatgiz, Moscow, 1965) [in Russian].
31. C. A. Olano, Astron. J. **121**, 295 (2001).
32. V. G. Ortega, de la Reza, E. Jilinski, *et al.*, Astrophys. J. Lett. **575**, L75 (2002).
33. P. P. Parenago, *A Course on Stellar Astronomy* (Gosizdat, Moscow, 1954) [in Russian].
34. I. Platais, V. Kozhurina-Platais, and F. van Leeuwen, Astron. J. **116**, 2423 (1998).
35. S. Randich, N. Aharpour, R. Pallavicini, *et al.*, Astron. Astrophys. **323**, 86 (1997).
36. N. Robichon, F. A. Arenou, J.-C. Mermilliod, *et al.*, Astron. Astrophys. **345**, 471 (1999).
37. M. J. Sartori, J. R. D. Lépine, and W. S. Dias, Astron. Astrophys. **404**, 913 (2003).
38. D. R. Soderblom, B. F. Jones, S. Balachandran, *et al.*, Astron. J. **106**, 1059 (1993).
39. I. Song, B. Zuckermann, and M. S. Bessel, Astrophys. J. **599**, 342 (2003).
40. J. R. Stauffer, L. W. Hartmann, C. F. Prosser, *et al.*, Astrophys. J. **479**, 776 (1997).
41. *The Hipparcos and Tycho Catalogues,* ESA SP-1200 (1997).

42. J. Torra, D. Fernández, and F. Figueras, Astron. Astrophys. **359**, 82 (2000).
43. J. Torra, A. E. Gómez, F. Figueras, *et al.*, *HIPPARCOS Venice'97,* Ed. by B. Battrick (ESA Publ. Div., Noordwijk, 1997), p. 513.
44. R. J. Trümpler and H. F. Weaver, *Statistical Astronomy* (Univ. of California Press, Berkely, 1953).
45. A. S. Tsvetkov, Astron. Astrophys. Trans. **8**, 145 (1995).
46. A. S. Tsvetkov, Astron. Astrophys. Trans. **9**, 1 (1995).
47. A. Tsvetkov, *JOURNEES-97,* Ed. by J. Vondrák and N. Capitaine (Observatoire de Paris, Paris, 1997), p. 171.
48. R. Wichmann, J. H. M. M. Schmitt, and S. Hubrig, Astron. Astrophys. **399**, 983 (2003).
49. R. Wichmann, G. Torres, C. H. F. Melo, *et al.*, Astron. Astrophys. **359**, 181 (2000).
50. M. V. Zabolotskikh, A. S. Rastorguev, and A. K. Dambis, Pis'ma Astron. Zh. **28**, 516 (2002) [Astron. Lett. **28**, 454 (2002)].

Translated by V. Astakhov

Astronomy Letters, Vol. 30, No. 11, 2004, pp. 797–802. Translated from Pis'ma v Astronomicheskiĭ Zhurnal, Vol. 30, No. 11, 2004, pp. 874–880.

Photon Excitation of Sodium Emission in Comets

E. A. Baranovsky* **and V. P. Tarashchuk****

Crimean Astrophysical Observatory, Nauchnyi, Crimea, 98688 Ukraine

Received March 28, 2004

Abstract—We consider the possibility of the excitation of sodium resonance emission in cometary matter under solar radiation at a heliocentric distance of 5 AU, as was observed when a fragment of Comet Shoemaker–Levy 9 plunged into Jupiter. When the sodium emission is calculated, the multiple scattering in the cometary cloud is taken into account. We use a non-LTE radiative transfer code for a two-level model sodium atom. A comparison of the computed and observed Na I D emission line profiles allows the column density of the sodium atoms for specific times of observations of Comet Shoemaker–Levy 9 to be determined. The observed Na I ($D_1 + D_2$) line profile was found to agree well with the computed profile for an optically thick sodium cloud. We calculated the column density of the sodium atoms for three comets from the observed intensity of the D_2 line emission. We also calculated the D_2/D_1 intensity ratio for various optical depths of the sodium cloud and various phase angles. © *2004 MAIK "Nauka/Interperiodica"*.

Key words: *Solar system—planets, comets, small bodies, heliosphere, sodium emission, radiative transfer, light scattering.*

INTRODUCTION

The spectra of many celestial bodies exhibit rather strong sodium emission, although the abundance of this chemical element is generally very low. This is attributable to the peculiarities of the structure of the sodium atom and its excitation. Thus, for example, almost 70% of the entire emission from meteors is produced by sodium whose abundance in dust grains is less than 1%. In comets, sodium has been observed visually since 1882 (Comets C/1882 I F1 and C/1882 II R1). Now, interest in the sodium emission has increased in connection with the discovery of planetary systems around other stars. Since this is one of the most intense emissions in comets, it can serve as an indicator of the existence of gas–dust and planetary disks around stars that include cometary bodies. Occasionally, small comets undetectable from the Earth fall into the Sun as they approach it. A number of complex physical processes recorded onboard spacecraft arise in the solar corona. Gulyaev and Shcheglov (1999) detected high-velocity clouds of ionized calcium in the (dust) F-corona that could also be supplied by comets.

Sodium emission has generally been recorded from fairly bright comets around their nuclei and at significant cometocentric distances in their tails, but at heliocentric distances up to 1.4 AU (Greenstein 1958; Dobrovol'skii 1966). However, as yet there is no explanation for the absence of sodium emission at large heliocentric distances and for several other peculiarities of its behavior in comets.

In 1994, when fragments of the Comet Shoemaker–Levy 9 (S–L 9) plunged into Jupiter, the emission of high-velocity sodium clouds was observed as one of these fragments was passing through the magnetosphere (Prokof'eva and Tarashchuk 1996; Prokof'eva *et al.* 2002). The authors explained the release mechanism and the observed behavior of sodium in the magnetosphere and roughly estimated the total column density of the sodium atoms. The goal of this paper is to consider the possibility of the excitation of resonance sodium emission in cometary matter under solar radiation at a heliocentric distance of 5 AU and to determine the column density of the sodium atoms.

To calculate the sodium emission under solar radiation, multiple scattering was taken into account. A non-LTE radiative transfer code was used for a two-level model sodium atom. A comparison of the computed and observed Na I D emission line profiles allowed the column density of the sodium atoms to be determined for specific times of observations of Comet S–L 9.

We also considered some of the peculiarities of the sodium emission in other comets at other heliocentric distances for which the corresponding sodium observations are available.

*E-mail:edward@crao.crimea.ua
**E-mail:vera@crao.crimea.ua

1063-7737/04/3011-0797$26.00

PECULIARITIES OF THE SODIUM EMISSION IN COMET S–L 9

On July 20, 1994, when the Q fragments of Comet S–L 9 plunged into Jupiter, more than 200 spectra of this giant planet were taken at the Crimean Astrophysical Observatory with a digital TV system and a spectrograph attached to the MTM-500 telescope. The observations were begun in the daylight sky and carried out from about 17^h until 21^h UT. The spectral resolution was 20 Å, and the time resolution of the spectrum recording was 26 s (Prokof'eva and Tarashchuk 1996). Almost 1.5 h before the impact, when Q fragments surrounded by an extended gas–dust coma were passing through the Jovian magnetosphere at a distance of about $3R_J$ (where R_J is the radius of Jupiter), sodium emission was observed over the entire disk. A circular 6-arcsec aperture was pointed at different parts of the Jovian disk: along the $-45°$ parallel where the cometary fragments struck, the center, the eastern and western equatorial limbs, the north polar region, and the central meridian at a latitude of about $+45°$.

On July 19, 1994, the observations were performed using a similar technique. The Na I line was observed only in absorption and had an equivalent width of 1.2 Å, which is almost equal to the solar line (1.3 Å).

The sodium emission on July 20 exhibited several peculiarities:

(1) The sodium emission was observed over the entire disk of Jupiter; the estimated size of the emission region extended to distances of at least $3R_J$ (Prokof'eva and Tarashchuk 1996).

(2) The emission was observed in the form of a sequence of flashes with an intensity variation time scale of approximately 1 min.

(3) The broad sodium emission was blueshifted and redshifted relative to the unshifted absorption line by up to 30 Å, which corresponds to a velocity of 1500 km s^{-1}. This indicates that ionization followed by the acceleration of sodium ions inside the magnetosphere took place.

(4) The sodium emission was most intense at $18.0–19.2^h$ UT. At 18.0^h UT, the Q2 fragment ahead of the string of Q fragments was at a distance of $4.5R_J$, i.e., in the inner magnetosphere of Jupiter.

The flashes ceased 30 min before the recorded explosions in the Jovian atmosphere, when the distance was less than $2R_J$. The central time of the highest flash activity at 18.9^h UT corresponded to a distance of the Q2 fragment from the Jovian center of $3.1R_J$.

Having analyzed the conditions in the magnetosphere of Jupiter, Prokof'eva *et al.* (2001) suggested the mechanisms of sodium release from dust, the ionization and acceleration of sodium atoms, and estimated the total amount of released sodium. However, it is of considerable interest to estimate the emission of sodium atoms by calculating the radiative transfer for the resonance scattering of solar radiation at a heliocentric distance of 5 AU.

CALCULATING THE SODIUM EMISSION IN THE CLOUD OF COMET S–L 9

Sodium emission has been most commonly observed in comets at heliocentric distances of 0.5–1 AU, but no farther than 1.4 AU. The resonance scattering of solar radiation is generally believed to be responsible for the sodium emission. In our case, we were dealing with observations at a heliocentric distance of 5 AU, and it is not obvious a priori whether the influence of solar radiation can explain this emission. The Na I D line emission observed on Jupiter's satellite Io can be explained in terms of the resonance scattering, but this emission is weak, while in Comet S–L 9, it is about two orders of magnitude stronger.

There is uncertainty in estimating the observed intensity of the emission, because the observations were performed against the background of the Jovian disk. The radiation excess of Jupiter caused by the emission of sodium atoms falls on the continuum rather than the solar absorption line, since the emission is shifted due to the high radial velocity. If the optical depth at the line center (D) is small, then this excess is the emission from the sodium cloud. If, however, the optical depth is large, then Jupiter's radiation is attenuated, and the cloud emission is superimposed on the absorption line. The emission intensity will be higher than the excess above the continuum. Thus, we cannot unambiguously determine the emission intensity without calculations.

Let us first calculate the emission for an optically thin layer. As a result, we obtain the column density of the sodium atoms required to explain the observed emission and the optical depth of the layer. If the calculated optical depth will actually be small, then the problem may be considered to have been solved. If, however, the optical depth is large, then the assumption about a small optical depth is invalid, and the problem must be solved in general form.

To calculate the emission from an optically thin medium, it will suffice to calculate the amount of absorbed emission in a column with a cross section of 1 cm^2 by assuming that each absorbed photon will be reradiated. The amount of reradiated energy is then set equal to the emission intensity. Hence, we find the column density of the ground-state sodium atoms. However, we performed our calculations in more general form in order that these could also be

applied to an optically thick layer. In this case, we take into account the fact that the sodium atoms had significant velocities along the line of sight, so the Doppler shift was much larger than the width of the Na I D lines. The statistical equilibrium equation for a two-level sodium atom is

$$n_2 P_{21} = n_1 P_{12}, \quad (1)$$

where n_1 and n_2 are the numbers of sodium atoms at levels 1 and 2, and P_{12} and P_{21} can be expressed as

$$P_{21} = A_{21} + B_{21}\bar{J} + C_{21}, \quad (2)$$

$$P_{12} = B_{12}\bar{J} + \mathrm{C}_{12}, \quad (3)$$

where A_{21}, B_{12}, and B_{21} are the Einstein coefficients, C_{21} and C_{12} are the collisional transition rates. The quantity

$$\bar{J} = \int \Phi_\nu J_\nu d\nu, \quad (4)$$

where Φ_ν is the line absorption coefficient normalized in such a way that the following equality holds: $\int \Phi_\nu d\nu = 1$.

$$J_\nu = \frac{1}{4\pi}\int I_\nu d\omega, \quad (5)$$

where I_ν is the intensity of the emission inside the cometary sodium cloud, J_ν is the mean intensity of the emission, and $d\omega$ is the solid angle. For the D_1 and D_2 line profiles, we performed the calculations separately. It turned out that the ionization effects and C_{12} and C_{21} may be disregarded.

When the optical depth of the layer is small, the intensity of the emission inside the sodium cloud, I_ν, is equal to the intensity of the solar radiation, $I_\nu = I_\nu^0 = 3.34 \times 10^{-5}$ erg cm^{-2} s^{-1} sr^{-1} Hz^{-1}. According to (4) and (5), we then obtain $\bar{J} = 6.55 \times 10^{-12}$ erg cm^{-2} s^{-1}.

The sodium emission observed when the cometary cloud was passing through the inner magnetosphere of Jupiter had a Doppler shift that reached 30 Å, relative to the position of the solar D_1 and D_2 absorption lines. Therefore, for an optically thin medium, we took I_ν^0 to be equal to the intensity of the solar continuum rather than the line intensity. Having calculated P_{12} and P_{21}, we obtain from Eq. (1): $n_2/n_1 = P_{12}/P_{21} = 1.08 \times 10^{-8}$ for the D_2 line.

If N_2 is the number of atoms at level 2 in a column of matter with a cross section of 1 cm^2, then the energy emitted from an area of 1 cm^2 will be equal to $N_2 h\nu_{12} A_{21}/(4\pi)$ erg cm^{-2} s^{-1} sr^{-1}, where $h\nu_{12} = 3.38 \times 10^{-12}$ erg, and $A_{21} = 4.19 \times 10^7$ s^{-1}. The total intensity of the observed emission in the D_1 and D_2 lines is equal to 2.48 erg cm^{-2} s^{-1} sr^{-1}. The D_2 line emission accounts for 2/3 of this value, so the equality $N_2 h\nu_{12} A_{21}/(4\pi) = 1.65$ yields $N_2 = 1.47 \times 10^5$ cm^{-2} and $N_1 = N_2/1.08 \times 10^{-8} = 1.36 \times 10^{13}$, where N_1 is the number of atoms at level 1.

Let us now calculate the optical depth. At the center of the D_2 line, it is

$$\tau = N_1 k_{\mathrm{D}}^{\mathrm{L}}, \quad (6)$$

where

$$k_{\mathrm{D}}^{\mathrm{L}} = \frac{h\nu}{4\pi}\frac{1}{\sqrt{\pi}\Delta\nu_0}B_{12} = \frac{9.76 \times 10^{-3}}{\Delta\nu_{\mathrm{D}}} \quad (7)$$

is the absorption coefficient at the line center. The quantity $\Delta\nu_{\mathrm{D}} = \frac{1}{\lambda}(2kT/m + V_t^2)^{1/2}$ is the Doppler line width, where T is the temperature, and V_{t} is the turbulent velocity. The widths of the observed sodium lines in comets generally correspond to velocities of $V_{\mathrm{t}} = 10$–50 km s^{-1}, while the temperature is estimated to be $T \leq 500$ K. For $V_{\mathrm{t}} = 30$ km s^{-1}, we obtained $k_{\mathrm{D}}^{\mathrm{L}} = 1.87 \times 10^{-13}$ and $\tau = 2.54$.

For this optical depth, the approximation of an optically thin layer is inapplicable. The problem remains even if a higher turbulent velocity is taken. For the problem to be solved more accurately, we must take into account the multiple scattering of the emission inside the cloud and the attenuation of the light from Jupiter against the background on which the sodium emission was observed. Therefore, we also performed calculations for an optically thick layer of sodium atoms.

For an optically thick layer, the intensity of the emission inside the cometary sodium cloud I_ν in Eq. (5) is unknown, because it must include the multiply scattered photons. In this case, the following radiative transfer equation must be added to the statistical equilibrium equation:

$$\mu(dI_\nu/d\tau_\nu) = I_\nu - S, \quad (8)$$

where $\mu = \cos\theta$, and S is the source function.

We then transform the statistical equilibrium and radiative transfer equations into an integral equation for the source function that can be solved by a method described by Avrett and Loeser (1969).

The initial parameter is a quantity called the primary source, which is determined by the solar radiation absorbed at different depths in the sodium cloud. We numerically solved the equation for the source function and integrated the derived source function over the depth. As a result, we obtained the emergent radiation for a set of wavelengths, i.e., the D_2 or D_1 line profile. These line profiles were corrected for the instrumental profile and added.

Since the sodium emission was observed against the background of the Jovian disk, the radiation

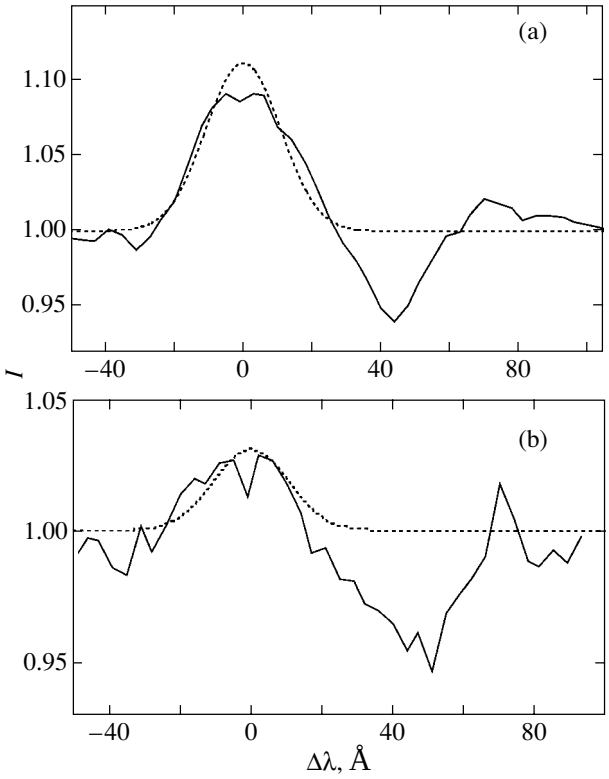

Fig. 1. Computed (dotted curve) and observed (solid curve) Na I $D_1 + D_2$ line profiles for two times of observations of Comet S–L 9 with different equivalent widths of the sodium lines: for (a) strong and (b) weak flashes. The intensity, in units of the continuum, is along the vertical axis.

emergent from the cloud must be added to Jupiter's radiation, which was attenuated by absorption in the sodium cloud. Therefore, we computed the profile of the total emission in the D_1 and D_2 lines. The calculations were performed for various optical depths of the cloud and various turbulent velocities V_t. The results of our calculations depend significantly on the assumed values of these quantities.

Good agreement between the computed and observed line profiles for an intense flash is achieved for an optical depth of the sodium cloud in the D_2 line equal to $\tau = 3 \times 10^2$ and a turbulent velocity equal to $V_t \approx 130$ км с$^{-1}$. In this case, the column density of the sodium atoms is $N_1 = 6 \times 10^{15}$ cm^{-2}. For a weak flash, the column density of the sodium atoms is $N_1 = 3.0 \times 10^{14}$ cm^{-2}.

Figure 1 shows the computed and observed line profiles for these two flashes. We see that the observed and computed Na I D line profiles show satisfactory agreement for the chosen parameters.

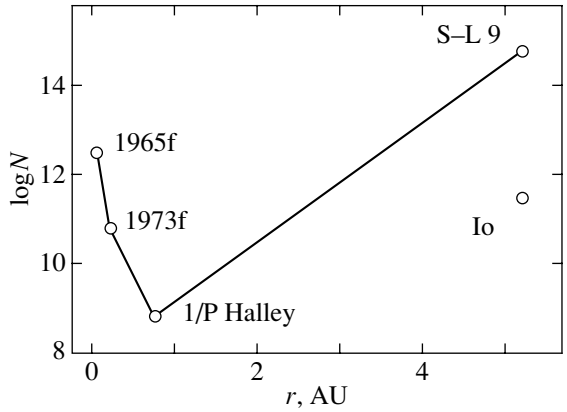

Fig. 2. Calculated column density N of the sodium atoms versus heliocentric distance r for Comets Ikeya–Seki 1965f, Kohoutek 1973f, 1/P Halley (March 5, 1986), as derived from the data of the table, S–L 9, and the satellite Io.

PECULIARITIES OF THE SODIUM BEHAVIOR IN COMETS

Sodium has repeatedly been observed in comets, but these observations were for the most part purely qualitative. The data on emission intensity are depressingly scarce. It is of considerable interest to perform calculations similar to those presented in the previous section for comets with published data on the observed intensity of the sodium line emission.

The table gives data for three comets: Ikeya–Seki 1965f (C/1965 S1) (Evans and Malville 1967; Boyce and Sinton 1966), Kohoutek 1973f (C/1973 E1) (Lanzerotti *et al.* 1974), and 1/P Halley (Combi *et al.* 1997)—the heliocentric distance r and the intensity of the sodium line emission I reduced to the same dimensions using data from these papers. Also given here are the calculated optical thickness and column densities of the emitting sodium atoms N_1.

Since these comets were observed at different heliocentric distances, the pattern of the r dependence can be determined by determining the column density of the sodium atoms N_1. This dependence is shown in Fig. 2. We see that N_1 tends to rapidly decrease with increasing distance from the Sun, but N_1 for comet S–L 9 does not fit this trend and proves to be much higher. This peculiarity also takes place for the N_1 determined for Jupiter's satellite Io. This is probably because these objects differ from ordinary comets and because the mechanism for the appearance of sodium atoms in Jupiter's orbit has its own peculiarities, as shown by Prokof'eva *et al.* (2001, 2002).

Although the number of comets with published quantitative estimates of the sodium emission intensity is small, it is still possible to solve one of the outstanding problems of the sodium behavior in comets: determining the D_2/D_1 line intensity ratio.

Table

Comet	r, AU	I, erg cm^{-2} s^{-1} sr^{-1}	τ	N_1, cm^{-2}
Ikeya–Seki 1965f	0.05	1.0×10^3	2.50	3.1×10^{12}
Kohoutek 1973f	0.22	5.1×10^{-1}	0.036	4.5×10^{10}
1/P Halley	0.75	1.35×10^{-3}	0.0001	1.0×10^8

The Na I D lines are known to arise from the resonance scattering of solar light and to be attributable to the $3^2S_{3/2,1/2}$–$2^2P_{1/2}$ transition to the ground level. For this mechanism, the theoretical doublet line intensity ratio, D_2/D_1, is equal to 2 (or less than 2 for a large optical depth).

However, observations have shown that this intensity ratio could be both larger and smaller than 2. For example, the D_2/D_1 ratio in Comet Mrkos 1957 V (C/ 1957 P1) was 1.39 (Greenstein and Arpigny 1962). In Comet Ikeya–Seki 1965 VIII at a distance of 30" from its nucleus, the D_2/D_1 ratio varied within the range 1.6–2.2 and was within 1.26–1.77 in different parts of its head (Evans and Malville 1967). This ratio was within 2.4–2.6 in Comet Seki–Lince 1962 III (C/1962 C1) (Warner 1963) and even 1 in Comet 1927 IX Skjellerup (C/1927 XI) (Adel *et al.* 1937).

We found that allowing for the Doppler shift of the exciting solar radiation did not increase the Na I D line intensity ratio (we took into account the Swings effect due to the change in the heliocentric velocity of the comet).

Since the previous theoretical estimates of the intensity ratio were obtained in the approximation of an optically thin layer, in our case we calculated this ratio by taking into account the multiple scattering for various optical depths of the layer and various phase angles of the comet. It turned out that the D_2/D_1 ratio at a phase angle $\geq 90°$ could exceed 2 and reach 2.5. The D_2/D_1 ratio at a phase angle of 0° exceeds 2 only slightly, and the pattern of the dependence at an angle of 180° is similar to the run of the curve for a phase angle of 90°, with the maximum value of D_2/D_1 being larger than 2.5.

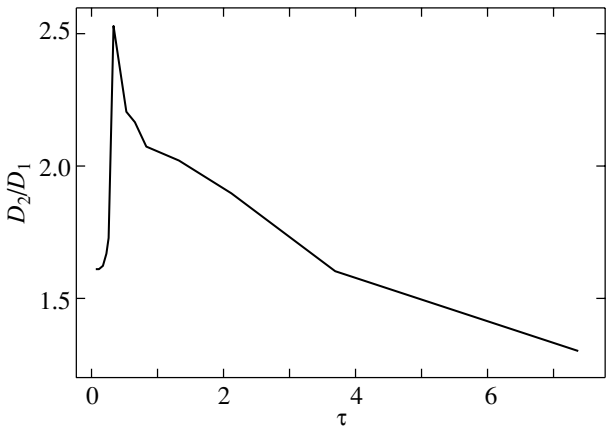

Fig. 3. Calculated intensity ratio of the sodium lines D_2/D_1 versus optical depth τ of the sodium cloud for a phase angle of about 90°.

In Fig. 3, D_2/D_1 is plotted against the optical depth of the cloud for a phase angle of 90°. The intensity ratio was calculated by taking into account the fact that the exciting solar radiation was attenuated by the presence of the D_2 and D_1 absorption lines in the solar spectrum. This attenuation was larger in the D_2 line than in the D_1 line, causing the D_2/D_1 ratio to be less than 2 for a small optical depth. The depth (line-of-sight) distribution of the amount of absorbed solar radiation in the cometary cloud depends on the phase angle. As a result, the depth dependence of the source function appearing in the radiative transfer equation and, eventually, the D_2/D_1 intensity ratio depend on the phase angle, because these lines originate at different depths.

Thus, we obtain a peculiar kind of phase dependence of the D_2/D_1 ratio. This ratio may also be affected by a change in the polarization of one of the doublet components. It is well known that one of the doublet components is polarized, while the other is nonpolarized. Special spectropolarimetric observations of bright comets are required to elucidate this peculiarity of the behavior of the sodium line.

CONCLUSIONS

We studied the sodium emission when one of the fragments of Comet S–L 9 plunged into Jupiter about 1.5 h before the explosions in the atmosphere. The sodium emission was observed in the form of flashes of various intensities indicative of a variable column density of the atoms involved in the flashes. We calculated the atomic column density for the strongest detected flash and for a weak flash. To compare the observed and theoretical line profiles, we performed calculations for a two-level model sodium atom by taking into account the multiple scattering of light in the sodium cloud using a non-LTE radiative transfer code.

We found that the sodium emission observed near Jupiter at a heliocentric distance of about 5 AU could be produced by the resonance scattering of solar radiation at a large optical depth of the sodium cloud and determined the column density of the sodium atoms.

We established that the observed Na I ($D_1 + D_2$) line profile agrees well with the computed profile for an optically thick sodium cloud. The column densities of the sodium atoms in the cloud for strong and weak sodium flashes, i.e., the upper and lower limits, are 6×10^{15} and 3.0×10^{14} cm^{-2}, respectively.

We also performed calculations to compare the calculated and observed emission intensities for several comets observed at different heliocentric distances. These data were used to estimate the sodium column density and its variation with heliocentric distance within 0.05–0.75 AU.

We calculated the D_2/D_1 intensity ratio for various optical depths of the sodium cloud. This ratio was found to depend on the phase angle.

Thus, the sodium emission in comets could be produced by the resonance scattering of solar radiation at heliocentric distances from 0.05 to 5 AU. This indicates that the problem of sodium emission in comets reduces not to its excitation, but to the mechanism of sodium release from dust and to its subsequent propagation in the cometary head and tail at various heliocentric distances.

The appearance of metal emission lines in the spectra of comets as they approach the Sun (or for the so-called sungrazing comets) suggests that the matter evaporation rate increases and the ejection of dust grains, including sodium or its compounds, is enhanced; the solar radiation energy is enough to excite the sodium.

REFERENCES

1. A. Adel, V. M. Slipher, and R. Ladenburg, Astrophys. J. **86**, 345 (1937).
2. E. H. Avrett and R. Loeser, SAO Spec. Rep. No. 303 (1969).
3. P. B. Boyce and W. M. Sinton, Astron. J. **69**, 534 (1964).
4. M. R. Combi, M. A. Di Santi, and U. Fink, Icarus **130**, 336 (1997).
5. O. V. Dobrovol'skiĭ, *Comets* (Nauka, Moscow, 1966) [in Russian].
6. C. Evans and M. J. McKim, Publ. Astron. Soc. Pac. **79**, 310 (1967).
7. J. Greenstein, Astrophys. J. **128**, 106 (1958).
8. J. L. Greenstein and C. Arpigny, Astrophys. J. **135**, 892 (1962).
9. R. A. Gulyaev and P. V. Shcheglov, Dokl. Ross. Akad. Nauk **366,** 199 (1999).
10. L. J. Lanzerotti, M. F. Robbins, N. H. Tolk, *et al.*, Icarus **23**, 618 (1974).
11. V. V. Prokof'eva and V. P. Tarashchyuk, Kinemat. Fiz. Neb. Tel **12**, 82 (1996).
12. V. V. Prokof'eva, V. P. Tarashchyuk, and Yu. T. Tsap, Kinemat. Fiz. Neb. Tel **17**, 538 (2001).
13. V. V. Prokof'eva, V. P. Tarashchyuk, and Yu. T. Tsap, Pis'ma Astron. Zh. **28**, 150 (2002) [Astron. Lett. **28**, 130 (2002)].
14. B. Warner, Observatory **83**, 223 (1963).

Translated by V. Astakhov